O. V. Dykha, K.E. Holenko, M.O. Dykha, V.O. Dytyniuk

SIMULATION OF STRESS STATE AND TRIBOLOGICAL BEHAVIOR IN STRUCTURAL ELEMENTS OF TRANSPORT SYSTEMS

МОДЕЛЮВАННЯ НАПРУЖЕНОГО СТАНУ ТА ТРИБОЛОГІЧНОЇ ПОВЕДІНКИ У КОНСТРУКЦІЙНИХ ЕЛЕМЕНТАХ ТРАНСПОРТНИХ СИСТЕМ

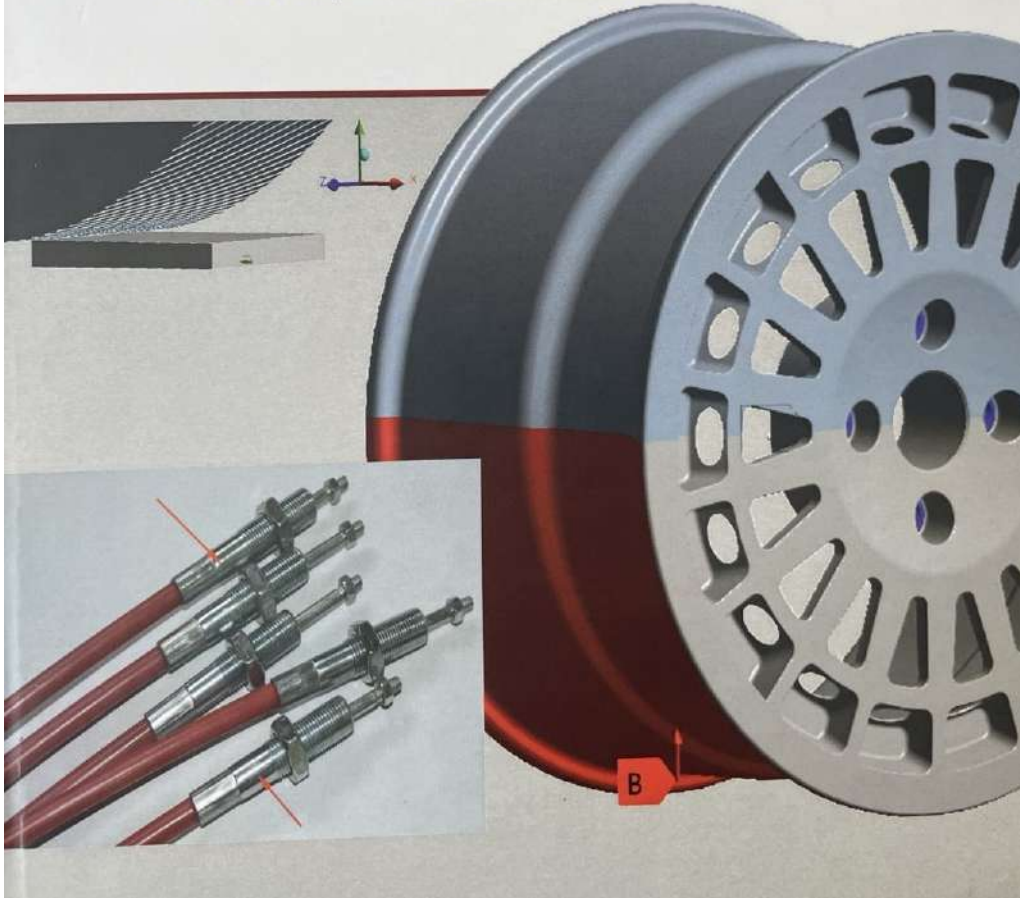

O. V. Dykha, K. E. Holenko, M. O. Dykha, V. O. Dytyniuk

SIMULATION OF STRESS STATE AND TRIBOLOGICAL BEHAVIOR IN STRUCTURAL ELEMENTS OF TRANSPORT SYSTEMS

Khmelnytskyi 2025

O. V. Dykha
K.E. Holenko
M.O. Dykha
V.O. Dytyniuk

SIMULATION OF STRESS STATE AND TRIBOLOGICAL BEHAVIOR IN STRUCTURAL ELEMENTS OF TRANSPORT SYSTEMS

УДК 621.89:629
S614

Рекомендовано до друку науково-технічною радою Хмельницького національного університету, протокол № 7 від 24.06.2025

Авторський колектив:

Диха О. В., д-р техн. наук, проф. (Chapter 3);
Голенко К. Е., канд. техн. наук (Chapter 1);
Диха М. О., канд. техн. наук (2.3. Optimization of technological parameters …; 3.3. Probabilistic approach to assessing …);
Дитинюк В. О., д-р філософії (2.1. Improving the wear resistance …; 2.2. Investigation of the stress contact state …)

Рецензенти:

Лящук О. Л. – д-р техн. наук, проф., перший проректор Тернопільського національного технічного університету імені Івана Пулюя;
Шепеленко І. В. – д-р техн. наук, проф., проф. кафедри експлуатації та ремонту машин Центральноукраїнського національного технічного університету;
Поліщук О. С. – д-р техн. наук, проф., декан факультету інженерії, транспорту та архітектури Хмельницького національного університету

Матеріали подані в авторській редакції

ISBN 978-966-330-450-2

Table of Contents

Chapter 3
Modern approaches to modeling dynamic processes, contact parameters, wear and reliability of structural elements of transport systems

Introduction

Modern mechanical engineering, particularly in the field of transport, is currently undergoing an intensive phase of digital technology integration into processes of design, calculation, optimization, and forecasting of the service life of structural components. The continuous complication of functional requirements for transport systems necessitates a deeper understanding of the physico-mechanical, tribological, and thermodynamic processes occurring in friction units, frame elements, braking systems, and in contact zones of moving parts. An effective tool for this purpose is numerical modeling, which enables accurate and comprehensive simulation of the behavior of structures under various operational conditions.

The objective of this monograph is to systematize the results of the author's research, which cover a wide range of problems related to modeling stress-strain states, thermal loads, contact interactions, and wear of transport machine components. Within three chapters, a comprehensive approach to the structural behavior analysis is presented, using the finite element method (FEM), computational fluid dynamics (CFD), energy-based and probabilistic wear models, as well as experimental design techniques.

The first chapter addresses applied problems of numerical modeling of physico-mechanical processes in transport structures. The focus is placed on the simulation of interaction between a dual-row windshield wiper and a curved glass surface. It is shown that accounting for the blade geometry, its flexible properties, and the hydrodynamic characteristics of the surface enables accurate modeling of the wiper system's performance under various weather and speed conditions. Section 1.2 investigates the influence of triangular side window openings in a bus body on overall stiffness and passive safety, which is especially relevant given modern energy absorption requirements during collisions. Special attention is paid to thermal loading in ventilated brake discs-both constant and variable load regimes are analyzed, with temperature gradients and thermal failure zones identified. The chapter concludes with studies on

parametric modeling of the geometry of control cable reinforcement and the structural reinforcement of light-alloy rims with additional stiffening rings, demonstrating the application of FEM to enhance structural integrity.

The second chapter of the monograph is dedicated to wear resistance of guide elements in transport machines. Section 2.1 provides a detailed tribological analysis of guides, particularly the influence of surface texturing and types of lubricants. Further, the chapter examines surface plastic deformation treatment of cylindrical guide elements, including contact modeling between a roller and the processed surface, as well as stress and temperature analysis in the deformation zone. A separate focus is placed on the process of discrete strengthening of steel cylindrical surfaces. Using factorial experimental design, the optimal processing parameters are determined to achieve maximal improvement in wear resistance. The final part of the chapter explores the influence of surface texture discreteness on the strength of the surface layer—accounting for stress redistribution after pre-profiling of the tribosurface allows for forecasting its service life under different loading conditions.

The third chapter is focused on modeling dynamic processes, wear parameters, and assessing the reliability of structural elements. Section 3.1 examines complex nonlinear oscillatory processes in magnetization systems operating under ferroresonance conditions, which are critical for the functionality of collectors and electromechanical systems. Mathematical models are developed to demonstrate how resonance affects tribological system dynamics. Section 3.2 investigates the tribopair "contact insert – current-carrying wire" in trolleybus systems. Through modeling of contact loads, stress distribution, and energy-based wear models, quantitative assessments are obtained regarding the insert’s service life and main causes of degradation during prolonged operation. The chapter concludes with a probabilistic approach to evaluating tribosystem reliability. Wear is treated as a random variable, and methodologies are presented for calculating reliability under both constant and stochastic loading, offering a transition from deterministic to more flexible predictive scenarios.

Overall, the monograph demonstrates the capabilities of a wide array of computer modeling tools for solving complex engineering problems. The integration of traditional mechanical analysis, CFD, thermal modeling, optimization techniques, and statistical approaches allows not only a deeper understanding of the physical processes in transport systems but also offers effective strategies to improve the reliability, safety, and durability of structural components.

Chapter 1

Comprehensive approach to numerical modeling of physico-mechanical processes in transport structures

1.1. Determining the characteristics of contact interaction between the two-row windshield wiper and a curvilinear glass surface

Normative requirements for windshield wipers are regulated by a number of international rules, in particular the United Nations Economic Commission for Europe (UNECE) in the European Union and the Federal Motor Vehicle Safety Standards in the United States. The latter establish such requirements as: the windshield wiper system should not interfere with the driver's work but remain capable of cleaning the normatively defined area of the windshield during the specified number of cycles, etc. The UNECE R43 regulation also includes performance requirements for windscreen wipers and describes their ability to effectively clear the windscreen of dirt, rain, or snow. However, some parameters of these Rules need to be revised in order to comply with modern trends, for example control of the wiper pressure on the glass surface or the selection of alternative profiles of rubber brushes with an assessment of their effectiveness. Therefore, studies considering the development and optimization of the parameters of the working elements of windshield wipers in contact with the glass surface are relevant.

The review in [1] reflects the evolution of the design of windshield wipers and washers from 1939 to 2021, highlighting the main innovations aimed at optimizing windshield cleaning and improving road safety. It notes the increased risk of accidents in adverse weather due to potential visibility problems caused by wiper and washer systems and offers suggestions for future research areas to further improve these systems. At the same time, in the cited review there are no studies on alternative designs of wiper blades. Windshield wipers are primarily designed to remove water and dirt from the windshield [2], providing the driver with a clear view of the road ahead. Determining

the efficiency of windshield wipers from the very beginning of their design is critically important for ensuring their reliable operation, which is the subject of numerous scientific works. Paper [3] investigates how variations in the curvature of the windshield affect the distribution of forces acting on the side of the windshield wiper and demonstrates the influence on the corresponding dynamics of transient processes. The study includes contact calculations for three different types of windshield curvature and three force application points in a finite element analysis (FEA) module. These data are further analyzed using a series of interconnected mass-spring damping systems to model the dynamic behavior of the wiper blade rib. Works [2, 3] do not contain studies of windshield wipers in critical operating conditions, which is one of the tasks of this work. Paper [4] delves into the complex non-linear interaction between the wiper blade and the vehicle glass using FEA, demonstrating how the shape of the brush affects the load distribution. Since the contact of the blade with the windshield depends on the movement of the windshield wiper, it is useful to refer to study [5], which focuses on the geometric synthesis of the mechanism of the front windshield wiper using rockers for fixing the brush. Wiper mechanisms are also studied in [6]. Despite the relevance of the topics addressed in [4–6], the authors do not provide data on the resulting pressure on the glass surface from the side of the windshield wiper. In [7], the dynamic characteristics and mechanism of generating vibrations of a frameless windshield wiper are studied. A wiper prediction scheme is proposed using a sectional linkage model to estimate vibrations caused by frameless structures and provides a detailed analysis of nonlinear dynamics. Work [8] investigates the dynamics of friction and vibrations during the interaction between a windshield wiper and a vehicle windshield by developing and testing dynamic and frictional models under various conditions. The aim is to provide a theoretical basis for the structural optimization of rubber blades. The authors of [7, 8] do not provide the results of a comparison of traditional and frameless windshield wipers, which is especially valuable from the point of view of friction and vibrations. In [9], the dynamics of wiper blades on a curved windshield were analyzed and attention was focused on such a parameter as the angle of attack, which contributes to the development of the problem of jumps. A two-link analytical model is introduced to study the interaction of dynamic and static friction using a variable gap control method to accurately determine the timing and conditions of transients affecting the jump

phenomenon. Work [10] investigates the vibrations of front windshield wipers and their impact on driving comfort and safety by measuring contact forces at different points along the blade of the brush. Works [9, 10] consider the angle of inclination of the glass, but do not provide data on the effect of changing the radius of curvature of the glass on the obtained reactions and pressure distribution. In reality, the increase in the curvature of the glass helps reduce the load on the wiper at the edges – the uniformity of its fit deteriorates. Considering the scientific novelty of the proposed double-row blade model, it is recommended to familiarize yourself with other novelties in the field of windshield wipers. Paper [11] presents an automatic wiper rain tracking system aimed at improving driver safety by using water sensors, an Arduino Uno, a servo drive, and an external power supply. Such a complex makes it possible to detect the intensity of precipitation and provide automatic control of the speed of the windshield wiper (in order to reduce mechanical errors and driver distractions). The authors of [12] also presented their automatic car windshield wiper system designed to minimize driver distraction by adjusting the windshield wiper speed according to the intensity of the rain and providing an audio signal about the downpour. The system consists of a rain sensor and a servo drive interacting with an ATMega328 (Arduino Uno A000066), showing fast responses and efficient operation, thereby increasing driving safety and potentially integrating with modern automotive technology. Automatic rain-sensing wipers using Arduino are the subject of [13]. Automotive engineers present precise mathematical formulas, applied to a three-dimensional elastic model with specific boundary conditions, to predict the vibration frequencies of the windshield wiper rubber brush [14]. This noise reduction model has been validated with experimental data, showing near-perfect fit, and providing a reliable tool for testing and improving wiper design. Papers [11–14] are based on Arduino but remain isolated from the vehicle user interface. Modern trends in control and driver interaction with car systems are often based on Android Automotive. Despite the fact that the object of research is a conventional windshield wiper, it makes sense to get acquainted with the features of the geometric curvature of a frameless windshield wiper [15], which has nonlinear variable characteristics. Study [16] highlights a method for optimizing the geometry of metal flexible elements in flat windshield wipers by measuring the pressure distribution using piezoelectric sensors and using computer aided design (CAD) and FEA. The authors

apply these techniques to curved windshields, perform dynamic wiping simulations, and compare practical cleaning performance with real-world numerical results to ensure optimal wiper performance. In works [15, 16] there is a lack of results comparing the pressure distribution from traditional and frameless wipers on the curved glass surface under the same boundary conditions. The topic of pressure on the glass surface was previously discussed in [17] – the intermediate state of the system under the action of a vertical load of 20 N applied to the windshield wiper frame was considered. The results showed that the load can be increased, taking into account the permissible limits of movement of the wiper blade according to the Rules R43 (1.5 mm), and therefore the studies are not exhaustive. Paper [18] details the integration of CFD to evaluate the washoff performance of rainwater and windshield wiper fluid on automotive glass surfaces. The study determines the movement of the wiper blades based on Multi-Body Dynamics (MBD), taking into account variables such as the speed and range of the driver and passenger side wipers. The CFD theme continues in [19] – the authors of the study focus on evaluating the waterproof performance of vehicle windshield wiper systems using CFD software PreonLab to simulate water flows, thereby identifying areas of potential waterproofing failure. Study [20] uses numerical simulations to analyze the aerodynamic forces acting on windshield wiper systems at critical angles, focusing on blade geometry and spoiler modifications to counteract lift forces at high speeds. Optimum modifications such as wiper profile, height, and connection type are determined to minimize aerodynamic lift. The effectiveness of these changes has been confirmed through wind tunnel testing, proving that the new wiper design is more efficient and provides higher wiping performance. Despite the use of CFD, papers [18] are focused on the aerodynamics of windshield wipers, but do not provide data on hydrodynamics under various boundary conditions. The authors in works [19] seek to deepen the understanding of the transient aerodynamic effects of moving windshield wipers, using vortex simulation and dynamic grid methods to study the factors affecting the air flow and various aerodynamic forces. An increase in the density of the environment leads to an increase in its resistance – aerodynamic indicators during rain differ from those in dry weather. The theoretical foundations of transient mechanical processes in Ansys Transient Structural are also described in [20] by the authors of this work. The work serves more as a theoretical reminder of the Ansys strength calculation principles applied

in current research. The last fact is closely related to the modern trends of reducing budgets and deadlines for the development and testing of windshield wipers. The so-called "key performance indicators" (KPIs) at all levels of enterprise or laboratory activity dictated by austerity and market competition have additional influence. Extreme conditions of operation of windshield wipers may be the subject of attention of manufacturers of special or military equipment, information about which is limited to open publications. Such specific conditions include, for example, the investigated case of frozen rocker arms and immobilized windshield wiper frame. There is also relatively little research on new types of rubber wiper blade profiles. CFD analysis is an innovative direction since most scientists consider the aerodynamics of the wiper as a whole, rather than the hydrodynamics of an individual rubber blade. Therefore, the above studies show that the UNECE Regulations need to be updated to meet the current trends in the automotive industry.

1.1.1. Interaction of the windshield wiper with a curved windshield

Below are the design features of a conventional windshield wiper based on a simplified assembly (Fig. 1.1) before conducting Ansys tests. A typical assembly structure of a conventional windshield wiper includes a retainer *1*, a frame of the windshield wiper *2*, a rubber brush with a blade *3*, which together rotate on the axis of the drive bracket *4* and are pressed by a spring *5*.

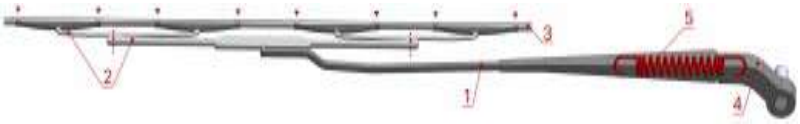

Fig. 1.1. Typical diagram of a regular windshield wiper model: *1* – retainer; *2* – frame; *3* – brush; *4* – bracket; *5* – spring

The spring *5* creates a load, which in the form of pressure is distributed over the surface of the glass with the help of the rubber blade of the brush *3*. At the same time, the force distribution along the contact line cannot be assumed to be uniform. The frame *2* consists of movable links (rocker arms) that rotate on the respective axes (dashed lines in Fig. 1.1) to ensure full adherence of the blade to the glass surface. The rubber brush is clamped by rockers, usually at 8 points (marked by triangles in Fig. 1.1), through which concentrated forces are created on

the rubber blade. It is impossible to compensate for the point load by selecting the appropriate stiffness of the wiper rubber brush, as this parameter is provided by the R43 Rules. The check can be performed by moving a brush over the surface of a standard container with a width of 80 mm or using other legally acceptable equipment. The main transverse dimensions of the rubber brush (visualized solid model in Fig. 1.2) are: the thickness of the blade *7* is 0.6 mm; the height of the blade *1* and the rest of the brush *3* is 5 mm each; neck *2* – 0.5 mm. Index numbers and values are taken from R43.

Fig. 1.2. R43 parameters of the cross-section of the wiper brush: *1* – 5 mm; *2* – 0.5 mm; *3* – 5 mm; *7* – 0.6 mm

Mathematical modeling of the interaction of the wiper with the glass surface (Fig. 1.3) can be carried out on the basis of Winkler's modified solution (model *a* in Fig. 1.3) – a linear elastic model. In the general case, it is a beam of infinite length x with width B and variable bending stiffness $EI(x)$ with an external load diagram $Q(x)$ and a single stiffness parameter k (1.1).

$$\sum_{i=1}^{m} P_i \delta(x - x_i) = Q(x) = \\ = EI(x)\frac{d^4 w(x)}{dx^4} + \frac{M(x)}{R_a^2}\frac{d^2 w(x)}{dx^2} + k \cdot B \cdot w(x), \tag{1.1}$$

where P_i is the point load from the wiper rockers on the rubber blade (in this case, $i = 8$, which corresponds to the triangles in Fig. 1.1); $\delta(x–x_i)$ is the Dirac delta function, and x_i is the location of the concentrated load (the load factor of the windshield wiper rockers); $w(x)$ is the vertical deflection of the beam, m; $M(x)$ is the moment along the beam caused by the curvature of the glass, Nm; R_a – radius of glass

curvature, m; $EI(x) = E(x) \cdot I(x)$ – variable stiffness of the Euler-Bernoulli beam, Pa·m^4; B – beam width, m; k – hardness parameter (subgrade modulus), N/m^3.

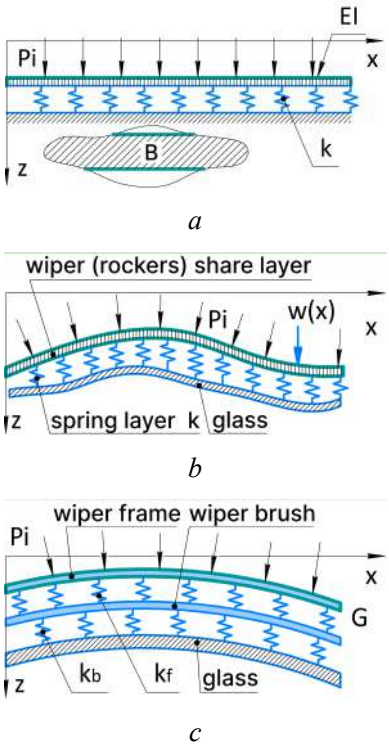

Fig. 1.3. Mathematical multilayer models:
***a*) Winkler; *b*) Parsnip; *c*) Kerr**

$E(x)$ represents the change in modulus of elasticity along the arc length x, which may include effects such as increasing or decreasing stiffness, etc. $I(s)$ is responsible for the change in moment of inertia along x, which takes into account modifications of the cross-sectional area of the brush blade due to the curvature of the contact surface of the wiper. The rubber brush receives different stresses along its length (will be confirmed in the results of the work), taking into account the unevenness of its adhesion to the glass. Then $I(x)$ for a blade with cross section $B \times h$ can be written as $B(x)h(x)^3/12$.

Winkler's approach takes into account the stiffness of the frame of the windshield wiper with rockers, and not their interaction during the shift, so it is advisable to refer to the Pasternak model (1.2) based on the modified Winkler model (1.1) (model *b* in Fig. 1.3):

$$\sum_{i=1}^{m} P_i \delta\left(x - x_i\right) = Q\left(x\right) = W_i\left(x\right) + L\left(w\right), \tag{1.2}$$

where $W_i(x)$ are terms of the equation of the Winkler model (1.1); $L(w)$ is an operator that takes into account interactions during shear.

The surface of the glass and wipers are not rectilinear, which was demonstrated in model *b* (Fig. 1.3) and described in the modified Winkler model (radius of curvature R_a). In real cars, even $R_a \neq$ const (curvature is not constant). If we denote the curvature of the surface by the function of the position along the beam $k(x)$, which takes into account the influence of curvature on stiffness, then the Pasternak model (1.2) will take the following form:

$$EI\left(\frac{d^4 w(x)}{dx^4} - 2k(x)\frac{d^2 w(x)}{dx^2} + 2k\left(x\right)^2 w\left(x\right)\right) + \\ + L\left(w\right) + k \cdot B \cdot w\left(x\right) = Q\left(x\right). \tag{1.3}$$

The specified transient process with the functions $k(x)$ and $w(x)$ (1.3) cannot be mathematically described by a discrete state, and therefore it is necessary to resort to such packages as Transient Structural (Ansys), which are able to calculate the intermediate positions of the system. We shall present other alternative mathematical models, for example, the Filonenko-Borodich model – the continuity of individual spring elements in the Winkler model with their connection in thin elastic membranes under tension *T*. The Hetenyi model – an elastic beam that is subjected to only bending deformations and applies the bending stiffness *D* of the elastic state. The elastic-plastic model (Rhines, 1969) and the Kerr model (Kerr – model *c* in Fig. 1.3), which is of greatest interest to us. This is due to the fact that a regular windshield wiper actually consists of two elastic layers: a frame with rockers and a rubber brush with a blade. Thus, the wiper pressure p_w on the glass surface can be found from the differential equation of the Kerr model in the following form (1.4):

$$p_w = \frac{k_b w(x) + \frac{G\nabla^2 p}{k_f} - G\nabla^2 w(x)}{1 + \frac{k_b}{k_f}}, \quad (1.4)$$

where k_f is the elasticity of the frame layer (wiper with rockers); k_b – brush layer constant; G – shear modulus, Pa; $w(x)$ is the deflection of the framework layer (given that the deflection of the brush is relatively smaller, its value can be neglected, although this is an open topic for possible further research), m; ∇^2 is the Laplace operator.

Analysis was carried out for the most difficult case of wiper operation, when the surface of the windshield was curved, and the rubber blade had a straight profile. This is possible when the moving links (rockers) of the frame of the windshield wiper are frozen or acidified and blocked (do not rotate on the corresponding axes).

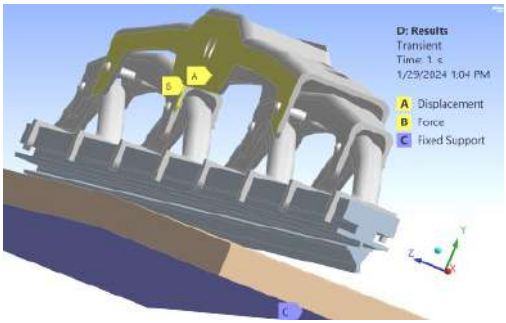

Fig. 1.4. Wiper boundary conditions in Ansys Transient Structural

Then the entire structure is immobilized, which often happens in winter, off-road, or due to the age of the car. The following boundary conditions were set in the Ansys Transient Structural module (Fig. 1.4):

– rigid fixation of the "Fixed Support" of the curved lower surface of the windshield (label C);

– zero displacement "Displacement" (label A) of the windshield wiper frame along the Z axis (parallel to the glass surface) throughout the experiment (duration = 1 s with 5 steps of 0.2 s);

– force "Force" (label B) from the spring (element *5* in Fig. 1.1) applied to the center of the windshield wiper frame along the Y axis

(perpendicular to the glass surface) with a modulus of 24 N. This value is the iteration of previous studies [17], the results which are not exhaustive from the point of view of the margin for the maximum permissible movements of the blade (1.5 mm according to R43);

– the length of the rubber blade is 0.5 m, and the coefficient of friction is 0.1;

– FE-mesh of the model consists of 14268 elements and 41913 nodes.

1.1.2. CFD analysis of the profile of the innovative rubber blade

The idea of our technological advancement refers to the "eternal" question: why do manufacturers of shaving machines equip them with several blades? Why does this not happen in the case of windshield wipers, which also have blades, but rubber ones? The built SolidWorks model (model *a* in Fig. 1.5) is a hybrid of a classic continuous rubber blade with an additional row of individual micro brushes located at an angle. Preliminary expectations of efficiency are based on the idea that each such brush acts like a broom, sweeping dirt from the glass surface on one side and passing streams of water through the channels on the other. Let's test the latter hypothesis by simulating it in the Ansys Fluid Flow module but before that, let's familiarize ourselves with the mathematical modeling approach and the theory of computation.

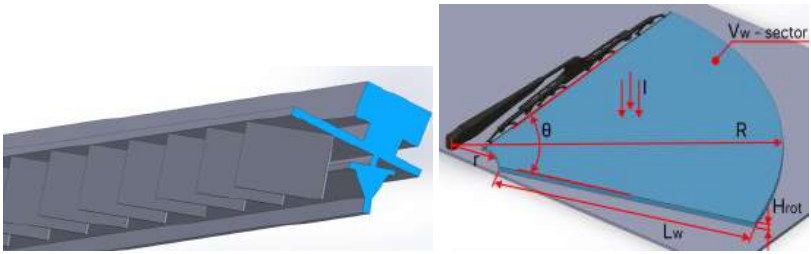

a *b*

Fig. 1.5. Simulating the modified windshield wiper brush:
***a*) solid model with an additional row of individual brushes located at an angle;**
***b*) boundary conditions of the volume of the water sector**

The windshield wiper washes the volume of water V_w during one revolution t_{rot} (model *b* in Fig. 1.5) but the flow rate Q_w will additionally

depend on k_d – the coefficient of dynamism, because in the same time t_{rot} the car travels a distance d_v. In fact, k_d determines how many times V_w must be considered during t_{rot}. The parameter V_w itself is the area of the water sector A_w multiplied by the height of the water layer H_{rot} according to the rain intensity I.

The first theoretical approximation of the calculation model Q_w (model *b* in Fig. 1.5) can be written in the form (1.5):

$$Q_w = \frac{V_w}{t_{rot}} k_d = \frac{A_w H_{rot}}{t_{rot}} \frac{d_v}{L_w \cos\alpha} = \\ = \frac{\left(\frac{\theta}{2}\left(R^2 - r^2\right)\right)\left(I \cdot t_{rot}\right)}{t_{rot}} \left(\frac{v_v \cdot t_{rot}}{L_w \cos\alpha}\right) = \frac{\theta \cdot I \cdot v_v \cdot t_{rot}\left(R^2 - r^2\right)}{2 L_w \cos\alpha}, \tag{1.5}$$

where Q_w is water flow rate, m^3/s; V_w – the volume of rainwater falling on the windshield sector, formed by the rotation of the windshield wiper, m^3; k_d – coefficient of dynamism; A_w – sector area under V_w, m^2; H_{rot} – height of the rainwater sector, m; I – rain intensity, m/s; R, r are the outer and inner radii of the sector, m; θ – sector angle, rad; L_w is the length of the wiper rubber brush, m; t_{rot} – time of 1 rotation (pass) of the windshield wiper, s; d_v – displacement of the car during t_{rot}, m; v_v – vehicle speed, m/s; α is the angle of inclination of the windshield, °.

Taking into account the variability of the speed of the vehicle v_v and the intensity of rain I during the time t_{rot} (1.5), it is advisable to switch to the integral form of equation (1.6):

$$Q_w = \frac{\theta\left(R^2 - r^2\right)}{2 L_w \cos\alpha} \int_0^{t_{rot}} I(t) v_v(t)\, dt. \tag{1.6}$$

After determining the water flow rate Q_w (1.6), which the wiper must remove in 1 pass during t_{rot}, we proceed to the next step – calculating the speed of water passing the profile of the rubber blade. As you know, for a round pipe where the liquid moves laminarly (in layers without turbulence), the Hagen-Poiseuille equation can be applied for a cross section with a complex configuration and a variable area along the flow axis (1.7):

$$v_{HP} = \frac{1}{A_{HP}} \int \frac{Q_w}{\rho} dA_{HP}, \tag{1.7}$$

where v_{HP} is the velocity according to the Hagen-Poiseuille equation, m^2/s; A_{HP} is cross-sectional area, m^2.

More common is the Navier-Stokes equation, which is the basis of hydrodynamics, describing the movement of a liquid in three-dimensional space. Considering (1.6), for an unsteady fluid flow, the determination of the velocity v_f along the windshield wiper brush (x-axis) according to the Navier-Stokes equation (1.8) can be written as follows:

$$\mu \frac{\partial^2 v_f}{\partial x^2} = -\frac{\partial P}{\partial x}, \text{ or } \frac{\eta}{\rho} \cdot \frac{\partial^2}{\partial x^2} \cdot \frac{Q_w}{A(x,t)} = -\frac{\partial P}{\partial x}, \tag{1.8}$$

where μ is kinematic viscosity, m^2/s; v_f – liquid flow rate, m/s; x – coordinate along the x-axis, m; P – liquid pressure, Pa; ρ – liquid density, kg/m^3; η – dynamic viscosity, Pa · s; $A(x, t)$ – cross-sectional area, m^2.

When solving equation (1.8), several interrelated problems arose: $A(x, t)$ is a variable not only with respect to time t (the cross-sectional area of the water flow along the windshield wiper) but also with respect to the x coordinate, which greatly complicates the solution of this equation. In addition, under real conditions, the movement of water is not unidirectional, which increases the degree of complexity of differentiation with respect to all axes x, y, z (model *a* in Fig. 1.6).

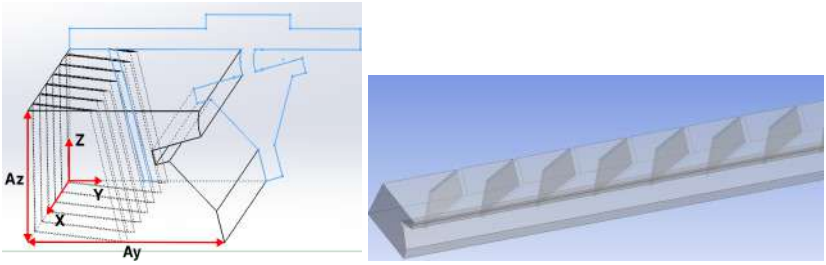

a *b*

Fig. 1.6. The volume of water passing by the modified wiper blade with brushes: *a*) cross section of the volume of water (black lines) under the blade (blue lines); *b*) part of the Ansys water volume model

Thus, it seems appropriate to proceed to the CFD modeling of the water flow (model *a* in Fig. 1.6), which passes by the innovative wiper blade with separate brushes (model *a* in Fig. 1.5). The blue lines (model *a* in Fig. 1.6) correspond to the cross-sectional profile of the wiper blade, and the black lines correspond to the volume of water under it. To simplify the calculation, part of the length of the solid model of this volume of water was simulated (model *b* in Fig. 1.6).

Let's analyze the geometric parameters of the cross section of the water flow volume (model *a* in Fig. 1.6): $A_z \cong$ const is a stable value determined by the physical height of the blade profile. It can fluctuate within very small limits (0.1–0.25 mm max) due to changes in the pressure of the windshield wiper on the glass, which was studied above in chapter 4.1. $A_y \neq$ const is a variable parameter since the area $A(x, t)$ (1.8) depends on the rain intensity I, which was also demonstrated in (1.6). In fact, A_y is responsible for how much water the wiper washes in 1 pass. In the Ansys Fluid Flow model (Fig. 1.7), the incoming water flow with a speed of v_i = 0.5 m/s corresponds to the blue areas (face *a* in Fig. 1.7), and the outgoing water flow to the red (face *b* in Fig. 1.7) with the A_{outlet} area.

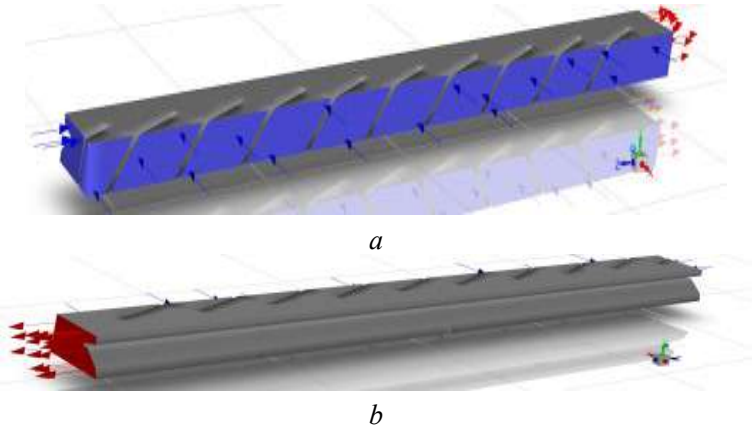

a

b

Fig. 1.7. Ansys Fluid Flow boundary conditions:
***a*) input flow; *b*) output flow**

Such boundary conditions already clearly demonstrate the fact of changing the parameter $A(x, t)$ (1.8) in time and coordinates. Boundary conditions of water: density, 998.2 kg/m^3; viscosity, 0.001003 kg/(m · s); the number of Ansys calculation iterations, 500; the ambient temperature, 22°.

1.1.3. Mechanical interaction of the windshield wiper with the windshield

Analysis of the stressed-strained state of the windshield wiper during contact with the curved glass has made it possible to establish the following results. Modeling of the real operating conditions of the windshield wiper cannot be completely replaced by the above mathematical models, which is clearly visible in the unevenness of the complete movements of the rubber blade along its length (Fig. 1.8). Even Kerr's model (1.4), which is closest in terms of factors to imitation of natural behavior (1.4), is insufficient. It does not fully take into account the change in the stiffness of the windshield wiper along its length – in fact, the coefficients k_b and k_f should be functions. The Mieses stress values are 0.112 MPa and are recorded in the central part of the blade (map *a* in Fig. 1.8). The total displacements were 1.48 mm (map *b* in Fig. 1.8) at the ends of the blade, which, despite the noticeable deflection, did not reach contact with the glass.

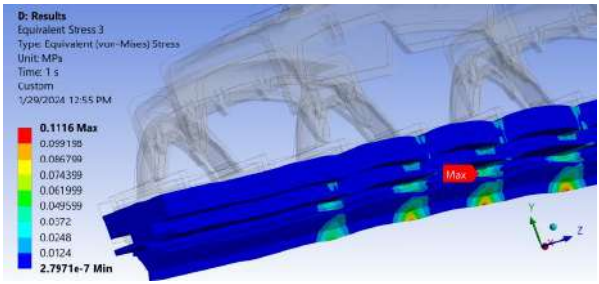

a

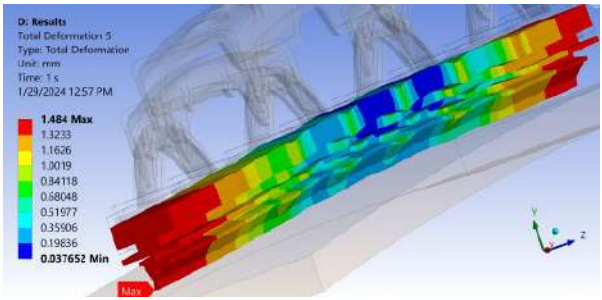

b

Fig. 1.8. Stressed-strained state of the windshield wiper: *a*) stress according to Mieses; *b*) total displacements

The Mieses stress map clearly shows the non-uniformity of the pressure distribution from the blade to the glass surface (the maximum value of 33.4 kPa is observed on map *a*, Fig. 1.9).

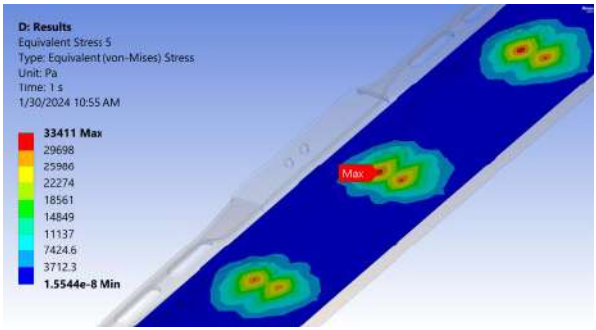

a

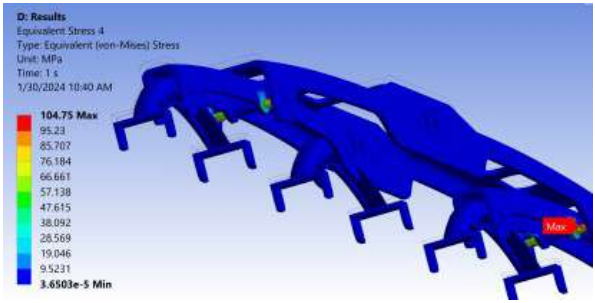

b

Fig. 1.9. Stress maps according to Mieses:
***a*) glass surface; *b*) windshield wiper frame**

The maximum Mieses stress for the entire model in general is 104.75 MPa and is observed on the axes of the wiper frame rockers (map *b* in Fig. 1.9). This is a fairly high value relative to the yield strength (124 MPa for brass). The location of these stresses is predictable since the established boundary conditions (Fig. 1.4) provided for the jamming of the indicated axes to simulate the most difficult case of operation. Despite the linear growth of the external load on the frame (Fig. 1.4) during the experiment (1 s), the movement and deformation of the blade in the selected locations (model *a* in Fig. 1.10) are completely non-linear. This is clearly observed in plots *b*, *c* in Fig. 1.10.

a

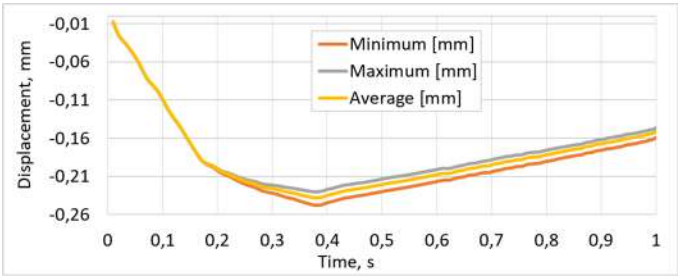

b

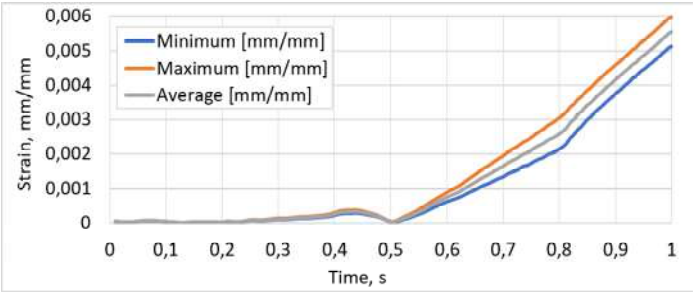

c

Fig. 1.10. Clamps with rockers:
***a*) location points; *b*) displacement of point *B*;**
c*) deformations of point *C

In the process of further loading of the windshield wiper frame, plastic deformations can be observed precisely in the critical areas of the rubber brush. This is traced under each of the specified 8 rocker arm clamps (model *a* in Fig. 1.10), which correlates with mathematical modeling. Such zones are subjected to the load P_i, which is included in equations (1.1) to (1.3). The displacements increased to 1.82 mm (map *a* in Fig. 1.11), and the geometric shape locally has a "cut" character.

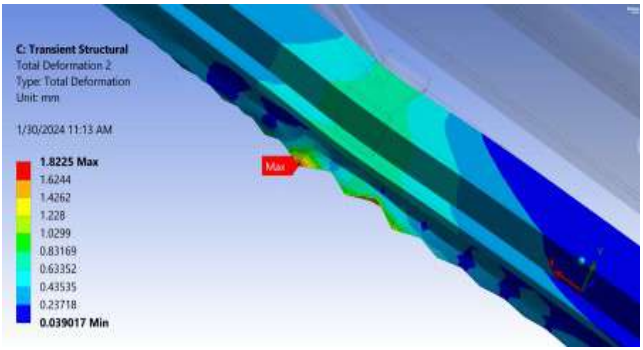

a

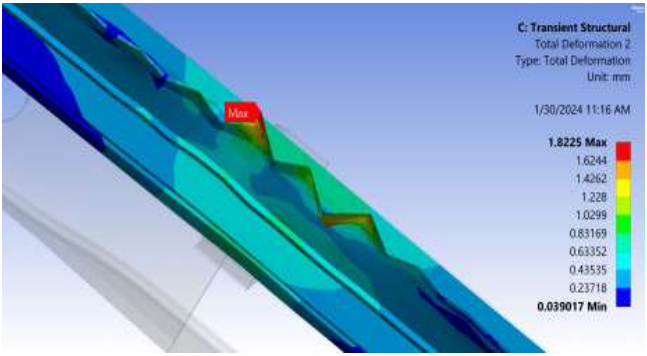

b

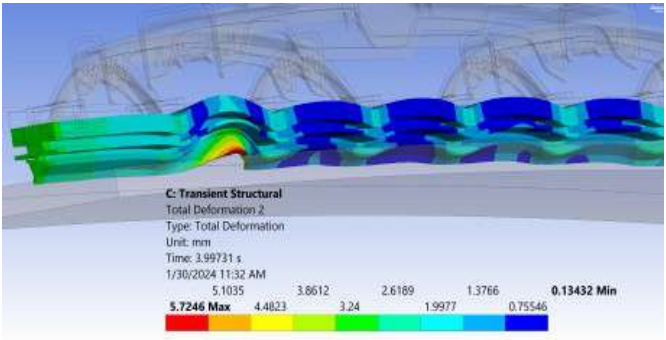

c

Fig. 1.11. Complete movements of the windshield wiper brush: *a*, *b*) local (general and bottom view); *c*) global (loss of shape)

An increase in the load also leads to global deformations – the loss of the shape of the rubber brush with its swelling in the space between the clamps and a lag of more than 5.7 mm from the glass surface. The large gap formed (map *c* in Fig. 1.11) between the blade and the glass will inevitably lead to the appearance of a blind zone and a significant deterioration of the driver's visibility, especially under severe weather conditions.

1.1.4. Results of the analysis of the hydrodynamic contact of a double-row rubber blade with a curved glass surface

Four calculation models were analyzed (Table 1.1): No. 1 – a classic brush with a single-row solid wiper blade and No. 2–4 – models with an additional row of individual brushes and a different range of the parameter A_y, which directly affects the area of the outlet channel A_{outlet}. The criterion for the efficiency of the windshield wiper brush was the maximum fixed speed of water flows v_{max}. Therefore, the faster the windshield wiper washed a given volume of water in 1 revolution, the less liquid and dirt remained on the glass surface.

Table 1.1

Dynamic characteristics of different wiper blade configurations in Ansys Fluid Flow

No.	Blade type	A_y, m	A_{outlet}, t^2	v_i, t/s	v_{max}, t/s	v_{outlet}, t/s
1	Flat blade	0.007	2.6244×10^{-5}	0.5	9.861	9.562
2	With brushes	0.007	2.6244×10^{-5}	0.5	15.61	15.14
3	With brushes	0.009	3.5041×10^{-5}	0.5	14.07	13.65
4	With brushes	0.011	4.3397×10^{-5}	0.5	10.01	9.703

Water flow simulations for different models in the Ansys Fluid Flow module allow us to visually compare the velocity results (Fig. 1.12).

Plastic deformations will certainly lead to the appearance of thin jets of dirt or water on the glass under real conditions due to the distortion of the shape of the blade (map *b* in Fig. 1.11). In some cases, the given local changes in the shape of the blade may become irreversible, which will require the driver to completely replace the wiper rubber brush.

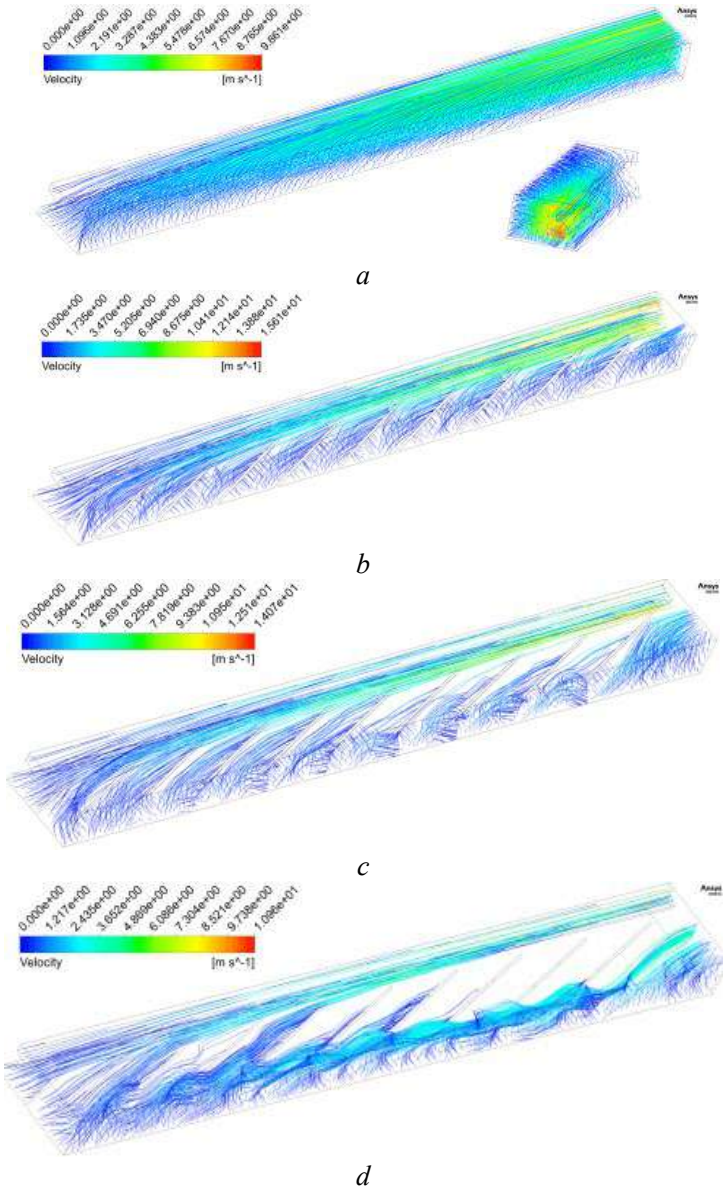

Fig. 1.12. Velocity results of Ansys Fluid Flow models: *a*) flat single row; *b*) #2; *c*) #3; *d* – #4

Despite the visual laminar speed demonstration shown in Fig. 1.12, in fact water flows are partially turbulent. This is clearly visible on the volumetric filling of model No. 3 (Fig. 1.13) – red clumps with local vortices (maximum values of velocity).

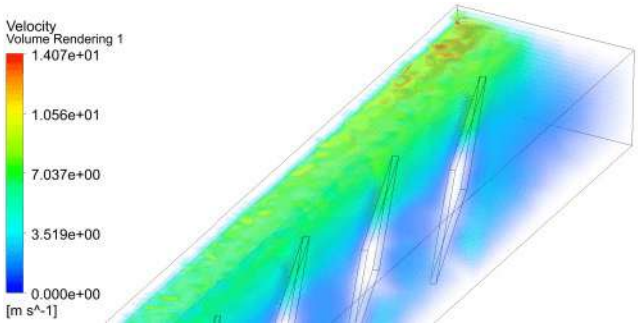

Fig. 1.13. Visualization of speed by volumetric filling of model No. 3

The distribution of the output velocity v_{outlet} along the outlet plane (red region *b* in Fig. 1.7) with the area A_{outlet} is shown in Fig. 1.14, and the values are indicated in Table 1.

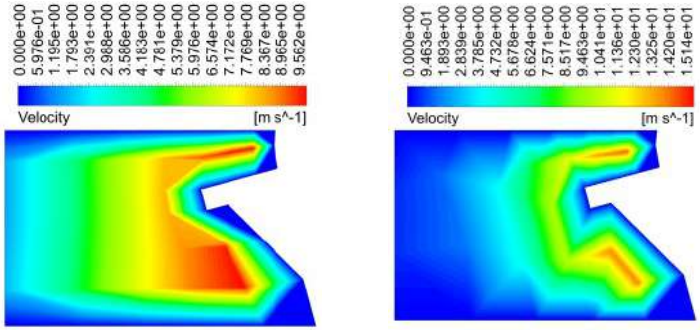

a *b*

Fig. 1.14. Velocity maps on the outlet plane A_{outlet} of the blade model: *a*) flat; *b*) # 2

From the given maps, it is possible to judge the distribution of velocities in the perpendicular plane of the windshield wiper and observe hydrodynamic trends.

Our research results, as well as those proposed by other authors [17], show that the optimal average value of the force of pressing the frame of the windshield wiper (1.2) by the spring (Fig. 1.1) is ≈20 N. According to our results, it was established that the loads should not exceed 24 N for this wiper configuration. A lower load value may not ensure sufficient adhesion of the wiper to the glass at the edges of the rubber brush in extreme operating conditions. The rubber blade showed a total displacement of 1.48 mm in the central part (map *b* in Fig. 1.8), which is quite a high indicator. Judging by the R43 wiper blade regulatory requirements (Fig. 1.2), the maximum total movement cannot exceed 1.5 mm since the height of the neck 2 is only 1 mm. Thus, for the specified materials ("Neoprene Rubber" and "Structural Steel NL") and geometrical parameters of the windshield wiper, the load value of 24 N is the upper limit in the case of mechanical immobilization. The frozen state of the rockers leads to an increase in Mieses stresses in their axes up to 104.75 MPa (map *b* in Fig. 1.9), which is close to the yield point of brass (σ_m = 124 MPa). The maximum value of pressure (33.4 kPa) was also recorded in the contact spots of the windshield (map *a* in Fig. 1.9), which correspond to the position of the rocker arms. This value is not critical but during accidental release of the spring-loaded wiper, it can increase several times and lead to impact on the glass and the appearance of cracks at low temperatures.

Further loading of the frame of the windshield wiper was accompanied by the appearance of deformations of two types: local and global (loss of the shape of the rubber brush). Local ones are manifested in the form of movements at the level of 1.82 mm (higher than the permissible 1.5 mm according to R43) and the appearance of thin jets of dirt or water on the glass as a result of cutting the blade. Global leads to the loss of the shape of the rubber brush with its swelling in the space between the clamps and the formation of a gap of 5.7 mm between the glass and the blade (map *c* in Fig. 1.11). This will certainly cause the appearance of a blind zone and a significant deterioration of the driver's visibility. Among modern passenger cars for masses, only the Mercedes-Benz G-Class and Tesla Cybertruck models have flat windshields, but on other cars the curvature and area of the glass is constantly increasing with each new generation. Our results of the distribution of pressure on stresses testify to the solution of the problem of studying the interaction of the windshield wiper with the curved surface of the glass. In contrast to [2–10], in which variants of the absolute repeatability of the curvature of the

windshield wiper and the glass surface are considered, the current research data demonstrate the application of other possible cases of operation.

Among the considered mathematical models for calculating the distributed load, the Kerr model turned out to be the closest in compliance with the boundary conditions of full-scale tests compared to Winkler's or Pasternak's solutions. A conventional wiper actually consists of two elastic layers: a frame with rockers and a rubber profile with a blade, which correlates best with Kerr's approach. The problem is that such a transient process as the presented calculation case (an immobilized frame pressed against a curved windshield) with functions $k(x)$ and $w(x)$ cannot be mathematically described by a discrete state. It is impossible by mathematical modeling to achieve such local full displacements as 1.82 mm obtained using FEA in the Ansys Transient Structural module (Fig. 1.11). Actually, this point can be attributed to the so-called limitations and shortcomings of our study from the point of view of its application in practice. On the other hand, the proposed mathematical models could serve as a basis for further theoretical research, which is a subject of scientific value because this approach is less resource-intensive than FEA with its iterations.

The reviewed literature [2–10, 15–20] does not sufficiently describe other variants of rubber blades, except for the traditional single-row one. A variant of the rubber blade with an additional row of individual brushes located at an angle has shown useful practical results. With the same initial area A_{outlet}, the wiper blade with brushes No. 2 (Fig. 1.12) provided 1.58 times higher speed $v_{\max}$ than in the case of the classic single-row model No. 1 (15.61 vs. 9.861 m/s). And even with a 1.73-fold increase in water volume when going from No. 1 to No. 4, the velocity values are almost the same. This confirms the effectiveness of the design of the brushes of the second row, which are used in No. 4 (A_{outlet} in No. 1 is 2.6244 m^2 against 3.5041 m^2 in No. 4).

The proposed additional individual brushes act as turbine blades, creating additional centrifugal accelerations of water flows, which is clearly visible in the visualization of the volumetric filling of model No. 3 (Fig. 1. 13). The distribution of the output velocity v_{outlet} along the outlet plane (red area of model *b* in Fig. 1.7) with the area A_{outlet} (Fig. 1.14) coincides with the trend of the volumetric analysis described for $v_{\max}$ (v_{outlet} is 15.14 m/s for model No. 2 against 9.562 m/s for No. 1). The following trend can be observed: the larger the value of A_y (model *a* in Fig. 1.6), the more distant water flows in the discharge plane (models *d*

and *c* in Fig. 1.12, 1.14). Thus, a 2-row blade model is implemented – the first layer removes dirt, snow, and water with separate brushes, and the second one finally cleans the surface. Our results testify to the hydrodynamic analysis of the proposed innovative blade. Studies [18–23] that considered the CFD problem were focused on the flow of air currents around windshield wipers but did not investigate the hydrodynamics of windshield wiper blades. The limitations of our research on hydrodynamics are manifested in the coverage of possible combinations of sizes and angles of inclination of individual brushes, their distance from the main row and physical and mechanical properties of rubber. To carry out multifactor modeling, it may be necessary to build individual AI models for iterative prediction of optimal combinations of the specified parameters. The next step involves CFD verification of the results in the Ansys Fluid Flow module and the construction of a physical sample of the double-row blade, which requires financial costs for the production of the prototype.

Our research may be advanced toward selecting optimal configurations of rubber brushes for the second row: length and thickness, angles of inclination and distance from the main row, as well as rubber stiffness. The problems of combinatorics under conditions of multifactoriality belong to the obvious difficulties of the current research: field testing of physical samples is expensive while mathematical modeling is time-consuming and insufficiently accurate. Perhaps it is appropriate to involve AI with the construction of appropriate mathematical models for the iterative search for the optimal combination of indicators, both from the point of view of hydrodynamics and the uniformity of pressure distribution. This stage could be the next one, preceding the registration of a patent for a utility model or invention.

Conclusions

1. It was established that the pressure value should not exceed 30–50 kPa, and the external normal load on the frame of the windshield wiper by the spring should not exceed 20–30 N. The blade of a conventional windshield wiper was deformed by 1.48 mm under the action of a load of 24 N. According to Rules R43, the maximum value of the full movement cannot exceed 1.5 mm, therefore, for this wiper configuration, the applied load is the maximum allowable. Local pressure spots on the glass with a maximum Mieses stress value of 33.4 kPa were obtained, which decreased to zero at the ends of the windshield wiper,

where a gap was formed. Such an uneven load distribution significantly reduces the area of windshield cleaning (to 40 %) and can create water drainage between the specified spots. Under the jamming mode of the rockers on their axes, the maximum Mieses stresses are formed at the level of 104.75 MPa, which is at the yield point of brass (124 MPa). Despite the linear growth of the load to a maximum of 24 N within 1 s, the magnitude of the complete movements of the rubber blade in the places of the clamps under the rockers (Fig. 1.10) is non-linear. Further loading of the wiper frame causes plastic deformations (local and global) in the vicinity of these clamps. The total displacements increased to 1.82 mm, and the geometric shape in this zone had a "cut" character (local deformations), creating thin jets of dirt on the surface of the glass (Fig. 1.11). Global deformations were manifested in the loss of the shape of the rubber brush and the formation of a gap between it and the glass (5.7 mm), which significantly worsens visibility in bad weather. None of the analyzed models (Winkler or Pasternak) can provide the magnitude of such plastic deformation, as it does not take into account transient processes.

2. We have proposed a structure of a double-row blade with separate brushes. With the same outlet area A_{outlet}, the model No. 2 wiper brush demonstrated 1.58 times higher speed $v_{\max}$ than classic single-row model No. 1 (15.61 vs. 9.86 m/s). The described design of the blade allows the passage of a much larger volume of water at the same time. With an almost two-fold increase in water volume between models No. 1 and No. 4, the velocity values remained almost the same, which confirms the effectiveness of brushes of model No. 4 (A_{outlet} in No. 1 is 2.6244 m^2 versus 3.5041 in No. 4). The output velocity distribution v_{outlet} matches the volumetric analysis trend described for $v_{\max}$. This means that the designed model of the blade is not inferior in efficiency at the final stage of releasing the consumed volume of water. The higher the value of A_y (ranging from 0.007 to 0.011 m – model *a* in Fig. 1.6), the more distant water flows in the outlet plane (model *d* in Fig. 1.12). At the same time, the speed of the external flow also increases (5.5–6.8 m/s for model No. 4).

1.2. Influence determination of triangular interwindow openings of a bus body on its structure, strength and passive safety

1.2.1. The state of problem

The EU sets ambitious targets for reducing CO_2 emissions for buses (city and intercity with an equipped weight of more than 3,500 kg)

by 15 % by the end of 2025 and by 30 % closer to 2030. To achieve climate neutrality by 2050, buses need to achieve full decarbonization. A possible solution is the introduction of vehicles with a zero emission level (Zero Emission Vehicles – ZEVs), which include electric buses on fuel cells (Fuel Cell Electric Buses – FCEBs) or directly on batteries (Battery Electric Buses – BEBs). The latter significantly increase the equipped mass of city buses (up to 12–18 % depending on the class), creating an additional load on the body. Given the low-entry or low-floor layout, the only possible place to install batteries is the roof, which in turn requires finding ways to strengthen the sides of the body. Since the body of a bus makes up about 30–40 % of its cost, and the city fleet of the EU as of 2024 has about 900,000 vehicles, there is a global task of adapting bodies to BEBs with minimal structural changes. One of the possible solutions for strength optimization is the transition from conventional rectangular side window openings to more rigid triangular ones. As a result of electrification, which requires mandatory compliance with the requirements of R100, the question of the uniform strength of the body under the conditions of daily operation in the modes of so-called "bending" and "torsion" also arises. Adherence to allowable stresses (relative to yield strength), safety factor, and deformations are among the requirements that must be checked. Therefore, studies aimed at designing the optimal structure and strength of the bus body by integrating triangular window openings and comparing the stress-strain state (SSS) with the classic rectangular model are relevant. In practice, the research results are equally important both for existing car fleet (local intervention in the body side structure above the window frame) and for new promising models with maximum unification for any type of drive.

Before starting to analyze available studies, it is advisable to get acquainted with our previous work, which forms the foundation of technological advancements in the field of modeling the stress-strain state of structures in the Ansys environment. In fact, the results of our studies acted as a driver for devising such new measures to optimize strength as the integration of triangular structures to the sidewalls of the body. Thus, the current work is a logical continuation of a series of previously published papers that are more practical for engineers and scientists as a complex. Thus, paper [21] focuses on the features of the low-floor body and the structural differences of city buses, such as the absence of deformation zones. We modeled a frontal impact of a city bus taking into account the UNECE R29 requirements for passenger

safety. The research results demonstrate the stress and deformation zones of the body, taking into account the reduced stiffness indicators and lower energy absorption of city buses in the event of a collision. The subject of estimating stresses, strains, and safety factor SF of a spatial body truss was also investigated by us in [22], however, using a different type of body as an example. Under the conditions of the transition to Euro-7 environmental standards with the change of diesel traction to electric, the question arises of the influence of the installed battery unit on the architecture and strength indicators of the body. The paper simulates the static and dynamic load modes of the truss using the coefficient k_d = 2.0, analyzes the stresses and deformations under the "bending" and "torsion" modes. The research results are important from the point of view of the conditions of daily operation, but the issues related to passive safety, such as UNECE R100, remained unresolved. It is shown that measures to optimize the structure made it possible to reduce the mass of the truss by 4.13 % and reduce the maximum stresses from 381.13 MPa to 270.5 MPa. Our paper [23] also provides the theoretical and applied foundations of Ansys, which are necessary for effective work with the model – Mises stress estimation, deformation zones, and the *SF* safety factor. On the basis of the processed materials and taking into account the global trends towards the electrification of buses (increasing the equipped weight), an idea was formed to strengthen the sides of the body by transforming the window openings from a rectangular to a triangular shape. In the history of Ukrainian bus construction, there were already prototypes with a similar "triangular" concept – models of the LAZ-360 series from Ukrbusprom, which is a source of pride for domestic engineering. However, the roof structure remained classical in contrast to the proposed "triangular" one in the current study. The likely reason is objective difficulties associated with the complexity of production and its manufacturability (profile cutting and welding at an angle, etc.).

Modern international publications by other authors consider the strength and passive safety of bus bodies not only on diesel but also on electric traction (BEB). This is the approach used in work [4], in which the authors conducted static and dynamic tests in order to optimize the body structure of a fully electric bus manufactured by Letenda Inc. To ensure durability in accordance with regulatory requirements, experiments were performed with variable driving conditions. Special attention is paid to the methods of correlating experimental data of vehicle response with known input signals for model validation. Work [25] considers the

optimization of the design of the light iron-aluminum body of an electric bus, taking into account static characteristics (strength and stiffness), safety in the event of a side rollover, and possible weight reduction. Finite-element models of static loads and side impact were developed, and the body truss was segmented by the thickness of profile pipes and their contribution to deformation. Three optimization schemes targeting different objectives were compared and the results evaluated through FE simulations. It was shown that the stresses decreased by 34.41 %, and the penetration depth by 4.48 %, while the mass remained almost unchanged; however, the issues of stiffness remained unresolved. Side rollovers as one of the basic certification test modes of electric buses are also covered in [26]. An analysis of variable parameters of the body was carried out and a mathematical model of multi-criteria optimization of the structure was built. A neural network based on radial basis functions was used to approximate the optimization model, and its accuracy was verified using test data. The optimization problem was solved using the Non-dominated Sorting Genetic Algorithm II (NSGA-II). The results showed that the weight of the optimized model was reduced by 240 kg (9.0 %) without changing the body frame materials, while maintaining the required strength and stiffness characteristics. All this gives reason to argue that it is advisable to use the NSGA-II algorithm in this kind of problems. This is a popular evolutionary algorithm used to solve multi-objective optimization problems. This is the approach used in [27]. The work considers the optimization of the bus body structure to reduce mass, taking into account rollover safety (ECE R66). A combination of a neural network (back propagation – BP) and the NSGA-II algorithm was used for multi-criteria optimization. The results showed a weight reduction of 7.7 % without loss of safety, which confirms the effectiveness of the proposed approach. Paper [28] studies the strengthening of the bus frame with composite materials to increase its strength and protect passengers during accidents. The frame of the bus, made of steel, was reinforced with a coating of composite materials. In accordance with the ECE R66 standards for the strength of superstructures of large passenger vehicles, a structural analysis was performed using LS-DYNA simulations. It is shown that the use of a frame made of composite-reinforced steel improves the protection of passengers, which was confirmed by the final rollover simulations. In addition to side rollovers, frontal crash tests remain relevant. For example, work [29] considers the development and implementation of a scheme for optimizing the structure of an electric

bus body, taking into account a frontal collision. The authors consider uncertainty factors that could affect the energy-absorbing characteristics of the body during an impact. An approach to strength optimization is proposed, which takes into account the design of deformation zones and makes it possible to analyze the influence of parameter variations on objective functions and constraints. Analytical methods such as entropy weight method, TOPSIS method, and correlation analysis were used to select variables, which made it possible to choose 15 shape parameters with the greatest influence on body strength. The research results of the work, like all the publications analyzed above, are based on a model with rectangular window openings. None of the models that were subjected to side or frontal crash tests in the cited works had triangular windowsills, which could theoretically improve the rigidity of the body. The likely reason is the objective difficulties associated with the expendable part of the body production with triangular armholes. The lack of real buses with similar sidewalls causes a lack of prototypes for their research and, therefore, related scientific works.

There are a number of publications whose authors chose an approach to optimizing the body based on the use of aluminum in combination with steel, but without the inclusion of triangles in the body side structure. Thus, work [30] considers reducing the mass of the hybrid body of an electric bus made of steel and aluminum to increase the mileage. A combination of a genetic algorithm (GA) and a radial basis function (RBF) model was used for multicriteria optimization. The proposed approach made it possible to reduce the mass of the body by 38.4 % owing to the use of an aluminum frame, and additional optimization reduced the mass by another 4.28 % without losing rigidity and strength. The research results are correlated with [31], in which the aluminum-steel structure of the body of an electric bus is also analyzed in order to reduce mass and increase mileage. The use of gradient optimizers ensured a reduction in mass while preserving the design characteristics, but the NSGA-II algorithm could have been used. Paper [32] describes the optimization of the bolted T-connection of the steel-aluminum body of an electric bus to increase its durability and reduce deformations. A finite element model was used to analyze fatigue strength, and the Kriging method was used to build a surrogate model. The optimization was carried out using the adaptive simulated annealing method (Adaptive Simulated Annealing – ASA), and to increase reliability, the Monte Carlo optimization approach, and archive-based

Micro Genetic Algorithm (AMGA) were used. The research results showed an increase in the minimum resource by 60.80 % and a decrease in the maximum deformation by 4.87 %, which significantly improves the overall efficiency of the structure. All this gives reason to assert that it is expedient to carry out a comprehensive analysis both of the structural optimization of the body and the use of materials alternative to steel.

Separate studies consider the structural optimization of the strength of bus bodies, however, in the absence of triangular armholes in the composition of the body. Thus, the authors of [33] investigated the multi-criteria optimization of the body design of a large electric bus to reduce mass, reduce movement resistance, and increase energy efficiency. They performed topological optimization of the roof, floor, and side panels of the frame using FEA. Through sensitivity analysis, 13 variables affecting weight reduction were identified. Further optimization was performed by the MOGA method, taking into account the minimization of mass and the maximization of bending and torsion frequencies. The results showed that the weight of the frame was reduced by 303 kg (11 %), providing all the requirements for static and dynamic characteristics, but the question of body rigidity remained open. Study [34] improved the conventional bus body frame design by focusing on the cross-sections of the tubular beams instead of just their thickness. The multi-objective approach to optimization includes a radial basis function neural network (RBFNN) and a genetic sorting algorithm II (NSGA-II – non-dominated sorting genetic algorithm). The results show a 5.9 % reduction in structural mass and a significant improvement in stiffness, with prediction errors not exceeding 0.3 %. It is shown that the selection of combinations of cross-sections is an effective solution but the issues of welded joints, the area of which is reduced when using a lighter assortment of pipes, remain unresolved.

Bus drive schemes could be different: not only diesel or electric, but also hydrogen. The body of the bus must be unified, so it is advisable to read, for example, [35], in which the authors present the adaptation of the design for the integration of heavy and bulky components of alternative drives, such as battery or hydrogen systems. Within the framework of the AnoWaAS project, structural solutions with the greatest potential for lightness have been identified, in particular, the use of trapezoidal windows, which is close to the topic of current research. The optimization made it possible to reduce the weight of the body by more than 20 %, ensuring compliance with the flow of forces

and weight reduction. All this gives reason to assert that it is advisable to conduct research on the selection of alternative rectangular window openings. The authors of paper [36] investigated the safety of the hydrogen city bus frame. The analysis showed that the maximum stresses during emergency turning and torque exceed the yield strength of the material. Optimizing the thickness of the components reduced stress to an acceptable level and reduced the frame weight by 106 kg, meeting the strength and weight requirements, but no deformation information.

Since among the boundary conditions of the current study there is a battery pack on the roof (R100 test), it is important to analyze the strength studies on the battery pack structures. This is the approach used in work [37], in which the design of the battery unit was analyzed with static and modal analysis under various conditions (turning and emergency braking on a rough road). Modal analysis revealed a frequency of 33.69 Hz, indicating the possibility of resonance. The authors of paper [38] proposed a method for optimizing the design of the battery unit housing to reduce weight through the thickness of the housing as an optimization parameter. It is shown that the maximum stress is reduced to an acceptable level, the first-order frequency is increased by 41 %, the resonance is reduced, the maximum deformation is reduced from 2.7 to 1.12 mm, and the total mass is reduced by 26.8 %. Study [39] considers the strength of the attachment of battery packs with corresponding reactions, modal analysis, and the influence of the battery pack on the overall strength of the body. The shortcoming of the research and a possible future direction of its development is the lack of vibration tests, as it is given in work [40]. The authors describe the methodology for modeling and analyzing the vibrations of the bus body in accordance with the AIS-153:2018 standard. An approach to determining the lowest natural frequency and analyzing vibrations in accordance with regulatory requirements has been devised. Paper [40] analyzed the frame of a medium-sized passenger bus and its dynamic and vibrational properties when replacing the materials of auxiliary structural elements with fiberglass. Theoretical and experimental modal analysis confirmed a change in dynamic characteristics of up to 20 % (resonant frequencies) compared to a steel frame. The replacement of materials made it possible to reduce the weight of the frame by 11 %, lower the center of gravity, and maintain the safety of the structure, which improves stability, comfort, and reduces fuel consumption. The research results suggest the expediency of conducting discrete local tests of the battery block as part of the two-mass "body-battery" system.

Summarizing the above publications, it could be concluded that the use of the triangular structure of window openings has not been found in modern literature and has prospects for the development of research. It could be assumed that among the possible reasons for the lack of publications is the more complex process of manufacturing the body and its glazing on real buses. In the case of a curvilinear shape of the sidewall profile, conventional vertical racks have the same radius of rounding, and in one plane (transverse), and allow the use of a common pipe bender. The transition to diagonal racks, which as a result form triangular window openings, requires simultaneous bending and twisting of pipes. The situation is further complicated by the fact that they are of different lengths according to the sections of the bus, and therefore there is no question of a single pipe bender. Cutting diagonal pipes and their welding are also significantly more difficult in comparison with the conventional rectangular shape of the lumbar section of the body.

From our review of the literature, the following could be stated. Works [4–9] focused on strength and passive safety of buses (including BEB), but without tests according to R100; [10–12] compare aluminum-steel structures with conventional steel ones, but only with a rectangular sidewall structure. Publications [13, 14] study the influence of various pipe profiles on the strength of a conventional body configuration; [17–19] analyze the fastening of battery blocks according to R100, but do not consider the entire body as a whole. The authors of [20, 21] study the oscillations, vibrations, and comfort of buses with typical vertical body struts. Thus, among the considered works, no studies on structural optimization of bodies were found, as a way to solve the problem of loading buses in connection with their electrification by installing batteries on the roof. This body part is possible for low-floor urban BEBs, which causes the need to strengthen the body sides, the relevance of which is obvious in connection with the introduction of Euro 7 from 2030.

1.2.2. The study materials and methods

The object of our research is the spatial model of the body frame for the low-entry city bus "Ukrautobusprom – 4289". The basic hypothesis of the research is to check the increase in strength and rigidity of the body as a result of the integration of triangular windowsills instead of conventional rectangular ones. A triangle is a more rigid figure than a rectangle because of its geometric stability – the impossibility of changing the shape while preserving the area without changing the length of the

sides and angles. Instead, a rectangle could easily deform into a parallelogram if forces are applied to it, even if the side lengths remain the same. Mathematically, this is confirmed by the basic equation of the area of the triangle A_T, which connects the sides and angles:

$$A_T = \frac{1}{2} a \cdot b \cdot \sin(\theta), \tag{1.9}$$

where a, b are the sides of the triangle, mm; $\sin(\theta)$ is the sine of the angle between them.

When a force P is applied to the rectangle, its angles could change, and it deforms to form a parallelogram. Formally, this could be described using a shift:

$$\gamma = \frac{\Delta x}{h}, \tag{1.10}$$

where Δx is the displacement of the upper side, mm; h is the height of the rectangle, mm.

Consider the deformations of the triangle δ_T and the rectangle δ_R, represented by rods with moment of inertia I, length L, and cross section A:

$$\delta_T \approx \frac{P \cdot L}{EA};\ \delta_R \approx \frac{P \cdot L^3}{48EI};\ \delta_R > \delta_T, \tag{1.11}$$

where P is force, N; E is Young's modulus of the material, MPa.

Under the action of the force P applied to the top of the triangle, the rods work mainly in tension and compression. In the case of a rectangle, the force P is distributed along the edge, so individual rods (especially the upper and side ones) are additionally bent. Their moments I may not be sufficient to counteract the deflection δ_R, and the rectangle will show larger deformations compared to the triangle.

Next, the deflection of the systems under the action of a uniformly distributed load $P = q(x)$ is analyzed (Fig. 1.15): one consists of triangular elements (triangular lattice – model *a* in Fig. 1.15), and the other – of rectangular elements (rectangular lattice – model *b* in Fig. 1.15).

The differential equation for the deformation of a triangular system, based on the principle of stretching and compressing rods (Hooke's law), taking into account stiffness and load transfer between adjacent elements, could be written in the form:

$$EA\frac{d^2u_i}{dx^2} = P_i - k\left(u_i - u_{i+1}\right) - C\frac{du_i}{dt}, \quad \forall i \in [1, N], \tag{1.12}$$

where $u(x)$ is the horizontal movement of the element as a function of the x coordinate; k – stiffness coefficient of the connection between adjacent triangles, N/mm; $u_i - u_{i+1}$ – difference in displacements between adjacent elements, mm.

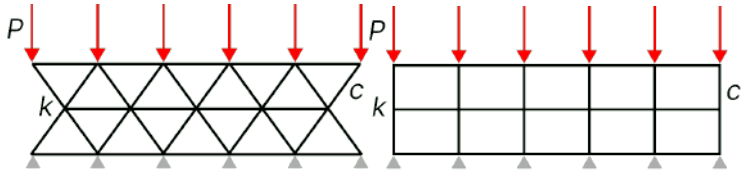

Fig. 1.15. The loading scheme of the rod lattice: *a*) triangular; *b*) rectangular

If the triangle receives vertical loads, its rigid structure compensates for them through the tension or compression of the diagonal rods with a corresponding horizontal displacement of the nodes. This explains the nature of the horizontal displacement $u(x)$.

For a rectangular lattice, each element is prone to bending since there are no diagonal elements that would stabilize the structure, as in a triangular system. Thus, one could consider the Euler-Bernoulli bending equation of the beam for each element, taking into account the damping to account for the dynamic behavior and energy loss in the system:

$$EI\frac{d^4w_i}{dx^4} = q_i\left(x\right) - k\left(w_i - w_{i+1}\right) - C\frac{dw_i}{dt}, \quad \forall i \in [1, N], \tag{1.13}$$

where $w(x)$ is the vertical deflection of the element as a function of the x coordinate; $q_i(x)$ – distributed load on rods, N/mm; $k(w_i - w_{i-1})$ – stiffness of connections between elements (takes into account how the deflection of one element affects the deflection of the adjacent one), N; N is the number of elements providing N interconnected equations.

The dynamic damping coefficient C could generally be written as:

$$C = C_0\left(1 - \alpha \cdot \omega^2\right), \tag{1.14}$$

where C, C_0 – dynamic and basic damping coefficient for a triangular/rectangular system, N·s/mm; α is a correction factor for taking into account the effect of vibrations (takes into account the influence of the vibration frequency and has units of measurement that compensate for the quadratic influence of the angular frequency (characterizes the frequency with which the system oscillates around its equilibrium state), s^2; ω is the angular speed of system vibrations, rad/s.

The value of ω is different for triangular and rectangular systems, so the difference between the damping coefficients could be written as:

$$\Delta C = C_T - C_D = C_0\left[\left(1-\alpha\cdot\frac{EA}{mL}\right)-\left(1-\alpha\cdot\frac{EI}{mL^3}\right)\right], \qquad (1.15)$$

where m is the mass of the rod, kg.

Prospects for advancing the above equations include taking into account nonlinearity of stiffness and damping, as well as delayed responses to loads. To model nonlinear stiffness, one could use the extended Hooke's law:

$$F = k_1 x + k_2 x^2 + k_3 x^3, \qquad (1.16)$$

where F is force, N; x – deformation, m; k_1, k_2, k_3 are stiffness coefficients that describe linear and non-linear components.

Damping could also be non-linear. Higher-order speed-dependent damping models are commonly used, such as:

$$C(u) = C_0 + C_1\left(\frac{du_i}{dt}\right)^2, \qquad (1.17)$$

where C_1 is a coefficient that takes into account the nonlinear effect, which increases with an increase in the rate of deformation, N·s/mm.

The time delay could be described in terms of additional terms that account for system memory or hysteresis effects. One method is to use models such as the Maxwell model or the Kelvin-Voigt model:

$$\sigma(t) + \tau\frac{d\sigma(t)}{dt} = E\left(\varepsilon(t) + \lambda\frac{d\varepsilon(t)}{dt}\right), \qquad (1.18)$$

where $\sigma(t)$ is the stress in the system, MPa; $\varepsilon(t)$ – strain; τ, λ are parameters that describe viscoelasticity (system reaction delay), s.

The complete equation for one element of the structure within the framework of the system, taking into account all nonlinear effects, takes the form:

$$EA\frac{d^2u_i}{dx^2}+\tau\frac{d}{dt}\left(EA\frac{d^2u_i}{dx^2}\right)= \\ =Pi-\left(k_1\left(u_i-u_{i+1}\right)+k_2\left(u_i-u_{i+1}\right)^2\right)-\left(C_0+C_1\left(\frac{du_i}{dt}\right)^2\right)\frac{du_i}{dt}. \quad (1.19)$$

Let's turn to the equation that describes the behavior of the entire system, taking into account both linear and nonlinear effects of stiffness and damping. For a system of N triangles, equation (1.19) will look like a system of differential equations, which could also be represented in the form of a matrix form for compact notation:

$$J\ddot{u}+C_0\dot{u}+C_1\left(\dot{u}\right)^2+K_1u+K_2\left(u\right)^2=Y, \quad (1.20)$$

where J is the diagonal mass matrix of each element (moment of inertia or rod mass); $C(u')$ is a damping matrix that takes into account both linear and non-linear damping effects (may include dynamic coefficients C_0 and C_1); $K(u)$ is the stiffness matrix, which includes linear and nonlinear elastic properties (coefficients k_1 and k_2). C_0 is the basic damping matrix, and C_1 is the matrix of coefficients that takes into account nonlinear damping (dependence on displacement speed); where K_1 is a linear stiffness matrix (for linear connections between elements), and K_2 is a matrix for taking into account nonlinear effects (for example, for cases where the displacement between elements is significant). Numerical methods such as Newton-Kant methods or direct integration using explicit and implicit schemes could be used to solve the system. In this study, an analytical technique for simulating natural tests is proposed, which is as close as possible to real physical tests without conducting them. This approach makes it possible to carry out multi-iteration strength optimization of the body structure in the FEA environment and precedes laboratory certification with the destruction of elements of full-scale prototypes of the bus. The above mathematical modeling is an effective way of pre-predicting the optimal configuration of the sides of the bus body. The next step is FEM calculation based on an iterative

approach. We shall form the unified boundary conditions for the analysis of the object of research – the beam model of the body frame of the bus "Ukrautobusprom – 4289" in the Ansys Static Structural environment in a rectangular (initial) and triangular configuration. On the example of the T-T (Triangular-Torsion) mode, let's consider the peculiarities of the problem statement (Fig. 1.16):

– a model with triangular (Triangular) window openings of the side walls and roof slope;

– a "Fixed Support" tie (tag A, Fig. 1.16) is attached to the right front wheel (the mounting flange of the air cylinders of the suspension), and the left wheel is suspended without a support, which simulates the torsion mode;

– the suspension of the rear wheels is limited in vertical movement – a yoke of the “Displacement” type (tags B and C, Fig. 1.16);

– distributed masses (spheres in Fig. 2) according to the technical documentation: Powertrain (1315 kg), Front (220 kg), Driver (75 kg), Standing passengers (3808 kg), Seated passengers (1972 kg), Rest (3055 kg), and the body weight (2400 kg);

– Standard Earth Gravity (9.806 m/s^2) with the coefficient of dynamism k_d=1.0.

– Material – steel S235 (yield strength σ_y = 252 MPa; Young's modulus=2.099×10^5 MPa, tensile ultimate strength=428 MPa, tangent modulus=1180 MPa) with "Bilinear Isotropic Hardening" (stress-strain curve). Material data was imported from Granta EduPack into Ansys.

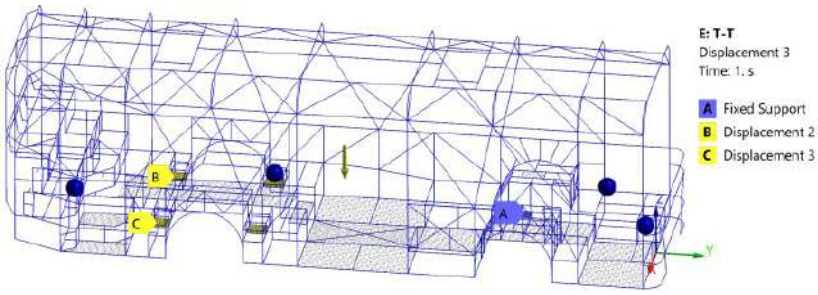

Fig. 1.16. Boundary conditions of the Ansys model under T-T mode

In total, 8 test modes were analyzed (Table 1.2), among which 4 relate to static load on bending (Bending) and torsion (Torsion) and another 4 simulate UNECE R100/R110 conditions. Static bending modes

assume a value of k_d = 2.0, i.e., the loads double, but the bus does not have overhanging wheels (it rests on all 4 wheels). Modes for simulating R100/110 are focused on the strength of the roof and are based on the dynamic coefficient acting in the horizontal direction: k_{hd} = 5.0 transversely or k_{hd} = 6.6 longitudinally. The acceleration is applied to the air conditioning system (1250 kg) and to the electric batteries on the roof (1500 kg) or to the gas cylinder equipment (Fig. 1.17). The batteries apply to buses with hybrid or fully electric traction (UNECE R100).

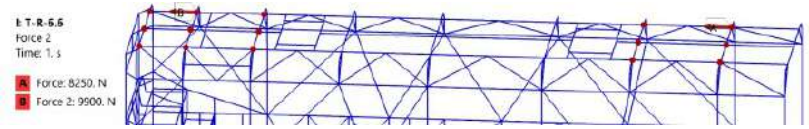

Fig. 1.17. UNECE R100/R110 modeling conditions (mode T-R-6.6)

For example, under the T-R-6.6 torsion mode with triangular window openings (conditionally, they could be called "triangular"), the load from the battery is 9900 N, and the conditioning is 8250 N, taking into account k_{hd} = 6.6.

Table 1.2

Bus body frame test modes in Ansys

Mode	Frame	Type	k_d	k_{hd}	Conditioning, kg	Batteries, kg
R-B	rectangular	bending	2	1	–	–
R-T	rectangular	torsion	1	1	–	–
T-B	triangular	bending	2	1	–	–
T-T	triangular	torsion	1	1	–	–
R-R-6.6	rectangular	R100/110	1	6.6	1,250	1,500
T-R-6.6	triangular	R100/110	1	6.6	1,250	1,500
R-R-5	rectangular	R100/110	1	5	1,250	1,500
T-R-5	triangular	R100/110	1	5	1,250	1,500

The mesh of the beam model with triangular window openings (Fig. 1.18) consists of 13194 elements (Elements) and 21250 nodes (Nodes).

The model with rectangular window openings has 12,726 elements and 20,338 nodes. Both values are about 2–3 mathematical orders lower than the similar Solid model, which significantly simplifies the process of iterative optimization in the early stages of body design.

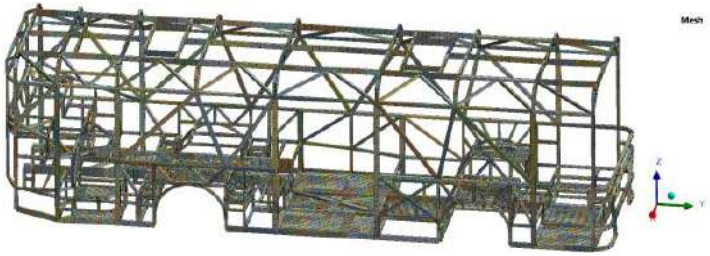

Fig. 1.18. Grid of finite elements of the model under T-T mode

1.2.3. Results regarding the effect of triangular window openings on body strength

A comparison of the Mises stress results of the classic model with rectangular (map *a* in Fig. 1.19) and triangular (map *b* in Fig. 5) openings showed that the maximum stresses σ_{max} decreased from 276.43 to 230.13 MPa, and the average σ_{ave} from 22.34 MPa to 18.88 MPa.

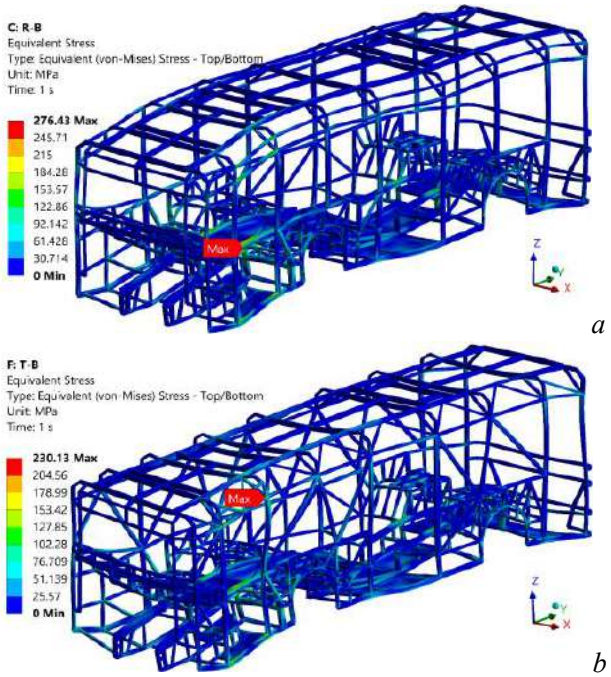

Fig. 1.19. Mises stress maps under the following mode: *a*) R-B; *b*) T-B

The location of σ_{max} has also changed – the max tag (Fig. 1.19) has migrated from the floor spar to the roof frame (rear door opening). Consolidated data are given in Table 1.3.

We shall compare the R-T and T-T simulation modes of hanging one of the wheels (static torsion) on the basis of the maximum displacement maps (Fig. 1.20). When switching from R-T to T-T, the maximum values halved: from 18.77 mm to 9.24 mm. This indicates a significant increase in the rigidity of the body. The theory states that the material begins to plastically deform in locations where the Mises stress (σ_{mis}) becomes equal to the ultimate stress, that is, the yield strength (σ_y). Thus, the safety factor ($SF_{min} = \sigma_y/\sigma_{mi}$) should be greater than 1. So, the value of SF_{min} left the dangerous zone (below 1.0) in both cases and increased from 0.92 to 1.10 when transitioning from the R-B to T-B mode (+19.57 %), and from 0.99 to 1.03 for the case from R-T to T-T (+4.04 %).

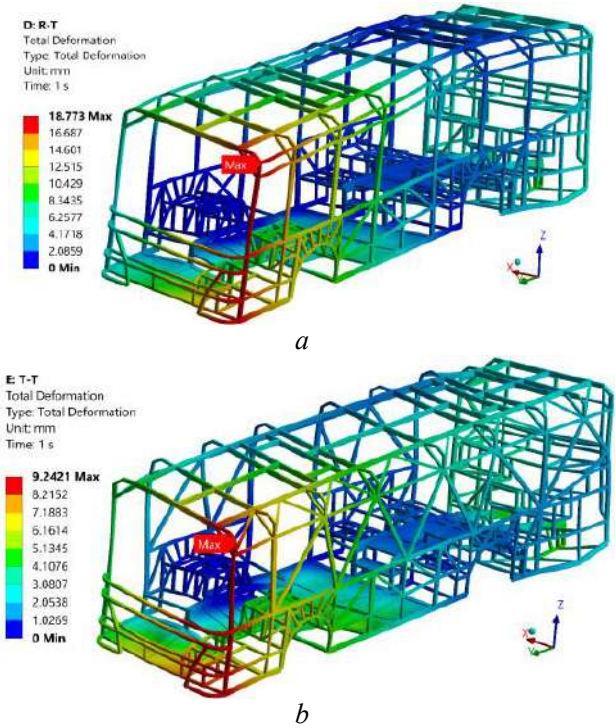

a

b

Fig. 1.20. Maps of movements under the following mode: *a*) R-T; *b*) T-T

Simulation of tests for compliance with UNECE R100/R110 certification requirements began with checking the body's ability to withstand longitudinal loads from the air conditioner and batteries on the roof (Fig. 3) taking into account $k_{hd} = 6.6$.

The R-R-6.6 model with a rectangular design of the window openings is much more pliable – the loss of shape is well observed relative to the initial undeformed state (*a* in Fig. 1.21).

a

b

Fig. 1.21. Mises stress maps under the following mode:
***a*) R-R-6.6; *b*) T-R-6.6**

The stress σ_{max} under the R-R-6.6 regime is almost 33 MPa higher than under T-R-6.6 (*b* in Fig. 1.21) with triangular window openings (177.72 vs. 144.8 MPa). Average stresses σ_{ave} decreased from 13.49 to 9.74 MPa. The assessment of the maximum stresses σ_{max} of the key pillars of the right side shows a reduction from 115.44 MPa (*a* in Fig. 1.22) to 89.63 MPa (*b* in Fig. 1.22. Average stresses decreased from 26.52 to 11.33 MPa.

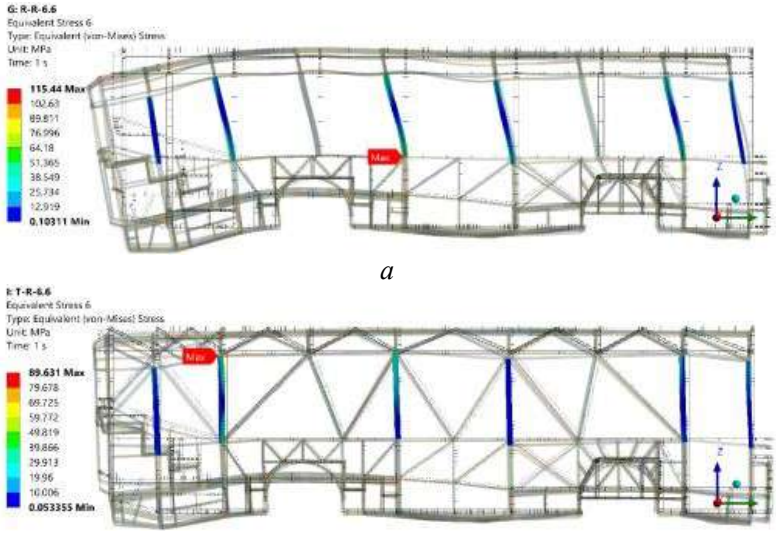

a

b

Fig. 1.22. Mises stress maps of the key pillars of the right side under the following mode: *a*) R-R-6.6; *b*) T-R-6.6

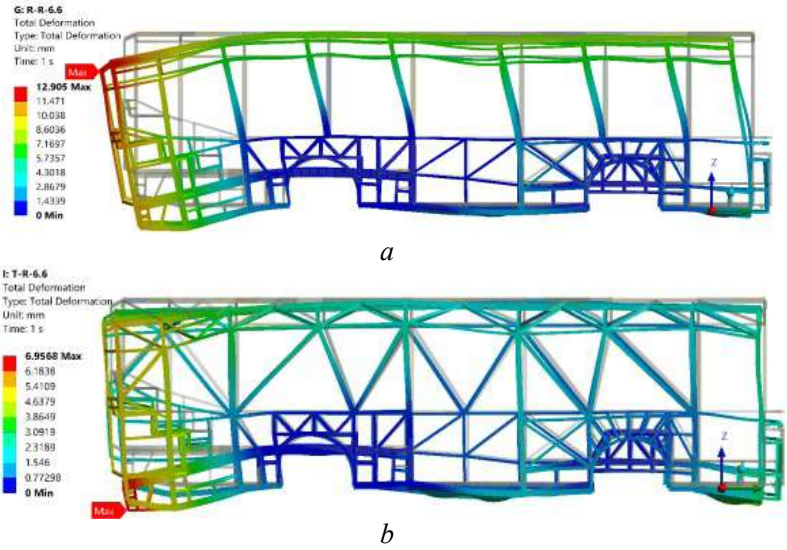

a

b

Fig. 1.23. Maps of deformations under the following mode: *a*) R-R-6.6; *b*) T-R-6.6

The longitudinal stiffness of the structure could be judged on the basis of displacement maps – the maximum values of δ are 12.91 mm under the R-R-6.6 mode (*a* in Fig. 1.23) and 6.96 mm under T-R-6.6 (*b* in Fig. 1.23). To understand: in the Ansys environment, the "Deformations" indicator, which is measured in mm, is responsible for displacement. In the classical sense, deformations are a relative quantity in mm/mm, but in Ansys they are termed "Strain". In the following, the term "deformations" is used in accordance with Ansys terminology (δ, mm).

The transverse stiffness of the body is proposed to be evaluated based on the results of deformations δ under the R-R-5 and T-R-5 modes: 13.05 versus 10.83 mm (Fig. 10). The maximum stresses σ_{max} decreased from 187.3 to 157.2 MPa.

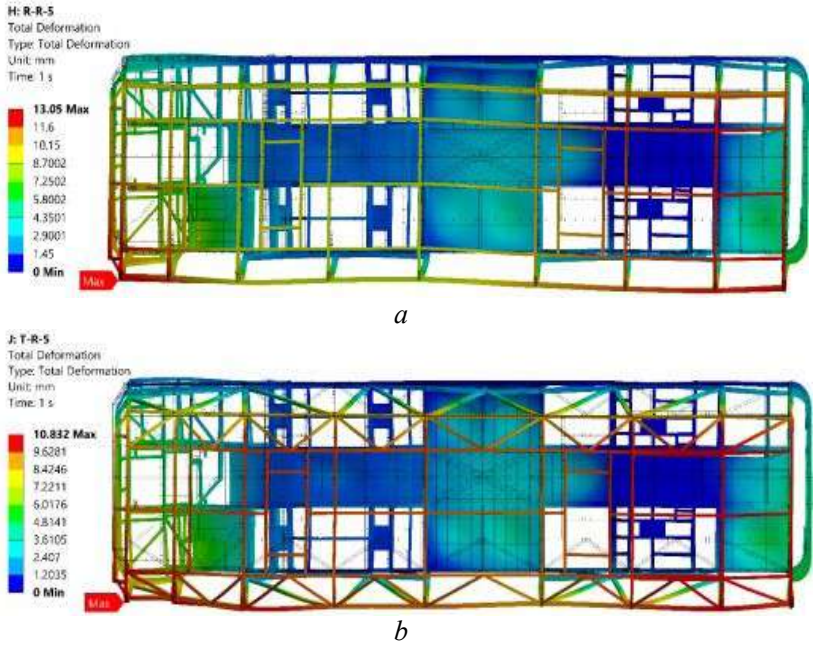

Fig. 1.24. Maps of deformations under the following mode: *a*) R-R-5; *b*) T-R-5

The frontal view of the body frame shows transverse deformations, which are important in view of the lateral safety of passengers – the trapezoid of the remaining interior space (Fig. 1.25).

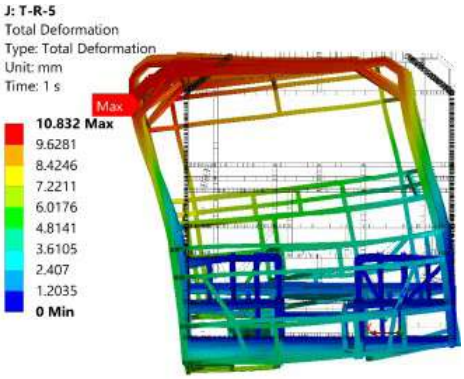

Fig. 1.25. Frontal deformation map under T-R-5 mode

The given maps of *SF* relative to the yield strength σ_y = 252 MPa for the selected regimes (Fig. 1.26) are an effective applied method for assessing the uniform strength of the structure, primarily for engineers. Uniform strength is directly related to the material consumption, which means the cost of the bus, the body of which makes up at least 30 % of the total cost of the vehicle.

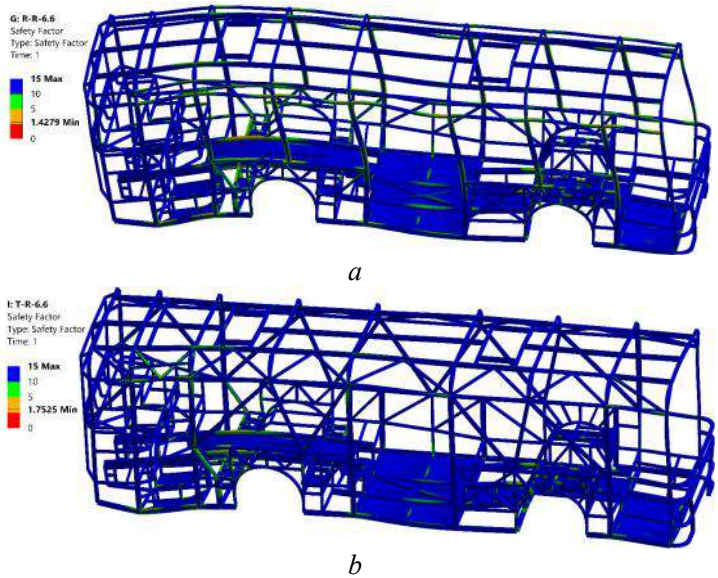

a

b

Fig. 1.26. *SF* maps under the following mode: *a*) R-R-6.6; *b*) T-R-6.6

Based on the presented *SF* maps, a significantly larger area of green and orange color (*SF* below 5) is clearly observed under the R-R-6.6 regime (*a* in Fig. 1.26) than under T-R-6.6 (*b* in Fig. 1.26). The uniqueness and practical benefit of the *SF* tool in Ansys is the ability to set the extreme stress threshold (Stress Tool>Stress Limit Type>Custom Value) relative to which the value of the safety factor would be calculated. For example, let's set a threshold equal to 50 MPa. If it is exceeded, the elements of the model acquire a red color. The effect is well observed when comparing the modes (Fig. 1.27): R-R-6.6 has a larger red area (Fig. 1.27, *a*), and the value *Sf*min = 0.28, which is lower than T-R-6.6 (Fig. 1.27, *b*), where *SF*min = 0.35. The visual availability of the stress state simplifies the selection of alternative materials with a different yield strength for individual elements of the model (for example, reinforcement using S275 steel).

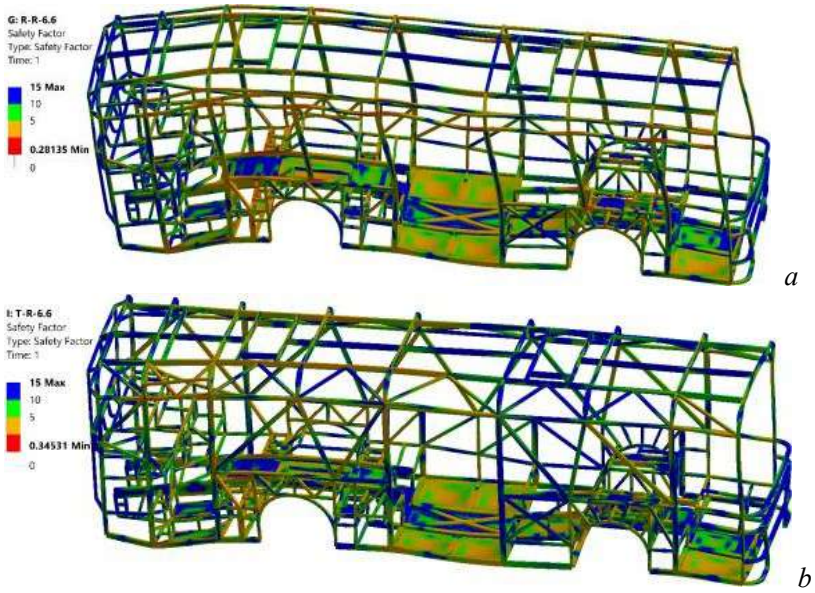

Fig. 1.27. Maps of *SF* relative to σ = 50 MPa under the following mode: *a*) R-R-6.6; *b*) T-R-6.6

The consolidated values of displacements δ and stresses (maximum σ_{max} and average σ_{ave}) characterizing the effectiveness of the proposed design solution (triangular openings) are summarized in Table 1.3.

Under all analyzed modes (Table 1.3), the relative indicators σ_{max}, $\Delta\sigma_{ave}$ and $\Delta\delta$ have a minus sign, which confirms the corresponding reduction of stresses and deformations when switching to a triangular system of window openings.

Since the stress-strain indicators of specific models of buses are a trade secret of their manufacturers, and no direct analogs with triangular structures were found among the analyzed contemporary works, it is not possible to compare our results with actual buses.

Table1.3

Consolidated results of structural optimization of the bus body frame

Mode	R-B	T-B	R-T	T-T	R-R-6.6	T-R-6.6
σ_{max}, MPa	276.43	230.13	254.44	247.18	177.72	144.8
$\Delta\sigma_{max}$, %	–16.75		–2.85		–18.52	
σ_{ave}, MPa	22.34	18.88	14.62	11.54	13.49	9.74
$\Delta\sigma_{ave}$, %	–15.49		–21.07		–27.80	
δ, mm	18.91	13.48	18.77	9.24	12.91	6.96
$\Delta\delta$, %	–28.71		–50.77		–46.09	
SF_{min}	0.92	1.10	0.99	1.03	1.43	1.75
ΔSF_{min}, %	+19.57		+4.04		+22.38	
SF_{ave}	12.02	12.59	13.41	14.02	13.51	14.29
ΔSF_{ave}, %	+4.74		+4.55		+5.77	

The above-mentioned LAZ-360 model, in fact, like vehicles of other manufacturers, had a different layout, dimensions, center of mass characteristics from the object of research, so any comparison with them would be incompatible. In general, a single approach to the assessment of body SSS is adopted in the industry: measurement of deformations and stresses relative to the yield point, assessment of SF, and material consumption.

The biggest advantage of the transition from the "rectangular" R-B mode to the "triangular" T-B mode is the removal of the body truss from the zone of plastic deformations (σ_y = 252 MPa) to the elastic limit (the range of Hook's law). The maximum stresses σ_{max} decreased from 276.5 to 230.1 MPa (Fig. 1.19), and the safety factor SF_{min} increased from 0.92 to 1.10 (Table 1.3), which may indicate the safety of the structure from the point of view of passive safety and resource tests. The location σ_{max} also changed (Fig. 1.19) – the extremum of stresses migrated from the floor spar to the roof frame (rear door opening). This

behavior is extremely positive because the main function of the specified spar is to hold the engine with the transmission, where there are additional loads in the form of vibrations, inertia, etc.

The R-T and T-T modes of simulating suspension of one of the wheels (static torsion) demonstrate a reduction of the maximum displacements by half: from 18.77 mm to 9.24 mm (Fig. 1.20). Both values correspond to the angle of the glued windshield, which directly determines the safety of its operation: moving the window opening by more than 10–15 mm could cause cracks in it. The value of $SF_{\min}$ left the dangerous zone (below 1.0) and increased from 0.99 to 1.03 during the transition from R-T to T-T mode (Table 1.3).

In order to comply with the new EURO 7 environmental regulations from July 1, 2027, it is economically more profitable for diesel buses to switch to electric traction. Systems such as exhaust aftertreatment (SCR, DPF), emissions monitoring (RDE), low-emission braking are more expensive than electric power and drive. Conversion of the existing fleet of city low-floor buses to electric traction involves certification according to UNECE R100 with verification of the strength of the upper part of the body. The peak stresses σ_{max} of the key struts of the right side (less rigid due to the presence of doors) decreased from 115.44 MPa to 89.63 MPa (Fig. 1.22). The maximum values of deformations δ decreased from 12.91 mm (mode R-R-6.6) to 6.96 mm (T-R-6.6) (Fig. 1.23) and also moved from the roof to the floor frame (rear overhang). This is extremely positive from the point of view of passive safety. This could also be seen from the results of the $SF_{\min}$ maps (Fig. 1.26): the area of orange and green spots has significantly narrowed, which indicates the uniform strength of the frame.

The transverse stiffness of the body is estimated by the results of deformations δ under the R-R-5 and T-R-5 modes: 13.05 vs. 10.83 mm (Fig. 11), recorded at the level of the over-window bar of the side walls (the upper corner of the cross-section of the bus body). Such a tendency to decrease is positive because the trapezoid of the remaining space of the cabin, determined by the deformations of the inter-window struts of the sidewalls, dictates the level of passive safety (room space at head level). The same trapezoid is the basis of UNECE R66 regarding the assessment of passive safety under side rollover conditions of a bus. The maximum stresses of the body frame σ_{max} decreased from 187.3 to 157.2 MPa (Table 1.3) when switching to the T-R-5 regime, that is, the structure is completely within the limits of the elasticity of the material (the scope of Hooke's law).

Speaking about the effectiveness of the optimization measures (transition from the "rectangular" to the "triangular" structure of the body sides), one should note the modes T-T and T-R-6.6, under which deformations were reduced by 50.77 and 46.09 %, respectively (Table 1.3). Taking into account the weight reduction of the optimized body relative to the initial one (–37 kg), it is possible to unequivocally state the expediency of the carried-out structural optimization. The above results of a reduction in stress values, deformations, and an increase in the safety factor in all the analyzed modes could be explained by the fact that a triangle is a more rigid shape than a rectangle. This is determined by its geometric stability – the impossibility of changing the shape while preserving the area without changing the length of the sides and angles.

Our solutions resolve the task to unify bus bodies for the installation of conventional diesel power plants or adaptation to the BEB and FCEB schemes, which significantly add mass due to batteries. The triangular structure of the sidewalls is able to compensate for additional loads under the modes of daily operation or certification according to UNECE R100 without increasing the material consumption of the body.

The reviewed literature is entirely based on classic "rectangular" bodies and mainly consider solutions for optimizing the selection of alternative cross-sections or manufacturing materials. Unlike [24–32], which consider typical rectangular structures, the advantage of the current work is the use of triangular elements. Work [35] describes the use of trapezoidal windows, which is close to the topic of current research; however, the shape of a trapezoid, as a quadrilateral, is less rigid than a triangular one.

The limitations of the proposed structural solution regarding the replacement of rectangular window openings with triangular ones are the increased complexity of the body manufacturing technology. In the case of a curvilinear shape of the sidewall profile, conventional vertical racks have the same radius of rounding, and in one plane (transverse), and allow the use of a common pipe bender. The transition to diagonal racks, which as a result form triangular window openings, requires simultaneous bending and twisting of pipes. The situation is further complicated by the fact that they are of different lengths according to the sections of the bus, and therefore there is no question of a single pipe bender. Cutting diagonal tubes and welding them is also significantly more difficult compared to the conventional rectangular configuration of the sidewalls of the body. The problem could be easily solved by

switching to a rectangular cross-section of the bus, which is a modern trend, taking into account the need to minimize production costs and reduce the cost of the final product.

The shortcomings of the study include the lack of analogs – any results of studying the stress-strain state of other models of buses with triangular structures. The objectivity of the reasons for this was substantiated by us above but it should be noted that, under the conditions of the appearance of modern similar scientific publications, one of the priority directions of the development of the current work will be the comparison of our results regarding the SSS of bodies. More applied shortcomings of the current study include the absence of results of forced body oscillations under the considered bending and torsion modes, as well as data on the vibration resistance of the roof truss. In addition, there is a need to check the impact of side glued windows on the final rigidity of the body under different approaches to their installation, which, in fact, is a limitation of this study. In one version, the windows could be triangular (occupying the area defined by the window bars), and in the other – rectangular. In the latter case, they will be glued on top of the triangular window openings with a flywheel so that the inclined racks will cross the windows diagonally from the inside of the cabin. Thus, visually, the bus will retain its manufacturability and at the same time look quite conventional – with classic rectangular windows but will remain innovative with its "triangular" body structure. In addition to modeling of glazing, the simulation of side and frontal impact tests (UNECE R66 and R29) are possible avenues to advance our research that, at the same time, are its limitations.

Conclusions

1. The most common modes of static bending (k_d = 2.0) and torsion (k_d = 1.0 if one of the wheels hangs out) during daily operation showed a reduction in stress by 16.75 % when going from R-B to T-B and by 2.85 % – from R-T to T-T. The most significant achievement is to remove the maximum stresses σ_{max} from the zone of values of plastic deformations (yield point σ_y = 252 MPa), that is, the work of the body frame in the zone of elasticity (Hooke's law). The value of the safety factor SF_{min} also exceeded 1 under both modes of the "triangular" model (1.10 in T-B and 1.03 in T-T). The stiffness of the frame could be estimated by the deformation index δ, which decreased by 28.71 % under the

bending mode (T-B) and by 50.77 % under the torsion mode (T-T). The obtained values of δ in the optimized model do not exceed 10 mm, which ensures normal operation of glued windows when the body is skewed (δ = 9.24 mm under the T-T mode).

2. Due to the necessity of the inevitable compliance with the environmental requirements of EURO 7, existing city fleet during electrification is automatically subject to certification according to those UNECE Regulations that were not initially foreseen. Being originally diesel, buses when converted to electric traction (installation of batteries) must comply with regulatory requirements R100. Reduction of σ_{max} occurred by 18.52 and 16.07 % when the body structure was changed to "triangular" under the T-R-6.6 and T-R-5 modes, respectively. The average stresses σ_{ave} managed to be reduced by 27.80 % (to 9.74 MPa) when switching to the T-R-6.6 mode, which allows us to judge the possibility of improving the material consumption by selecting alternative profiles of smaller cross-section. The total mass of the "triangular" body frame has become even lower than the "rectangular" version by 37 kg. Under the T-R-6.6 mode, deformations δ were reduced by 46.09 %, and under T-R-5, they amounted to only 10.83 mm, which is very positive in terms of passive safety – the preservation of the trapezoid of the remaining cabin space.

1.3. Thermal and stress-strain state of friction pairs in ventilated disc brakes of lightweight vehicles

Scientific and technological progress has provided the industry with significant theoretical developments in the field of heat and mass transfer, for example, in spheres such as tribology or thermodynamics, which have developed over several decades with progress in many sectors: nuclear energy, aerospace and aviation, automotive, etc. Modeling of problems related to the phenomenon of heat or mechanical energy transfer in general and through friction pair contacts in particular, is of primary importance in the design of relevant units, for example, disc brakes of vehicles. Many authors raised such topics in their publications as: design and thermal analysis of disc brake for minimizing temperature [41]; effect of cross-drilled hole shape on crack of disc brake rotor [42]; thermal analysis of disc brakes using FEA [43–44]. In fact, it is not only about the development of new models of brakes, but also about the selection of optimal options for systems for existing vehicles, taking into

account their class, type and operating conditions. As you know, brakes are a device that creates frictional resistance to move a system element (rotor) to stop further movement, so we can get acquainted with the modeling and analysis of FSAE car disc brake using FEM in [45] and discover the enhancement in design and thermal analysis of disc brake rotor in [46]. Brakes are a mechanism used to reduce the speed or stop the cycle of movement of a vehicle. Long-term use of the brake in a lightweight vehicle (bicycle and motorcycle) causes heating during the braking process [47–49], so that the rotor is deformed (jammed between the pads or breaks) due to high temperature and thermal expansion. Actually, the thermal analysis of disc brake is the topic of publication [47], which could be effectively supplemented by the study on crack initiation at small holes of one-piece brake discs in [49]. In the research [10] authors present the velocity and relative contact size effect on the thermal constriction resistance in sliding solids. Topic of investigation of temperature and thermal stress in ventilated disc brake based on 3D thermomechanical coupling model raised is similar to our work and makes sense to be researched. Our goal is to proceed the analysis of the behavior of the system under conditions of long-term friction at constant pressure with a corresponding increase in temperature and volume of the model, as well as with a variable load in the system (from the hydraulic cylinder), which leads to blocking of the brakes with plastic disc deformations (determination of stresses according to Mises).

1.3.1. Results of studies under constant load

A disc brake is a system consisting of a brake disc (rotor), brake pads and calipers actuated by a hydraulic cylinder. The brake disc rotates with the wheel and the pads mounted on the brake calipers clamp it to stop or slow the wheel (Fig. 1.28).

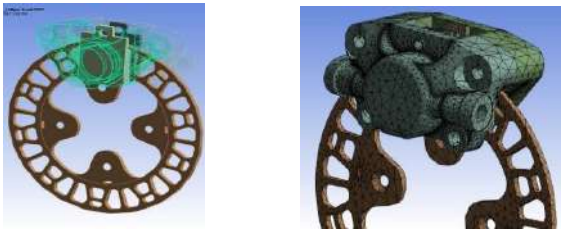

a *b*

Fig. 1.28. Solid disc brakes model: *a*) isometry; *b*) FE grid of the model

Brake pads generate heat through friction, converting kinetic energy into heat to reduce the total kinetic energy of the vehicle. Thus, due to the thermal energy generated during the braking process, the temperature of the disc on the contact part increases and generates fatigue stresses accumulation, causing cracks or plastic deformations that reduce the service life of the disc.

Usually, ventilated discs are used to improve the efficiency of heat dissipation, because they have channels for air circulation: the higher the rotational speed of the disc, the higher the centrifugal force, which contributes to the dissipation of heat. To select the optimal brake system according to the target vehicle, it is advisable to determine the required pressure [10–12] from the brake pads:

$$P = \frac{F_d}{S_\mu}, \tag{1.21}$$

where P – pressure between the disc and the pad; F_d – force acting on the disc; S – surface of the pad in contact with the disc; μ – coefficient of friction.

The actual value of the pressing force F_d can be found as follows:

$$F_d = k \cdot \left(M \frac{\nu^2}{2} \right) \Big/ 2 \frac{r}{R} \left(\nu t - \frac{1}{2} \left(\frac{\nu}{t} \right) t^2 \right), \tag{1.22}$$

where k – load factor – 0.3 (corresponding to 30%); M – mass of the vehicle; r – brake disc radius; R – wheel radius; v – vehicle speed.

We apply the following values to the boundary conditions of the calculation: time of the experiment t = 20 s; coefficient of friction μ = 0.2 c; angular velocity w = 3.5 rad/s, which corresponds to a wheel speed of 200°/s. Wheel is rotated due to the hub with the 4 holes for mounting bolts (Fig. 1.28, *a*), where are observed the highest meanings of stress (Fig. 1.29, *b*); the movement of pad Δ is symmetrical and presented in steps (Table 1.4). The initial gap between pads and disc is 1.5 mm. Starting from 0.3 s and until the end of the experiment Δ =1.501 mm – thus, the full contact between friction pairs is simulated.

The FEM model consists of 101529 elements; applied material is Structural Steel (typical characteristics are embedded in Ansys); the

number of time steps is 200 (duration of a step is 0.1 s); the total calculation time on the equipment (2 Intel Xeon processors 24 cores, RAM 48 Gb, NVIDIA GeForce 4Gb video) was 10 hours 42 min.

Table 1.4

Brake pads travel during the experiment (20 s)

Time moment	0 s	0.1 s	0.2 s	0.3 s	20 s
Δ, mm	0	0.75	1.5	1.501	1.501

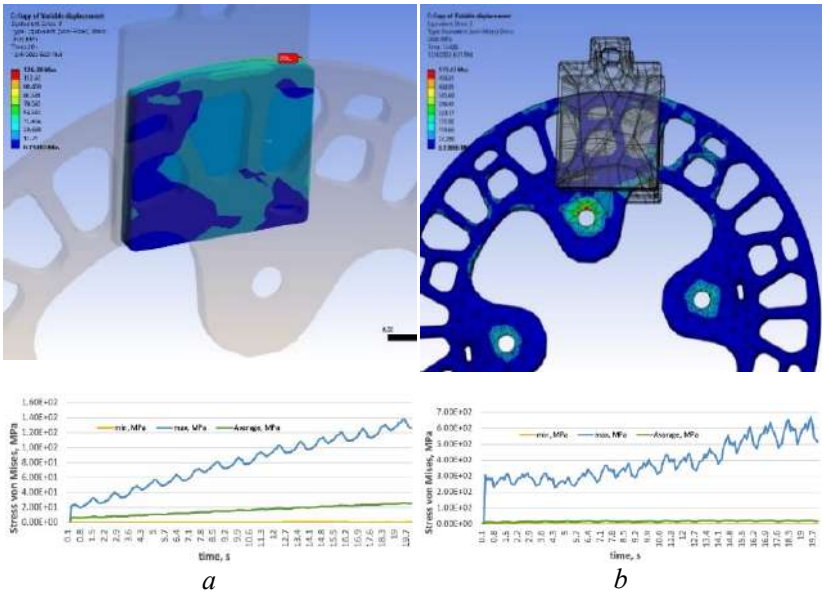

a *b*

Fig. 1.29. Stress in the braking system at a constant load:
***a*) brake pad and stress graph over time;**
***b*) ventilated disc and stress graph over time**

Let's analyze the stress maps of the brake pads and the ventilated disc (Fig. 1.29) – as we can see, there is a stress increase tendency while the experiment continues:

– the pad is pressed to the disc in 0.2 s and its stress increases from 8.3 MPa (caused by reactions from the rotational movement in the holes for mounting bolts attaching the disc to the hub) to 223 MPa

(when Δ reaches 1.501 mm). Further, as the experiment progresses, the stress increases to a maximum of 647 MPa at a time of 18.2 s. The intermediate state of stress at the moment of time 17.4 s is presented in Fig. 1.29, *b* (the curve is “max, MPa”). The curves "min, MPa" and "average, MPa" correspond to the minimally loaded locations of the body and the average value of loads for all its locations, respectively;

– the pad stress increases to 22 MPa in the first 0.2 s (the period of pressing against the disc) and then reaches up to 138 MPa at the time of 19.5 s (Fig. 1.29, *a*).

What should be paid attention to: despite the constant value of the displacement of the pads (it is stable and equal 1.501 mm during the entire experiment lasting 20 s), the stress values fluctuate and increase.

1. Stress fluctuations are explained by the uneven structure of the disc itself (holes in the structure for ventilation): as it rotates, the area of contact with the pad is constantly changing, and thus the pressure and stress change as well. Let's visually check the nature of the pad contact with the disc at different moments of time (Fig. 1.30) – the unevenness of the distribution is dictated by the channels in the disc that affect the contact spot: the position and movement of the contact element determines its condition relative to the target surface associated with it.

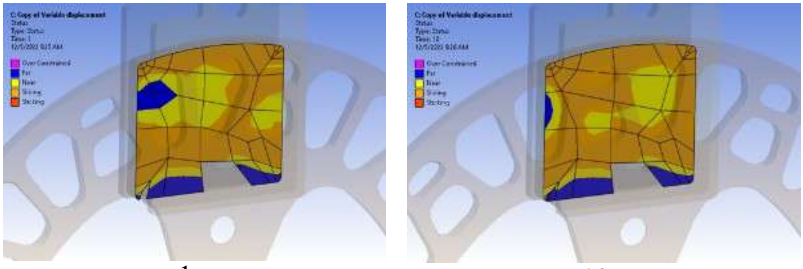

1 s 10 s

Fig. 1.30. Analysis of brake pad contact area at different moments of time

ANSYS monitors each contact element and assigns a status:

– STAT = 0 Open far-field contact (open remote contact) – blue color;

– STAT = 1 Open near-field contact (open near field contact) – yellow color;

– STAT = 2 Sliding contact (sliding contact) – orange color;

– STAT = 3 Sticking contact (sticking contact) – red color.

An element is considered to be in close contact if its integration points (Gauss points or nodal points) are within the code-calculated (or user-defined) distance to the corresponding target surface. This distance is called the pinball area. A pinball domain is a circle (in 2-D) or a sphere (in 3-D) centered around a Gauss point.

The friction coefficient may depend on the relative speed of the contacting surfaces. As a rule, the static coefficient of friction is higher than the dynamic one. ANSYS provides the following exponential friction damping model:

$$\mu = MU\left(1+(FACT-1)\exp(-DC\cdot \nu_{rel})\right), \tag{1.23}$$

where μ – friction coefficient; MU – dynamic coefficient of friction (using the MP command in Ansys); $FACT$ – the ratio of static to dynamic friction coefficients (the minimum value is set by default 1.0); DC – damping coefficient (by default it is equal to 0 and has the unit of dimension time/length), so time has a certain value in static analysis); ν_{rel} – slip velocity calculated by ANSYS. "Friction Decay" shows an exponential decay curve (Fig. 1.31, *a*), where the static coefficient of friction is defined as:

$$\mu_s = MU{\cdot}FACT. \tag{1.24}$$

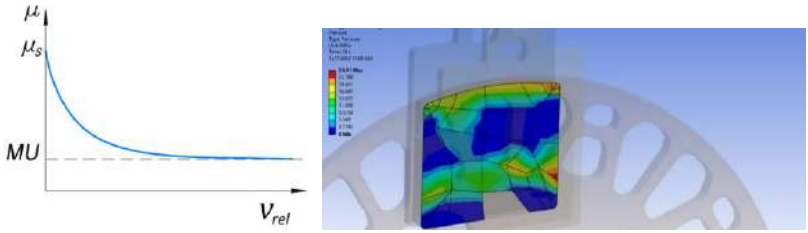

a *b*

Fig.1.31. Research of friction: *a*) exponential curve of friction damping; *b*) pressure map on the pad surface at the time of 20 s

The damping coefficient can be determined if the static and dynamic coefficients of friction and at least one data point are known (μ_1; ν_{rel1}). The equation to describe friction damping can be written as follows:

$$DC = -\frac{1}{\nu_{rel1}}\cdot \ln\left(\frac{\mu_1 - MU}{MU(FACT-1)}\right). \tag{1.25}$$

If no damping factor is specified in the simulation process, and FACT is greater than 1.0, then the friction coefficient will suddenly change from static to dynamic value as soon as the contact reaches the sliding state. It should be noted that such behavior is strongly not recommended, since the gap can lead to convergence difficulties when solving the problem [47–48].

2. Why does the value of stresses in the disc and brake pads increase, if they remain stationary and do not increase the external load from the hydraulic cylinder? By the way, what is the maximum pressure value recorded during the experiment (Fig. 1.32).

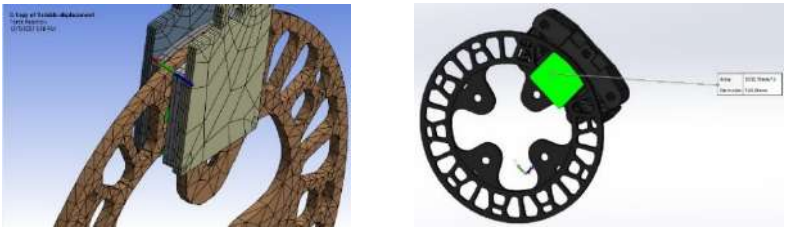

a *b*

Fig. 1.32. Determination of pressure in the disc brake system:
***a*) FEM model with load vector;**
***b*) determination of the brake pad area (SolidWorks environment)**

We have measured the maximum value of the load (Fig. 1.32, *a*) during the experiment in the Ansys environment: 7968.5 N at the time of 18.2 s. The pad area is 1030.78 mm^2 (Fig. 1.32, *b*), which corresponds to a pressure of 7.73 MPa. It's possible to observe a similar value on the graph (Fig. 1.33d – orange color), which shows the average pressure value over the pad area. However, taking into account that the contact area varies, as shown in Fig. 1.30, and can occupy up to 35–40 % of the pad area due to the ventilation holes at certain moments of time, the pressure value increases up to 20 MPa. This is a typical value for disc brakes in automotive and two-wheeled vehicles. Therefore, our experiments with the applied boundary conditions are approaching to the natural tests.

The reason of the stress increase is the thermal expansion of the disc and pads (increase in volume) as a result of heating (Fig. 1.33, *a*, *b*) and internal energy growth (Fig. 1.33, *c*), which leads to a decrease in the gaps between disc and pads with the appropriate pressure rise

(Fig. 1.33, *d*). It should be noted that the increase in the volume of the pad is relatively linear over time, but the disc expands according to a geometric progression – in fact, this already prompts the idea of the feasibility of scientific research on ventilation holes in the structure of the disc, the selection of their optimal configuration, etc.

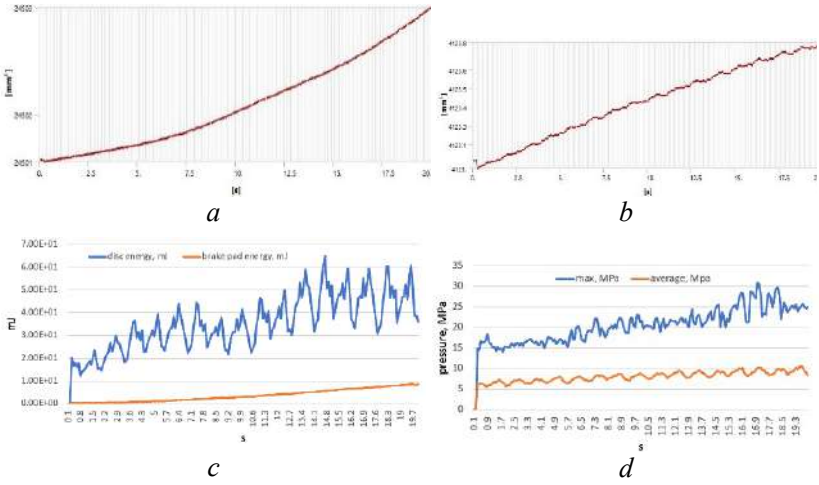

Fig. 1.33. Thermal state analysis of disc brakes:
***a*) volume of the disc; *b*) volume of pads;**
***c*) growth of energy over the friction; *d*) pressure on the pad surface**
(average in area and maximum in locations)

Fig. 1.34 shows temperature maps of the disc at certain moments of time. Thus, the value of the disc temperature during the experiment lasting 20 seconds reached 34.87 °C. It should be understood that the following boundary conditions were applied as a part of our research: temperature $T(x, y, z) = 22$ °C at time $t = 0$ s and zero value of convection (please note that the simulation of moving air masses assumes 5 W/m^{2}C in a static position and around 25 W/m^{2}C – in dynamics) to obtain clean results of body heating and heat flux (Fig. 1.35, *a*, *c*). The value of the pad's temperature reached – 35.04 °C, which is shown on the graph of both elements heating (disc and pads) – Fig. 1.35, *b*. It's quite exciting to observe how close are both graphs (Fig. 1.35, *b*) – heat transfer from pads to rotors could be visually observed by the temperature equalizing between both units at any time moment.

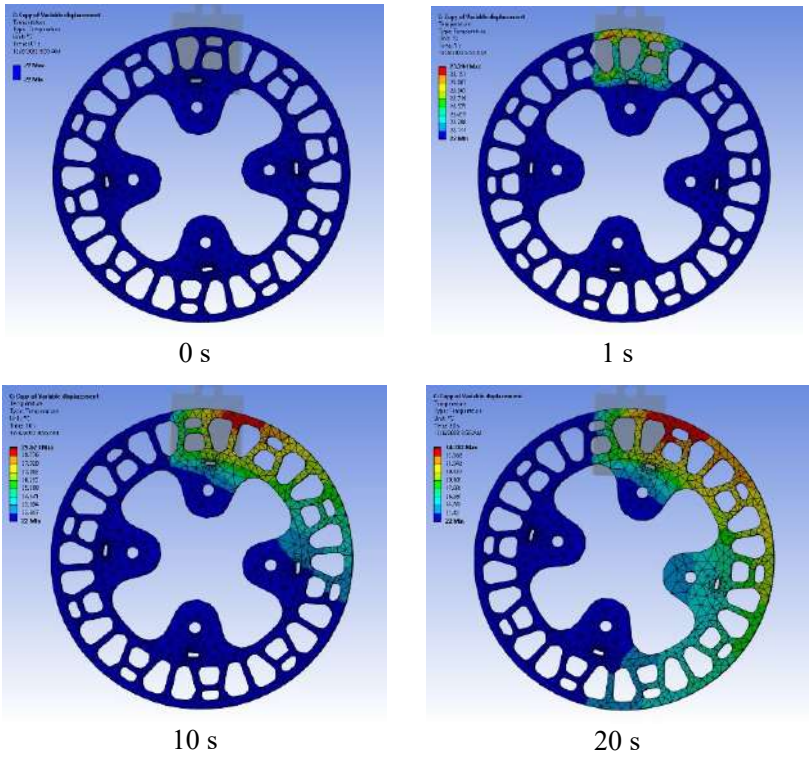

Fig. 1.34. Temperature maps of the brake disc at different times of the experiment

Let's turn to the theory of the thermal state description of the body – the first law of thermodynamics, which shows on the thermal energy saving:

$$C_p\left(\frac{\partial T}{\partial t}+\{\nu\}^T\{L\}T\right)+\{L\}^T\{Q\}=p. \qquad (1.26)$$

In our calculated case, there is no internal pressure source (p = 0), and therefore equation (1.26) will be written as follows:

$$\rho C_p\left(\frac{\partial T}{\partial t}+\{\nu\}^T\{L\}T\right)+\{L\}^T\{Q\}=0, \qquad (1.27)$$

where

$$\{L\} = \begin{Bmatrix} \dfrac{\partial}{\partial x} \\ \dfrac{\partial}{\partial y} \\ \dfrac{\partial}{\partial z} \end{Bmatrix}, \quad \{\nu\} = \begin{Bmatrix} \nu_x \\ \nu_y \\ \nu_z \end{Bmatrix}, \tag{1.28}$$

where $\{L\}$ – vector operator, $\{\nu\}$ – vector speed of the vehicle.

Let's write Fourier's law (1.27) in matrix form:

$$\{Q\} = -[K]\{L\}T, \tag{1.29}$$

where $[K]$ – matrix with the corresponding coefficients K_{xx}, K_{yy}, K_{zz} by axles X, Y, Z, which are equal in all directions for isotropic materials $K_{xx} = K_{yy} = K_{zz}$:

$$[K] = \begin{bmatrix} K_{xx} & 0 & 0 \\ 0 & K_{yy} & 0 \\ 0 & 0 & K_{zz} \end{bmatrix}. \tag{1.30}$$

When combining equations (1.27) and (1.29), we get the following expression:

$$\rho C_p \left(\frac{\partial T}{\partial t} + \{\nu\}^T \{L\}T \right) + \{L\}^T \left([K]\{L\}T \right). \tag{1.31}$$

In general, the typical boundary conditions of thermal calculation can be attributed to:

– surface temperature: $SURF_T$: $T = T^*$;

– thermal dissipation on the surface: $SURF_Q$: $\{Q\}^T \{n\} = -Q^*$;

– convection on the surface: $SURF_C$: $\{Q\}^T \{n\} = h\left(T_p - T_f\right)$,

where $SURF_T$, $SURF_Q$, $SURF_C$ – surface temperature, flow and convection; T^* – the temperature given at the surface; Q^* – the heat flux given at the surface; T_p – surface body temperature; T_f – environment temperature; h – coefficient of convective heat transfer.

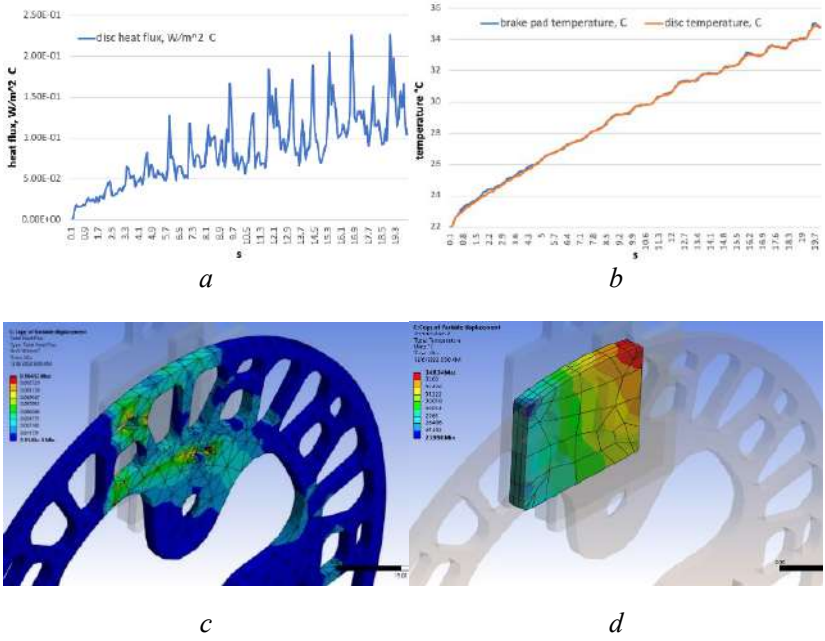

a *b*

c *d*

Fig. 1.35. Heat load of brakes:
***a*) heat flow of the disc; *b*) temperature of the disc and pad;**
***c*) heat flow of the disc at 20 s; *d*) temperature of the pad at 20 s**

In turn, the thermal expansion presented in the graph (Fig. 1.33, *a*) can be described by the following conditions, which are relevant for the behavior of solid bodies:

– thermal coefficient of volumetric expansion (measured in inverse degrees Kelvin, K^{-1}):

$$\alpha = \frac{1}{V}\left(\frac{\partial V}{\partial t}\right). \tag{1.32}$$

If the volume expansion coefficient changes significantly with temperature, then the equations must be integrated:

$$\frac{\Delta V}{V} = \int_{T_0}^{T_0+50} \alpha(T)dT; \tag{1.33}$$

– thermal expansion of the area of a solid body:

$$\Delta S = 2\alpha S_1 \Delta t, \tag{1.34}$$

where T_0 – initial temperature; ΔS – area change (for example, brake pads or disc); S_1 – starting area; Δt – temperature change.

1.3.2. Results of studies under variable load

We have previously considered the behavior of the brake system consisting of a disc and pads under a constant external load (pressure) from hydraulic cylinder on them: the static position of the pads during the entire experiment lasting 20 s and constant travel (Δ =1.501 mm). How will the system show itself if we increase the pressure in the hydraulic cylinder and set the pads movement according to the linear law (Table 1.5).

Table 1.5

Dynamics of brake pads movement during the experiment (20 s)

Moment of time	0 s	0.1 s	0.2 s	0.3 s	1 s	5 s	10 s
Δ, mm	0	0.75	1.5	1.501	1.508	1.548	1.598

This setting of boundary conditions leads to jamming of the brakes, because two factors come into play: the increase in pressure from the side of the pads; the thermal expansion of pads together with the disc. The stress map at the critical moment is presented in Fig. 1.36 – the plastic deformation of the disc is visually observed as a result of an attempt at inertial scrolling. As you can see, the experiment stopped at the 8th second – the further process is a static state of the system and does not require an assessment of its behavior (the disc cools down to the initial 22 °C). Rotor and pad stress trends are demonstrated on Fig. 1.37 – fluctuations on the graph mean the ventilation channels influence on the stress meaning. Additional plasticity of the material during the long-term friction is provided by an increase in temperature as a result of pressure growth – the disc model received 32–37 % higher temperature values compared to the previous experiment (unchanged travel of pads Δ = 1.501 mm). Such results lead to the opinion of the necessity to arrange not only the structural optimization of the disc (ventilation channels), but also force to think about the relevance of using heat-resistant materials for the production of brakes: ceramics, which is a standard point in the premium segment of cars, sports cars, etc.

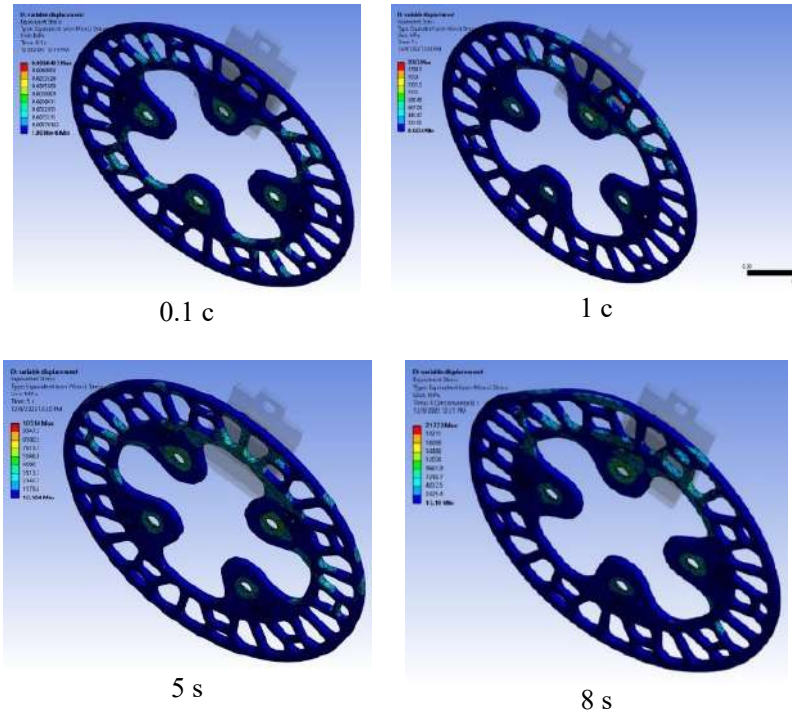

Fig. 1.36. Stress-deformable state of the brake rotor

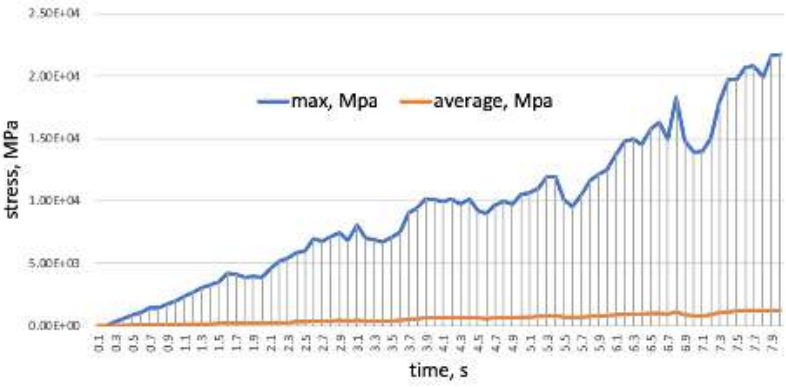

Fig. 1.37. Brake stress under the variable load- disc stress graph

Conclusions

1. The results of thermal behavior and stress-strain state of ventilated disc brakes presented in the work using the ANSYS Coupled Field Transient calculation environment are of a practical nature not only from the point of view of designing new vehicles with the appropriate selection of the optimal brake configuration for them, but also the optimization of existing structures. The research provides such valuable data as: temperature distribution along the rotor and pads during the friction process; heat dissipation, cooling and ventilation activities; selection of suitable materials for the production of friction pairs; creating an optimal configuration of the disc ventilation holes; determination of the required pressure in the hydraulic cylinders, taking into account the mass of the vehicle and the conditions of its operation (speed, convection of the medium, etc.).

2. The results obtained in the conditions of a pads static position during the entire experiment lasting 20 s with their constant travel ($\Delta = 1.501$ mm) allow us to quantitatively assess the influence of thermal expansion on the key performance indicators of the brakes as a result of friction (heating from 22 °C to 35.04 °C). This approach provides an understanding of the necessity to remove heat and ventilate the brakes, because the trends presented in the graphs indicate an exponential rather than a non-linear increase of the disc volume during heating, and suggest the inevitability of jamming / burning of the brakes (depending on the degree of vehicle movement inertia) with prolonged contact of friction pairs.

3. The use of the ANSYS Coupled Field environment in conjunction with the boundary conditions proposed in the work allows you to form your own effective brake modeling methods, which is especially useful in the conditions of small design studios and workshops, which, in fact, are often involved in the production and design of lightweight vehicles: motorcycles, e-bikes, ATVs, scooters, buggies, etc.

1.4. Parametric modelling of control cable fittings geometric configuration with interpolation of FEA results

The steel fittings (caps, claps or hubs) are a typical part of many components and assemblies in the automotive industry and are used, for example, in push-pull remote-control cables that serve to transfer loads from the control body to the controlled one. The practical problem of the

task is that being radially crimped, the fittings (detail in the form of pipe) must have a certain permissible range of stresses/strain in the area of the axial hole and on its outer cylinder surface to be rigid enough and avoid the transfer of unacceptable deformations inside of the cable. The strength analysis is simple at first glance, but in reality, it turns out to be filled with several possible problems and challenges so the fitting must:

– press the conduit (red polymer in Fig. 1.38, *a*) with sufficient force so as not to slip off it (normative tensile load not be less than 100 kgf for the cable);

– should not cause internal conduit deformation that can limit the free movement of the core (the main transmission element in the remote-control cable). Otherwise, the cable has an increased risk of jamming, which is dangerous for the operation of the vehicle.

The problem of calculating the plastic deformation of control cable fittings is related to the conditions of the cables exploitation and appropriate boundary conditions, thus the article [51] is recommended to get acquainted with possible push-pull cable-based actuation cases through experimental results and detailed analysis. The paper [52] introduces a novel push-pull cable-driven technology within the CORBYS rehabilitation system, enabling the creation of high-power-to-weight-ratio assistive devices. In [53], the authors describe the use of cables in UAVs, which is quite valuable for formulating specific boundary conditions for cable loading. Cable loading (as long as fittings are a part of the assembly) can overcome not just static loads but vibrations as well – vibration control of flexible manipulators by active cable tension is a topic of [54]. Quite an actual topic that is close to our scope of research was raised in [55] – fastening characteristics of preformed helical fittings considering the surface effect of transmission lines. As long as the fittings provoke pressure on the conduit, it makes sense to investigate its structure and behavior: the paper [56] – full 3D finite element modeling of spiral strand cables and papers [57, 58] – effect of interwire contact on the mechanical performance of wire rope strand (the part of cable conduit and core). Taking into account that cable fittings have a form of pipe [59], it's recommended to investigate the hoop stress nature [60]. Bilinear Isotropic Hardening as a part of applied Ansys material characteristics is mentioned.

The purpose of our research is to model the optimal configuration of the fitting (Fig. 1.38, *a*) according to the criteria: outer diameter, inner diameter and plasticity of the material depending on the

crimping load. An example of the radially crimped by 8 press elements fitting blank – a rod with a diameter of 20 mm without a hole is shown in Fig. 1.38, *b*. It can serve as a valuable basis for forming an individual stress-strain characteristic that is quite important for the laboratories of the same push-pull cable manufacturers.

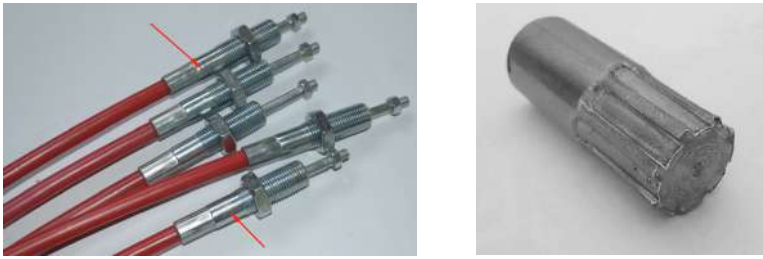

a *b*

Fig. 1.38. Push-pull control cables:
***a*) assembled units; *b*) crimped fitting blank**

Hoop stress, also known as circumferential stress, is the stress that develops in a cylindrical or spherical structure like a tube or pipe when radial loads are applied normally (perpendicular) to the outer surface of the structure. This type of stress is primarily due to the confinement of the material and results from the stretching or compression of the material in the circumferential direction. Let's calculate the Hoop stress for the thick-walled pipe using the next formula:

$$\sigma_H = \frac{p \cdot a^2 (r^2 + b^2)}{r^2 (b^2 - a^2)}, \tag{1.35}$$

where σ_H – Hoop Stress, MPa; p – applied radial pressure, MPa; a – inner radius, m; b – outer radius, m; r – radial position where stress is to be found, m.

To calculate the σ_H value, it's necessary to find the pressure p magnitude: considering we have 8 crimping press elements (Titanium Alloy in Ansys) with each element contact area of 5×20 mm and applied normally load of 40 kN (Fig. 1.38, *b*), we will get p = 400 MPa. Other parameters are: r = 9 mm, which means that we seek to determine the stress on the already deformed surface of the pipe under the pressure of these crimping press elements.

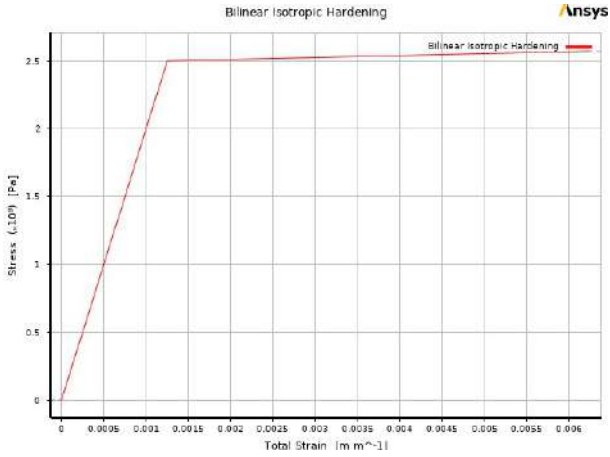

a

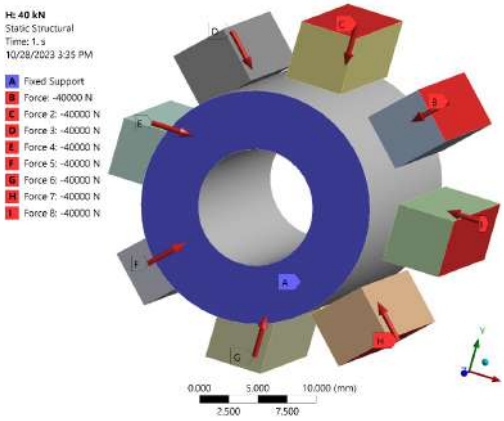

b

Fig. 1.39. Formulation of boundary conditions in Ansys:
***a*) "Bilinear Isotropic Hardening" of Structural Steel NL stress-strain curve;**
***b*) application of fixed support and external loads**

The fact is that the outer radius of the pipe in the places of crimping is subjected to plastic deformation and is reduced by the amount of penetration of the mentioned press elements (by approximately 1 mm), so the outer radius is reduced from 10 mm to 9 mm

approximately. Thus the Hoop stress value according to equation (1.35) is σ_H = 297.9 MPa, that is higher than the Yield stress of Structural Steel NL used in Ansys modelling (250 MPa) and goes beyond the Hook's law. In this a case, it is necessary to take into account the plastic deformation of the pipe in order to establish the total stress:

$$\sigma_{total} = \sigma_H + \sigma_{plastic}, \tag{1.36}$$

where

$$\sigma_{plastic} = E_t \cdot \varepsilon_H, \tag{1.37}$$

where E_t – the tangent modulus that represents the rate at which the stress-strain curve changes at each stress point, *Pa*; ε_H – deformation, m/m. In the context of the Ramberg-Osgood equation (1.38), it's the reciprocal of the first derivative with respect to strain:

$$E_t = \frac{E\sigma_{YS}}{\sigma_{YS} + 0{,}002nE\left(\frac{\sigma}{\sigma_{YS}}\right)^{n-1}}, \tag{1.38}$$

where σ_{YS} – the yield strength, usually the 0.2 % proof stress, MPa; E – the elastic modulus, Pa; n – the strain hardening exponent (or Ramberg-Osgood parameter).

In the context of an idealized elastic-plastic material model, the tangent modulus is employed to characterize the gradient of the stress-strain curve once the material has surpassed its yield point. If the stress-strain graph is a non-linear curve that obeys a simple mathematical law (parabolic or logarithmic etc), then, the tangent modulus is calculated by taking the derivative ($d\sigma/d\varepsilon$) of the stress-strain curve at the specific point of interest beyond the yield point. The Bilinear Isotropic Hardening (Fig. 1.39, *a*) consists of 2 linear regions, so it simplifies our further research.

Based on the E_t = $1{,}45 \cdot 10^9$ Pa applied in the Ansys graph (Fig. 1.39, *a*) with the next intermediate points of the linear plastic hardening region (strain-stress dependence): ε_1 = 0.00125 mm/mm that matches σ_1 = 250 MPa and ε_2 = 0.0045 mm/mm that matches σ_2 = 255 MPa, we find the strain value ε_H = 0.0324 that matches to σ_H = 297.94 MPa using interpolation according to (1.39):

$$\varepsilon_H = \varepsilon_1 + \left(\sigma_H - \sigma_1\right) \cdot \frac{\varepsilon_2 - \varepsilon_1}{\sigma_2 - \sigma_1}. \quad (1.39)$$

Thus, returning to (1.39), we can calculate the value $\sigma_{plastic}$ = 46.98 MPa. Finally, σ_{total} = 297.9 + 46.98 = 344.92 MPa that should be compared with the Ansys FEA results (Fig.1.40a) for the same boundary conditions (Fig. 1.39, *b*): Average Stress value at the end of the experiment (t = 1 s) is 344.52 MPa (Fig. 1.40, *b*), which is less than 1 % error.

As part of our analytical FEA analysis, 3 types of fittings of the same outer diameter (20 mm) with the following wall thickness (t_w, mm) were additionally modeled (Table 1.6): 10 mm (rod), 4 mm (pipe) and 2.5 mm (pipe). Each model underwent 5 types of loads from F = 40 kN to 120 kN, resulting in the following Average Stress values. Besides we have suggested an original parameter *TAC* and TAC/t_w that will be described below.

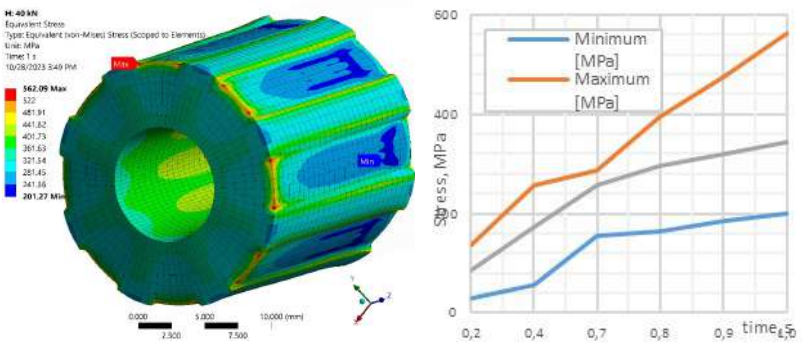

a *b*

Fig. 1.40. Ansys FEA results:
***a*) von Mises stress map (hole diameter is 10 mm; external load is 40 kN);**
***b*) stress graphs (Minimum, Maximum and Average)**

Table 1.6

Stress-loads dependence

t_w, mm	40 kN	60 kN	80 kN	100 kN	120 kN	TAC	TAC/t_w
10	192.09	282.14	339.35	396.65	450.52	3.23	1.615
4	380.07	547.7	718.55	890.84	1063.5	8.54	1.709
2.5	579.37	849.61	1120.8	1392.3	1663.8	13.56	1.694

Returning to the results of Average Stresses in Table 1, it can be seen that they have a close to linear character as the loads on the fitting increase (Fig. 1.41, *a*). This is explained by the linear nature of the graph beyond the Yield point (Fig. 1.39, *a*). A visual view of the stress-strain state of the models under characteristic selected loads is presented in Fig. 1.42. In the meantime, we can move on to a new stage – introduce the following evaluation indicator – TAC (Tangent Angle Coefficient):

$$TAC = \frac{\sigma_{max} - \sigma_{min}}{F_{max} - F_{min}}, \tag{1.40}$$

where $\sigma_{max}, \sigma_{min}$ – maximum and minimum stress during the research (like 450.52 and 192.09 MPa according to FEA); F_{max}, F_{min} – max and min force load (like 120 and 40 kN).

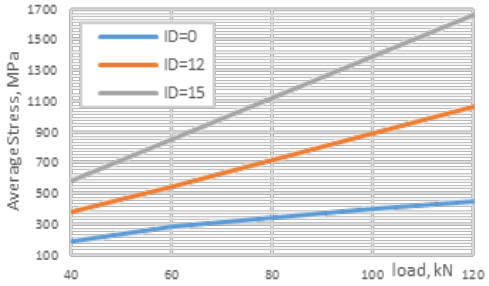

a

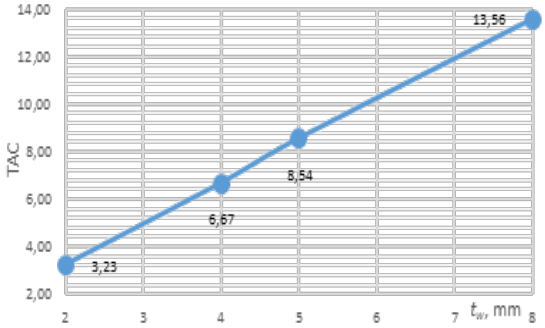

b

Fig. 1.41. Analytical research results:
***a*) Average Stress for 3 types of pipes; *b*) TAC indicator graph**

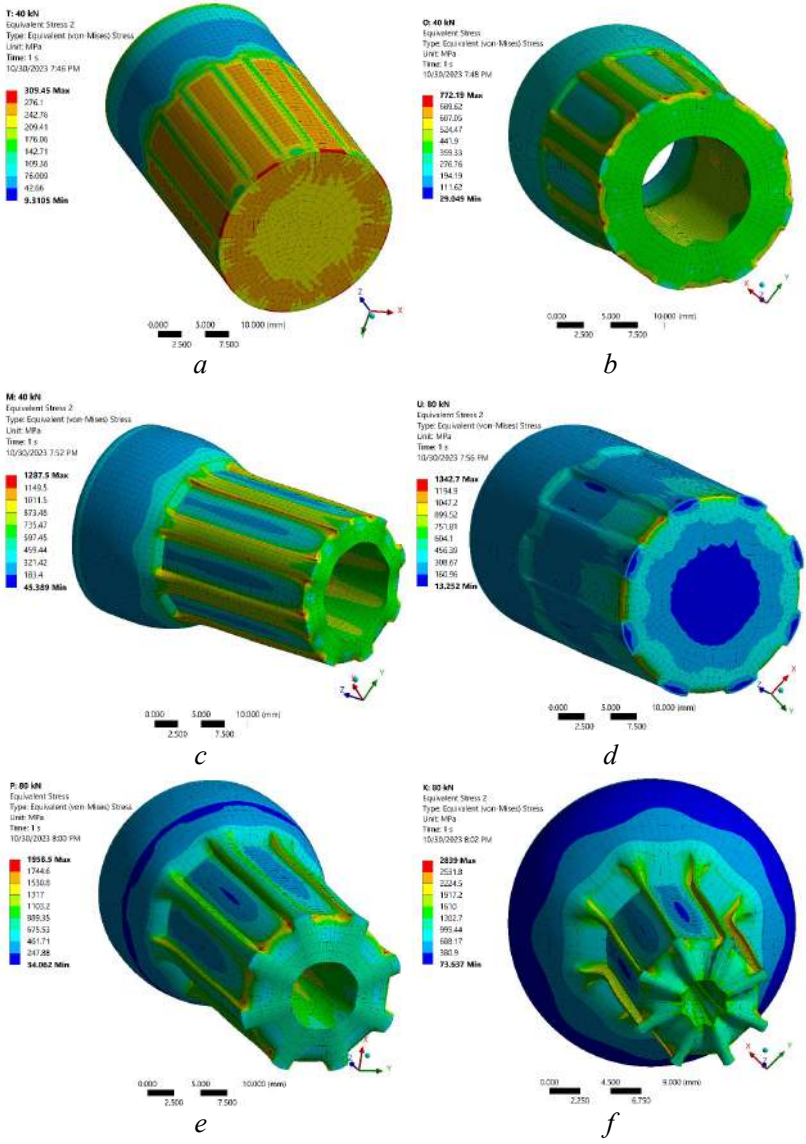

Fig. 1.42. Ansys von Mises stress results:
***a*) t_w = 10 mm, F = 40 kN; *b*) t_w = 4 mm, F = 40 kN; *c*) t_w = 2.5 mm, F = 40 kN;**
***d*) t_w = 10 mm, F = 80 kN; *e*) t_w = 4 mm, F = 80 kN; *f*) t_w = 2.5 mm, F = 80 kN**

The final results of *TAC* are presented on the graph (Fig. 1.41, *b*) – very interesting from a scientific point of view is its linear nature: the dependence of *TAC* on the thickness of the pipe wall (t_w) is linear and this opens up wide prospects for modeling the required configurations of pipes without another FEA recalculation. Let's test our hypothesis of the linearity of the *TAC* indicator: Table 1.6 presents the actual values of the average stresses for all analyzed pipes, except for the fitting with a wall thickness of 5 mm (corresponding to a hole diameter of 10 mm). *TAC* for this pipe with previously measured Average Stress in Ansys (σ_{max} = 851.36 MPa and σ_{min} = 315.56 MPa) according to (1.40) is:

$$TAC = \frac{851,36 - 315,56}{120 - 40} = 6,698. \qquad (1.41)$$

Now let's compare the measured *TAC* (1.41) with the calculated one based on the interpolation method:

$$TAC = 3,23 + (4 - 2)\frac{8,54 - 3,23}{5 - 2} = 6,77. \qquad (1.42)$$

The error is less than 1 % between (1.41) and (1.42). An alternative test criterion for our theory confirmation is a calculation of *TAC* to t_w ratio and here we get quite an exciting results situation: 1.615, 1.694 and 1.709 for the t_w = 10, 4 and 2.5 mm accordingly. The closest of values forces us to judge the effectiveness of the proposed method of stress prediction in the case of Bilinear Isotropic Hardening stress-strain graph of material.

An additional confirmation of the results convergence of the experiment with the calculation is the measurement of the deformations depth of the rod – the real depths measured with a caliper are 0.9–1.0 mm (Fig. 1.38, *b*), and the ones obtained as a result of FEA – 0.96 mm (Fig. 1.43, *a*). At the same time, the maximum values are recorded in the center of the rod and are 2.12 mm – the body bulges under pressure (tag "max" at Fig. 1.43, *a*). The established trend of increasing deformations closer to the longitudinal axis is also observed in the analysis of pipe: under an external load of 120 kN of the fitting with the wall thickness t_w = 4 mm has demonstrated the maximum deformations – 6.33 mm that is observed along the axis (Fig. 1.43, *c*).

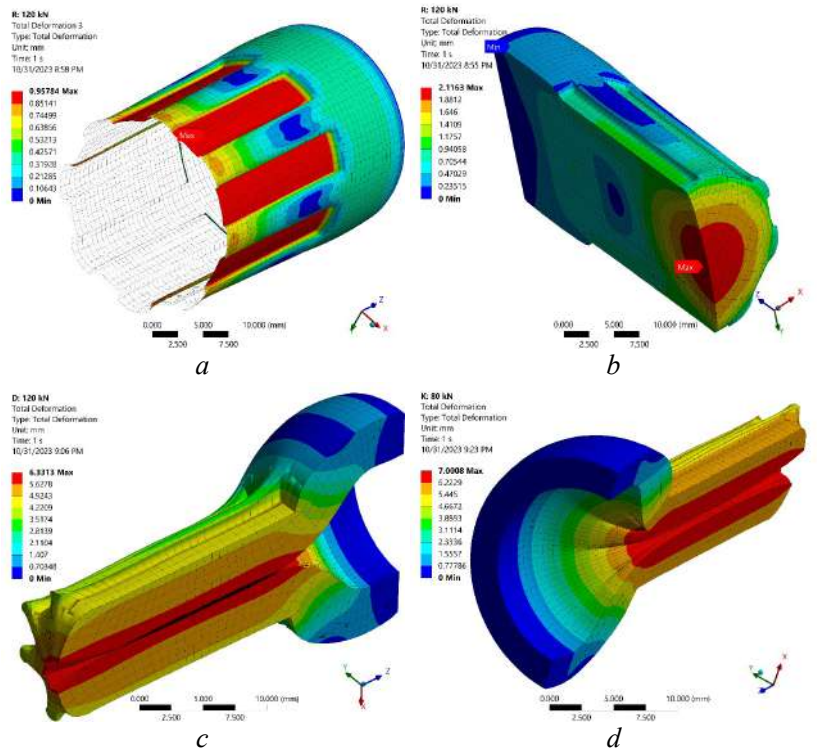

Fig. 1.43. Cable fittigs deformation:
***a*) rod with 120 kN (outer surface); *b*) rod with 120 kN (cross section);**
***c*) pipe (tw = 4 mm) – 120 kN (cross section);**
***d*) pipe (tw = 2.5 mm) – 80 kN (cross section)**

Being less thick (t_w = 2.5 mm), the fitting, despite a significantly lower load (80 kN), gained even higher deformations – 7.0 mm. This well demonstrates the influence of the wall thickness on the ability of the fitting to absorb the load and allows us to pre-calculate the magnitude of the load for crimping the fitting to obtain the required residual diameter of the inner hole. Recall that the last parameter determines the movement freedom of the core inside the conduit of the control cable on the one hand, and the strength of holding the fitting on the same conduit itself – on the other. A competent balance of these two indicators determines the final resource of the remote-control cable.

Conclusions

1. The task of finding the optimal crimping load of the fitting turns out to be quite difficult in the real conditions of the production of remote-control cables: excessive crimping can lead to the destruction of the cable conduit shell or even jamming of the travalling core due to an unacceptable reduction in the inner diameter of the fitting. On the other hand, not pressing the fitting leads to non-fulfillment of the condition of axial strength – the cable must withstand at least 100 kgf.

2. We performed FEA in Ansys with 4 types of fittings of the same outer diameter (20 mm) and different inner diameters (from 0 to 15 mm) in 5 load modes (from 40 to 120 kN). It can be clearly stated that below 40 kN the crimping is insufficient, and above 80 kN causes an unacceptable reduction in the diameter of the fitting hole.

3. One of the key criteria for the formation of fitting plastic deformations is the zone beyond the Yield point of the stress-strain curve with the tangent modulus (in the case of Bilinear Isotropic Hardening used for Structural Steel NL in Ansys its magnitude is 1450 MPa). The specified linearity allows obtaining almost linear stress-load graphs, which prompted the authors to create their own *TAC* evaluation criterion, which is perfectly amenable to interpolation for predicting results without FEA each time. Thus, for a pipe with an internal diameter of 10 mm, the error of the *TAC* value was less than 1 % when comparing the FEA values and the analytical calculation.

1.5. The influence of an additional ring in the structure of an alloy rim on its strength analysis

Analysis and calculation of the strength of car wheel rims is considered in modern research [61–64]. Modern technologies of casting alloy wheels under high pressure from Aluminium alloys (like 6061, 6082, 7075) and Magnesium (like AZ31 and AZ91) make it possible to implement the most daring design solutions – the shapes of rims become more and more complex and new structural elements often appear. This study will analyze the impact of an additional ring implementation in the structure of a multi-spoke alloy rim. This idea is not new and originates from the 80s of the last century – the era of Lancia's dominance in WRC (FIA World Rally Championship) car races with their Delta HF Integrale model. It was on this model and its rally rivals that the strength of rims with an additional ring was practically tested, which after almost 40 years

came back into modern trend, keeping at the same time its main task – increasing the strength and rigidity of the rim. In the era of EVs rapid popularization, the mass of which has increased tremendously (more than 2.5–3 tons in the premium class), the issue of the alloy wheels' strength has become more acute than ever, since the growth of unsprung masses is extremely undesirable.

1.5.1. Rim analyses boundary conditions. Mathematical modelling research

The object of research is the 15" Speedline Evolution magnesium rally racing rim originally produced for Lancia Delta HF Integrale (Fig. 1.44, *a*), which consists of 18 spokes and a concentric ring connecting them together. The ring is located between the hub (4 holes for fastening with bolts) on the outer edge of the rim (closer to it).

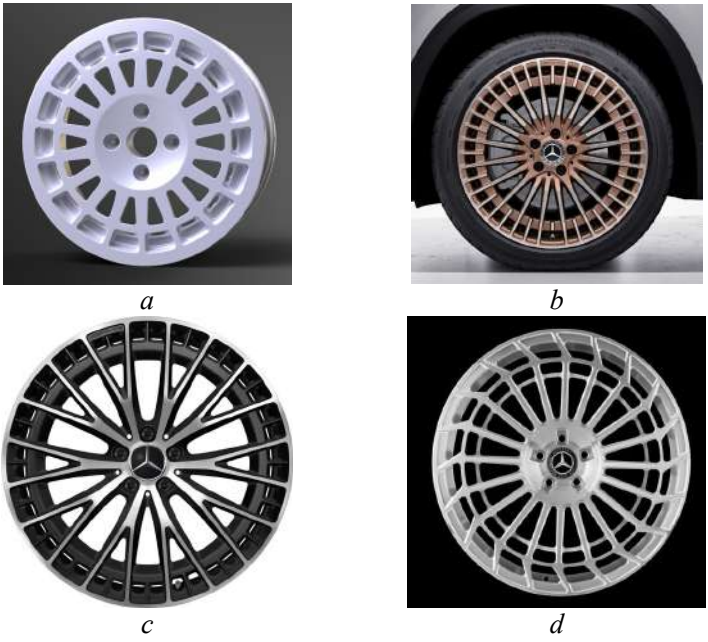

Fig. 1.44. Alloy wheels with the integrated ring:
***a*) solid-model 15" Speedline Evolution for Lancia Delta HF Integrale;**
***b*) AMG 20" for EQB X243; *c*) AMG 21" for EQE43;**
***d*) AVANT GARDE - SRX06 21" for Mercedes-Benz S580 and Evs**

In the version of Fig. 1.44, *d*, the "Avant Garde Wheels" manufacturer went even further and gave 2 rings in the structure of the rim, although their thickness is several times smaller than the concepts b and c in Fig. 1.44.

Let's investigate the mathematical modeling approach which can be particularly effective before complicated and resource-intensive FEA to predict rim strength and mass. The cross-sectional area (A) of the rim without the additional ring can be represented as:

$$A = \pi\left(R_0^2 - R_i^2\right) - N_s \cdot t_s \cdot h_s, \tag{1.43}$$

where R_0 – outer radius of the rim; R_i – inner radius of the rim; N_s – number of spokes; t_s – thickness of the spokes; h_s – height of the spokes (extends from the inner radius to the outer radius).

The cross-sectional area (A_c) of the rim with the additional ring:

$$A_c = \pi\left(R_0^2 - R_i^2\right) - \pi\left(R_c^2 - (R_c - t_c)^2\right) - N_s \cdot t_s \cdot h_s, \tag{1.44}$$

where $\pi\left(R_c^2 - (R_c - t_c)^2\right)$ accounts for the material thickness of the internal circle consider its radius R_c and thickness t_c.

The moment of inertia (I_c) for the rim section needs to account for the presence of the additional ring, therefore, by analogy with the equation for determining the area (1.44), the following should be considered:

$$I_c = \frac{\pi}{4}\left(R_0^4 - R_i^4\right) - \frac{\pi}{4}\left(R_c^4 - (R_c - t_c)^4\right) - N_s \cdot \frac{t_s h_s^3}{12}, \tag{1.45}$$

So, considering the applied load F applied at the outer edge of the rim and the bending moment M_c, the normal and bending stress will be the next:

$$\sigma_r = \frac{F}{A},\ \sigma_{r,c} = \frac{F}{A_c} \text{ and } \sigma_b = \frac{M \cdot y}{l},\ \sigma_{b,c} = \frac{M_c \cdot y}{l_c} = \frac{F(R_0 - R_c)y}{l_c}, \tag{1.46}$$

Thus, the change in strain energy due to the additional ring is:

$$\Delta U = U_c - U = \frac{1}{2E}\left(\int_{V_c}\left(\sigma_{r,c}^2 + \sigma_{b,c}^2\right)dV - \int_V\left(\sigma_r^2 + \sigma_b^2\right)dV\right), \tag{1.47}$$

where V and V_c – volume of the material in the rim (without the additional ring and considering it); E – Young's modulus.

The proposed algorithm of mathematical modeling is an effective method of multi-factor analysis of the selection of optimal geometric parameters of the rim before verification and resource-intensive FEA calculations.

1.5.2. Fea modelling research. Rim analyses results

The following two modifications of the Lancia rally rim were analyzed in the Ansys Static Structural environment: with the additional ring according to the original design (Fig. 1.45, *a*) – model A and the simplified one (without a ring – Fig. 1.45, *b*) – model B. FEA mesh used the next settings: Element Size = 2 mm; Span Angle Center = Fine; Smoothing = High.

a *b*

Fig. 1.45. FEA mesh of the 15-inch Lancia Delta HF Integrale rim: *a*) original design; *b*) without a ring

FEA mesh consists of: 538404 elements (model A) and 468094 (model B). Vertical force F_{wr} (the reaction of the road to the wheels under the influence of the weight of the car m_c) applied to the lower part of the disk (16 surfaces) with the dynamism coefficient k_d (Fig. 1.46):

$$F_{wr} = \frac{m_c q}{4} k_d = \frac{1215 \cdot 9{,}81}{4} \cdot 2{,}5 = 7449{,}5N, \qquad (1.48)$$

Fixed support is applied to 30 surfaces that correspondent to the bolt mounting holes (Fig. 1.46, *a*). Rim material properties: Magnesium Alloy NL with the nonlinear Stress-Strain curve of Bilinear Isotropic Hardening type. The Yield strength = 193 MPa.

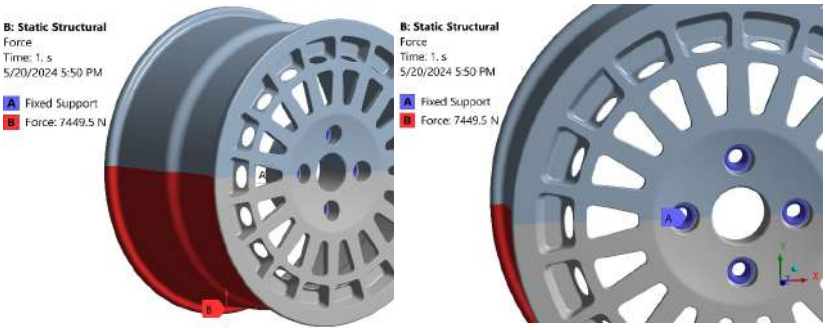

a *b*

Fig. 1.46. Ansys-model boundary conditions:
***a*) applied force F_{wr}; *b*) Fixed Support**

The main criterion for comparing models A and B will be the maximum and average values of von Mises stresses (scale-deformed map in Fig. 1.47). When moving from the original model A to the modified model B, the value of the max Mises stress increased by 6.42 % (from 128.11 MPa to 136.34 MPa – Fig. 1.47, *a*, *b*) but still remain within the Yield strength (193 MPa). Stress extremes fall on the roots of the spokes in the area of the hub – in the corresponding radii of rounding, which is clearly visible from the reverse side of the rims (Fig. 1.47, *c*, *d* and Fig. 1.48).

The average stresses are almost the same in both models: 11.56 MPa (A) and 11.61 MPa (B). This leads to the conclusion that the implementation of an additional ring into the design of the rim increases its uniform strength: with almost unchanged average stresses, the maximum ones are reduced.

Attention should be paid to the lower edge of rim B (closer to the road surface – Fig. 1.47, *a*, *b*) – the stress values from below are twice as high as model A (19–21 vs. 10–12 MPa). This may indicate that in conditions of high loads, beyond the yield point, the probability of cracking or irreversible dents increases dramatically (theoretically by a factor of 2). This area is also very important for rim balancing – often as a result of potholes, the edge loses its geometry (the most delicate area), which is transmitted to the steering wheel and affects the course stability of the car. As expected, the inner edge of the rim received the largest deformations (Fig. 1.49).

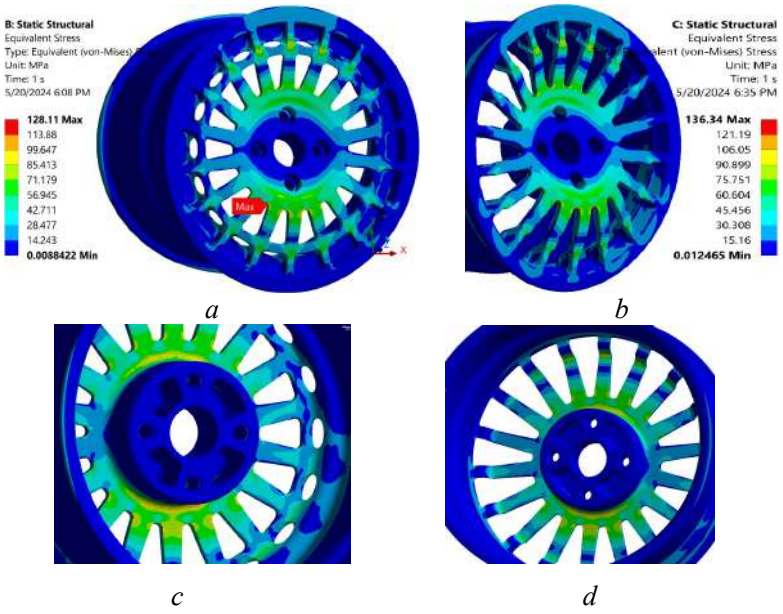

Fig. 1.47. von Mises Stress maps: *a*, *b*) model A and B front view; *c*, *d*) model A and B back view near the hub

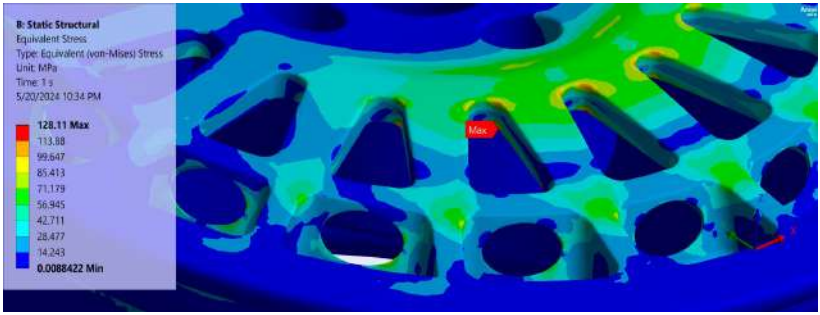

Fig. 1.48. von Mises Stress map of spokes (model A – max value is 128.11 MPa)

Although the inside edge does not have support in the form of spokes, the original design of the rim (with an additional ring) turned out to be more rigid: the maximum deformations are 2.98 mm (model A) vs. 3.27 mm (model B).

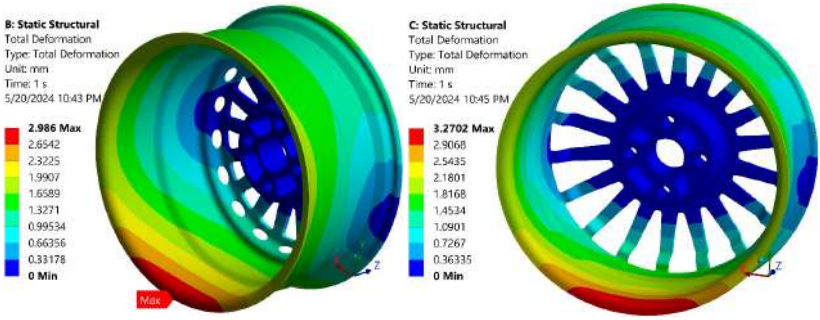

a *b*

Fig. 1.49. Deformation map: *a*) model A; *b*) model B

Conclusions

1. The modern design trend of an additional ring turned out to be a surprisingly successful solution, the roots of which go back to the distant 80s in the world of rally. Maximum stresses of the researched model decreased by 6.42 % (from 128.11 MPa to 136.34 MPa).

2. The inner side of the rim is traditionally the least rigid, but a ring at the opposite side made it possible to reduce the maximum deformations from 3.27 to 2.98 mm (a model without a ring).

3. Obviously, one could talk about a greater 1.7 % mass as a disadvantage, but the concept of a "web" rim design has great prospects: it is not for nothing that smart engineers from Mercedes-Benz use it primarily on super-heavy EVs with a mass of around 3 tons.

References for Chapter 1

1. Kaur, H., Nirmal, U. (2022). A Review on the Development of Wiper System for Automotive Car Windscreen Cleaning Application. Current Journal of Applied Science and Technology, 41 (7), 1–27. https://doi.org/10.9734/cjast/2022/v41i731675

2. Jhung, J., Kim, S. (2021). Behind-The-Scenes (BTS): Wiper-Occlusion Canceling for Advanced Driver Assistance Systems in Adverse Rain Environments. Sensors, 21 (23), 8081. https://doi.org/10.3390/s21238081

3. Graham, B., Knowles, J., Mavros, G. (2023). The influence of contact distribution shaping on the dynamic response of a wiper blade. Proceedings of the Institution of Mechanical Engineers, Part D: Journal of

Automobile Engineering, 095440702311647. https://doi.org/10.1177/095440/70231164792

4. Graham, B., Knowles, J., Mavros, G. (2023). Quantitative Multi-Physics Tools for Automotive Wiper Design. SAE Technical Paper Series. https://doi.org/10.4271/2023-01-0602

5. Antonescu, O., Valeanu, D., Antonescu, D., Strimbeanu, M. (2023). Contributions to the Geometric Synthesis of the Windshield Wiper Mechanism with Rocker-Slider Blade. Mechanisms and Machine Science, 404–413. https://doi.org/10.1007/978-3-031-45709-8_40

6. Sharveswaran, A., Nirmal, U. (2020). Research Development on Wiper Mechanism in Automotive Application: A Critical Review. Current Journal of Applied Science and Technology, 39 (35), 133–161. https://doi.org/10.9734/cjast/2020/v39i3531064

7. Li, Y., Xu, J. (2022). Dynamic characteristics and generation mechanism of windscreen frameless wiper blade oscillations. Nonlinear Dynamics, 111 (4), 3053–3079. https://doi.org/10.1007/s11071-022-08030-0

8. Yang, X., Wang, Y., Guo, H., Yuan, T., Zheng, L., Sun, P. (2022). A theoretical analysis of friction and vibration characteristics of wiper reversal process. Proceedings of the Institution of Mechanical Engineers, Part D: Journal of Automobile Engineering, 237 (6), 1327–1337. https://doi.org/10.1177/09544070221091021

9. Zhao, Z., Yabuno, H., Kamiyama, K. (2022). Dynamic Analysis of a Wiper Blade in Consideration of Attack Angle and Clarification of the Jumping Phenomenon. Applied Sciences, 12 (9), 4112. https://doi.org/10.3390/app12094112

10. Salleh, I., Z. Md Zain, M., R. Abu Bakar, A. (2018). Contact Force and Dynamic Behavior of Automobile Wiper Blade System. International Journal of Engineering & Technology, 7 (3.17), 100. https://doi.org/10.14419/ijet.v7i3.17.16630

11. Roland, A., Wejin, J., Misra, S., Sharma, M. M., Damaševičius, R., Maskeliūnas, R. (2022). A Dynamic Rain Detecting Car Wiper. Lecture Notes in Networks and Systems, 1375–1383. https://doi.org/10.1007/978-3-030-96308-8_127

12. Akanni, J., Ojo, A. O., Abdulwahab, A., Isa, A. A., Ogunbiyi, O. (2022). Development and Implementation of a Prototype Automatic Rain-Sensor Car Wiper System. Journal of Applied Sciences and Environmental Management, 26 (11), 1821–1826. https://doi.org/10.4314/jasem.v26i11.13

13. Yadav, S. (2021). Automatic Rain Sensing Wiper using Arduino. International Journal for Research in Applied Science and Engineering Technology, 9 (VI), 5434–5438. https://doi.org/10.22214/ijraset.2021.36065

14. Chen, T., Hong, Y. (2020). Mathematical Formulae for the Vibration Frequencies of Rubber Wiper on Windshield. arXiv. https://doi.org/10.48550/arXiv.2003.06022

15. Yunpeng, L., Jingjing, X., Xin, W. (2021). Shape analysis and numerical fitting of boneless wiper reed. Journal of Physics: Conference Series, 1939 (1), 012049. https://doi.org/10.1088/1742-6596/1939/1/012049

16. Huang, T. C., Tsai, J. W., Liao, K. C. (2021). Geometry Optimization of a Metallic Flexor for Flat Wipers. International Journal of Automotive Technology, 22 (3), 823–830. https://doi.org/10.1007/s12239-021-0075-6

17. Holenko, K., Voichyshyn, Y., Svidersky, V., Klypko, O. (2023). Simulation of wiper behavior during contact with a curved surface, factors affecting driving safety. Advances in mechanical engineering and transport, 1 (20), 127–137. https://doi.org/10.36910/automash.v1i20.1041

18. Shirsikar, A., Khatik, P., Singh, K., Ram, L. (2022). Optimized Wiper Design using Computational Fluid Dynamics. ARAI Journal of Mobility Technology, 2 (4), 401–410. https://doi.org/10.37285/ajmt.2.4.8

19. Yan, J., Zhu, K., Huang, X., Chen, K. (2022). Design Modification of Vehicle Body Structure for Wiper System Waterproof Performance. Proceedings of China SAE Congress 2021: Selected Papers, 1093–1102. https://doi.org/10.1007/978-981-19-3842-9_85

20. Chen, Z., Gu, Z., Jiang, T. (2019). Research on transient aerodynamic characteristics of windshield wipers of vehicles. International Journal of Numerical Methods for Heat & Fluid Flow, 29 (8), 2870–2884. https://doi.org/10.1108/hff-09-2018-0531

21. Holenko, K., Dykha, O., Koda, E., Kernytskyy, I., Royko, Y., Horbay, O. et al. (2024). Validation of Frontal Crashworthiness Simulation for Low-Entry Type Bus Body According to UNECE R29 Requirements. Applied Sciences, 14 (13), 5595. https://doi.org/10.3390/app14135595

22. Holenko, K., Dykha, O., Koda, E., Kernytskyy, I., Horbay, O., Royko, Y. et al. (2024). Structure and Strength Optimization of the Bogdan ERCV27 Electric Garbage Truck Spatial Frame Under Static Loading. Applied Sciences, 14 (23), 11012. https://doi.org/10.3390/app142311012

23. Holenko, K., Koda, E., Kernytskyy, I., Babak, O., Horbay, O., Popovych, V. et al. (2023). Evaluation of Accelerator Pedal Strength under Critical Loads Using the Finite Element Method. Applied Sciences, 13 (11), 6684. https://doi.org/10.3390/app13116684

24. Kehoe, P., Jafroudi, N., Oubahou, R. A., Toma, E. (2024). Experimental Testing for the Validation of a Multi-body Dynamics Model for a Novel Electric Bus. Advances in Dynamics of Vehicles on Roads and Tracks III, 664–670. https://doi.org/10.1007/978-3-031-66968-2_65

25. Yang, X., Tian, D. (2024). Design Optimization of a Lightweight Electric Bus Body Frame Orienting the Static Performance and Side-Impact Safety. SAE Technical Paper Series. https://doi.org/10.4271/2024-01-2461

26.Wang, D., Xie, C., Liu, Y., Xu, W., Chen, Q. (2020). Multi-objective Collaborative Optimization for the Lightweight Design of an Electric Bus Body Frame. Automotive Innovation, 3 (3), 250–259. https://doi.org/10.1007/s42154-020-00105-1

27. Hong, H. C., Hong, J. Y., D'Apolito, L., Xin, Q. F. (2024). Optimizing Lightweight and Rollover Safety of Bus Superstructure with Multi-Objective Evolutionary Algorithm. International Journal of Automotive Technology, 25 (4), 731–743. https://doi.org/10.1007/s12239-024-00072-0

28. Teng, T.-L., Liang, C.-C., Chu, H.-M. (2022). Development and Analysis of Bus with Composite-Material-Reinforced Frames. International Journal of Automotive Technology, 23 (5), 1229–1237. https://doi.org/10.1007/s12239-022-0108-9

29. Yang, X., Liu, B. (2024). Frontal Crash Oriented Robust Optimization of the Electric Bus Body Frame Considering Tolerance Design. SAE Technical Paper Series. https://doi.org/10.4271/2024-01-2459

30. Jiang, W., Zhang, Y., Liu, J., Zhang, D., Yan, Y., Song, C. (2023). Multi-objective optimization design for steel-aluminum lightweight body of pure electric bus based on RBF model and genetic algorithm. Electronic Research Archive, 31 (4), 1982–1997. https://doi.org/10.3934/era.2023102

31. Fu, C. L., Bai, Y. C., Lin, C., Wang, W. W. (2019). Design optimization of a newly developed aluminum-steel multi-material electric bus body structure. Structural and Multidisciplinary Optimization, 60 (5), 2177–2187. https://doi.org/10.1007/s00158-019-02292-w

32. Gan, J., Zou, L., Yang, X., Liu, J. (2023). Optimization of the Bolted T-Joint of an Electric Bus Body Frame Considering the Fatigue Performance. SAE Technical Paper Series. https://doi.org/10.4271/2023-01-0028

33. Wang, D., Mao, A., Niu, Y., Wei, J., Shi, X. (2017). Lightweight Multi-objective Optimization Design for Body Frame of Pure Electric Large Bus Based on Topology Optimization. China Journal of Highway and Transport, 30 (2), 136–143. https://zgglxb.chd.edu.cn/EN/Y2017/V30/I2/136

34. Fan, D., Yang, X., Song, Y., Zhang, S. (2023). Robust Optimization of an Electric Bus Body Frame Based on the Mesh Morphing Technology. SAE Technical Paper Series. https://doi.org/10.4271/2023-01-0033

35. Schmauder, N., Malzacher, G., Fritsche, M., Burkat, M., König, J., Boese, B. (2024). High potential: lightweight optimised structural design of car bodies for railway vehicles with alternative drive systems.

Discover Mechanical Engineering, 3 (1). https://doi.org/10.1007/s44245-024-00040-z

36. Yang, R., Zhang, W., Li, S., Xu, M., Huang, W., Qin, Z. (2023). Finite Element Analysis and Optimization of Hydrogen Fuel Cell City Bus Body Frame Structure. Applied Sciences, 13 (19), 10964. https://doi.org/10.3390/app131910964

37. Liu, Y., Liu, C., Tan, J., He, Y., Li, F., Zhang, T. (2024). Optimization and Structural Analysis of Automotive Battery Packs Using ANSYS. Symmetry, 16 (11), 1464. https://doi.org/10.3390/sym16111464

38. Liu, F., Xu, Y., Li, M., Guo, J., Han, B. (2022). Optimization of automotive battery pack casing based on equilibrium response surface model and multi-objective particle swarm algorithm. Proceedings of the Institution of Mechanical Engineers, Part D: Journal of Automobile Engineering, 237 (6), 1183–1194. https://doi.org/10.1177/09544070221/104858

39. Wang, K., Shi, P., Zhang, Z. (2023). Finite element modeling of electric vehicle power battery pack and its influence analysis and test research at body-in-white stage. Journal of Vibroengineering, 25 (7), 1353–1368. https://doi.org/10.21595/jve.2023.23260

40. Bijwe, V. B., Mahajan, R., Vaidya, R., Patel, K., Hiwale, D., Walke, A. A. (2024). Simulation Methodology Development for Vibration Test of Bus Body Structure Code AIS-153:2018. SAE Technical Paper Series. https://doi.org/10.4271/2024-26-0249

41. Deepak S. Hugar, U. B. Kadabadi, "Design and Thermal Analysis of Disc Brake for Minimizing Temperature", International Research Journal of Engineering and Technology (IRJET), Volume: 04, Issue: 07, July, 2017

42. Kang, H.; Jung, T.; Hong, Y.; Park, S. Effect of Cross-drilled Hole Shape on Crack of Disc Brake Rotor. J. Korean Soc. Automot. Eng. 2018, 26, 67–76.

43. Lee, H.-H. Finite Element Simulations with ANSYS Workbench 2021: Theory, Applications, Case Studies; SDC Publications: Gunpo-si, Korea, 2021.

44. Jaenudin, J. Jamari, M. Tauviqirrahman, "Thermal Analysis of Disc Brakes using Finite Element Method", American Institute of Physics, 1788, 030028 (2017); doi: 10.1063/1.4968281.

45. Reddy, V.C.; Reddy, M.G.; Gowd, G.H. Modeling and analysis of FSAE car disc brake using FEM. Int. J. Emerg. Technol. Adv. Eng. 2013, 3, 383–389.

46. Santosh Kumar Kallepalli, Harish Musti, DR.K.Sudhakar Reddy, "Enhancement in Design and Thermal Analysis Of Disc Brake Rotor", International Journal Of Engineering Sciences & Research Technology, February, 2017.

47. Mr. Sumeet Satope, Akshaykumar Bote, Swapneel D. Rawool, "Thermal Analysis of Disc Brake", International Journal for Innovative Research in Science & Technology, Volume 3, Issue 12, May 2017.

48. Swapnil Umale,Dheeraj Varma, "Disc Brake Rotor Selection through Finite Element Analysis", International journal of recent trends in engineering & research, Volume 02, Issue 4; April - 2016.

49. Nakatsuji T, Okubo K, Fujii T, Sasada M, Noguchi Y. Study on crack initiation at small holes of one-piece brake discs. SAE, Inc.; 2002. p. 01–0926.

50. Laraqi N. Velocity and relative contact size effect on the thermal constriction resistance in sliding solids. ASME J Heat Transfer 1997;119:173–7.

51. S. Grosu, R.G. Carlos, V. Grosu, B. Vanderborght, D. Lefeber. Evaluation and Analysis of Push-Pull Cable Actuation System Used for Powered Orthoses. Frontiers in Robotics and AI. 5. https://doi.org/10.3389/frobt.2018.00105 (2018)

52. R.G. Carlos, V. Grosu, S. Grosu, A. Leu, D. Ristic-Durrant, B. Vanderborght, D. Lefeber. Torque Control of a Push-Pull Cable Driven Powered Orthosis for the CORBYS Platform. https://doi.org/10.1109/ICORR.2015.7281170 (2015)

53. J. Goodman, T. Beckers, L. Colombo. Geometric Control for Load Transportation With Quadrotor UAVs by Elastic Cables. IEEE Transactions on Control Systems Technology. PP. 1–15. https://doi.org/10.1109/TCST.2023.3296730 (2023)

54. H. Şen, M. Akdağ. Vibration Control of Flexible Manipulators by Active Cable Tension. Scientific Research Communications. 3. 24–31. https://doi.org/10.52460/src.2023.008 (2023)

55. L. Zhongbin, L. Guanghui, L. Fangyu, W. Chuan, T. Yaguang, L. Jufang, Y. Zhongfei, L. Xiaohui, S. Yuntao, Y. Bo. Study on the fastening characteristics of preformed helical fittings considering the surface effect of transmission lines. Scientific Reports. 13. https://doi.org/10.1038/s41598-023-36982-9 (2023)

56. R. Judge, Z. Yang, S.W. Jones, G. Beattie. Full 3D finite element modelling of spiral strand cables. Constr. Build. Mater. https://doi.org/10.1016/j.conbuildmat.2011.12.073 (2012)

57. F. Meng, Y. Chen, D. Minggang, X. Gong. Study on effect of inter-wire contact on mechanical performance of wire rope strand based on semi-analytical method. Int. J. Mech. Sci. 115-116, 416–427. https://doi.org/10.1016/j.ijmecsci.2016.07.012 (2016).

58. D. Wang, D. Zhang, S. Wang, S. Ge. Finite element analysis of hoisting rope and fretting wear evolution and fatigue life estimation of steel

wires. Eng. Fail. Anal. 27(1), 173-193. https://doi.org/10.1016/j.engfailanal./2012.08.014 (2013).

59. R. Adianto, M. Nessim, B. Ngandu. Risk-Based Hoop Stress Factors for Pressure Design. Proceedings of the 2022 14th International Pipeline Conference. Volume 1: Pipeline Safety Management Systems; Project Management, Design, Construction, and Environmental Issues; Strain-Based Design and Assessment; Risk and Reliability; Emerging Fuels and Greenhouse Gas Emissions. Calgary, Alberta, Canada. V001T01A009, ASME (2022)

60. J. Lee. Modified and improved hoop stress formulas. Oceans - Yeosu, Yeosu, Korea (South), 2012, pp. 1–9, https://doi.org/10.1109/OCEANS-Yeosu.2012.6263653 (2012)

61. Korkut T. B., Armakan, E., Ozaydin O., Ozdemir K., & Goren, A., 2020. Design and comparative strength analysis of wheel rims of a lightweight electric vehicle using Al6063 T6 and Al5083 aluminium alloys. Journal of Achievements in Materials and Manufacturing Engineering, 99(2), 57–63.

62. Kandukuri S.Y., Pai, A. & Manikandan, M. 2022, Scope of Carbon Fibre-Reinforced Polymer Wheel Rims for Formula Student Racecars: A Finite Element Analytical approach, J. Inst. Eng. India Ser. C 103, 939–948. https://doi.org/10.1007/s40032-022-00808-w

63. Karikalan Loganathan, S.K. Vijaya Siva Subramani, 2023, Design and optimization of aluminium alloy wheel rim in automobile industry, Materials Today: Proceedings, https://doi.org/10.1016/j.matpr./2023.01.207

64. Poodipeddi S.K.K., Singampalli, A., Rayala L.S.M. and Ravula, S.S.N., 2024, Structural and fatigue analysis of car wheel rims with carbon fibre composites, World Journal of Engineering, Vol. 21 No. 3, pp. 503–509. https://doi.org/10.1108/WJE-04-2022-0178

Chapter 2

Improving the wear resistance of guide elements in transport machinery through contact interaction modeling, surface texturing, and optimization of technological parameters

2.1. Improving the wear resistance of load-bearing guide elements in transport machinery: tribological analysis, surface texture and lubricants

Guideways are one of the key components of mechanical systems that ensure the accuracy and stability of movement in various technical devices. They are widely used in industrial machines, lathes, conveyor systems, and other high-precision mechanisms. One of the main issues that arises during the operation of guideways is wear, which largely depends on the friction between the contact surfaces. As a result of prolonged use, guideways can experience significant deformation, reducing their efficiency and requiring frequent maintenance or replacement.

One of the key factors affecting wear is the surface texture of the contacting elements, as well as the choice of lubricating materials. Inadequate surface roughness parameters and improper lubricant selection can increase the friction coefficient, which, in turn, accelerates wear. However, optimizing the surface texture and using specialized lubricating materials can significantly reduce this effect. Therefore, one of the priority areas of research is the analysis of the impact of various factors on the tribological characteristics of guideways, which allows the development of new methods for improving their wear resistance.

In particular, studies have shown that using composite lubricants containing molybdenum disulfide, hexagonal boron nitride, and other promising additives can significantly improve friction and wear resistance of guideways. At the same time, optimizing the geometry of the contact surfaces and controlling the lubrication process are necessary to achieve maximum efficiency of mechanical systems.

Thus, the problem of wear resistance of guideways and optimizing their characteristics is relevant and requires further scientific development,

which will contribute to increasing their lifespan and improving the reliability of mechanical systems.

The most common failure modes of the guide are wear and contact fatigue, which are significantly affected by the friction properties of the contact surfaces. In the paper [1], the parameters of the three-dimensional rough surface are investigated for the evaluation of the guide. First, an effective three-dimensional surface model is achieved using the wavelet transform method and reverse engineering software. Second, the influence of the parameters of the functional surface on the friction force, average pressure and friction coefficient is studied using the computational fluid dynamics modeling method, and a regression model is built to predict the friction force. Third, the combinations of optimal surface parameters are analyzed considering the friction index and the simulation results are compared. The results show good agreement between the experimental results and the simulation. This study provides theoretical guidance for the fabrication of the guide.

Roller linear guide is a type of precision linear motion component that is widely used [2]. Stiffness and wear directly affect the performance and service life of roller linear guides. Therefore, the study of stiffness and wear is important for optimizing the design and improving the performance of roller linear guides. The study analyzes the contact mechanics between the roller and the raceway and the deformation of the roller. Using Archard's wear theory, the wear process of roller linear guides is analyzed. A calculation model of the slider movement, which is related to the wear loss of the slider's raceway during its reciprocating motion under load, is developed to predict the wear of roller linear guides. The effectiveness of the proposed models in predicting the contact stiffness and wear is verified through simulation and experiments on a specialized test system.

Guides adapt to the movement of tools or workpieces, and their dynamic behavior and associated sliding effects have a great influence on accuracy, stability, and productivity [3]. During machining, guides are subjected to oscillatory excitations due to cutting forces, which requires consideration of their pre-slip behavior along with the sliding characteristics to compensate for the associated tracking errors by the position control system. The study [3] considers the friction effects in the pre-slip and sliding modes of lubricated linear roller guide systems to provide an accurate dynamic model of the machine tool element. To simulate the dynamic characteristics of the frictional contact in a lubricated linear roller guide, which is commonly used in the machine

tool positioning control system to estimate the compensating driving force, a modified approach is used to consider the contact physics of rollers and tracks and the dynamics of the lubricating film. The proposed model also includes the effects of the coupling between normal and tangential forces in the contact (Fig. 2.1) [3].

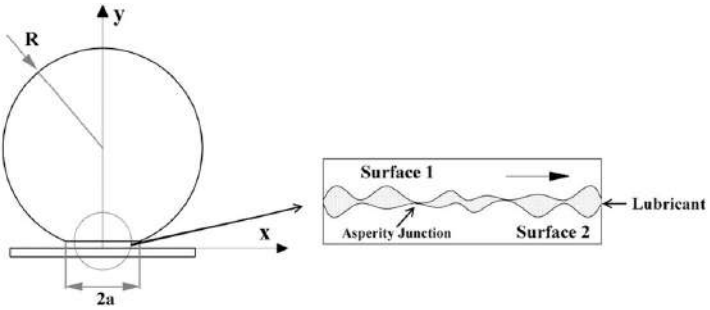

Fig. 2.1. Schematic representation of an elastohydrodynamic lubricating contact in a mixed lubrication mode

Experimental studies were conducted on a lubricated linear roller guideway to verify the performance of the proposed modified model. The experimental observations illustrate the dynamic behavior of friction in a lubricated linear guideway. Comparison of experimentally measured data and the proposed modified samples shows that the model can accurately predict the dynamic behavior of the frictional contact. To optimize the sliding phenomenon under low speed and high load conditions, a composite lubrication structure is used [4]. The optimal response surface design method establishes a quadratic mathematical model for the multi-stage parameters of the composite lubrication structure, including creep time and average friction coefficient. The optimal combined parameters of the multi-stage composite lubrication structures are determined. The optimal ratio of lubricant to molybdenum disulfide was identified, and a composite lubrication structure was proposed to improve the sliding phenomenon and friction efficiency of sliding guide rails under medium speed and medium load conditions. The results of these studies show that when low speed and high load are present, the creep time and friction coefficient first decrease and then increase as the width, distance, and cycle length of the sinusoidal texture and the diameter of the hexagonal pit expand. Under the circumstances of medium load and speed, the multi-stage composite lubrication structures

exhibit superior friction performance. These data can guide the design of multi-stage composite lubrication structures on the surface of slideways.

In order to improve the sliding of guides [5], the design of a composite lubricating structure on the surfaces of sliding guides and the characteristics of the friction force were investigated step by step. The composite lubricating microtexture was prepared by the high temperature and high pressure mosaic method based on the laser ablation microtexture. The general scheme of the formation of structured surfaces by laser is shown in Fig. 2.2 [4].

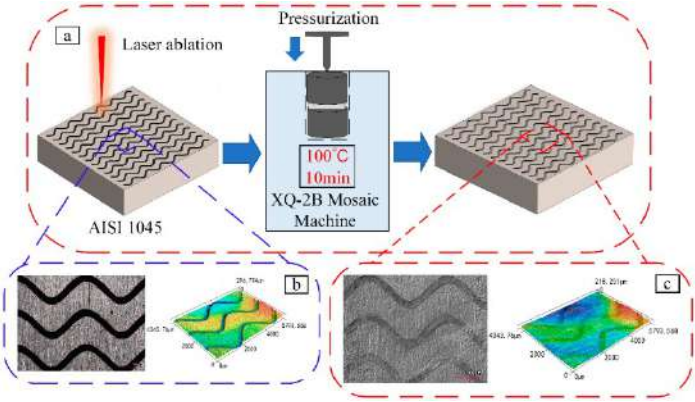

Fig. 2.2. Schematic diagram of specimen preparation:
***a*) Laser ablation diagram; *b*) Micro-texture before filling;**
***c*) Micro-texture after filling**

The friction force characterization methods were proposed step by step by friction tests. The effects of different composite lubricant structures on the friction characteristic parameters of each stage were investigated. Theoretical models of composite lubricant structures for improving the creep phenomenon were established, and composite lubricant structures with the best characteristics for reducing the influence of the creep phenomenon were found. The results show that the surface microtexture only affects the sliding and rising stages of the friction force, while the composite lubricant texture has a significant effect on the entire starting stage. The multi-stage composite lubricant texture with a combination of sinusoidal grooves and hexagonal pits filled with molybdenum disulfide was the most effective in improving the surface contact conditions and suppressing the creep phenomenon (Fig. 2.3).

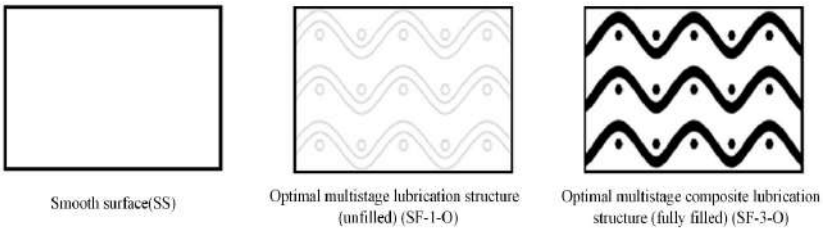

Fig. 2.3. Diagram of different grease textures

To study the effect of different surface treatment methods on the antifriction performance of Babbitt-Steel 45 alloy pair, hexagonal boron nitride was encapsulated in the surface texture, and composite lubricating structure surfaces were prepared [6]. The disc wear test was carried out with lubricant, and the wear process was separated by quantitative analysis. The antifriction performance of composite lubricating structure surfaces during running-in and normal wear was investigated. The results show that the composite lubricating structure surfaces have a lower friction coefficient and that the antifriction performance is better than that of the texture surface alone. Compared with the surface without texture, the average friction coefficient of the composite lubricating structure surfaces decreases by 77 % during the running-in period and 68 % during the normal wear period. Composite lubricating structure surfaces with larger texture pore diameter have better antifriction performance and shorter running-in period. Both textured surfaces and composite surfaces of the lubricating structure have more significant anti-friction characteristics at higher speeds. It has been found that the lower the friction coefficient of different surfaces during the break-in period, the lower the corresponding friction coefficient after entering the normal wear period. Reducing sliding wear and friction in guide bearings can bring both economic and environmental benefits, including longer service life, lower operating costs, and higher efficiency. In a study [7], the effect of stainless steel countersurface roughness on the tribological behavior of three bearing materials used in hydropower was evaluated using linear reciprocating motion at high contact pressure and low sliding speed. Surface roughness was measured using white light interferometry. The results of this study show that surfaces that are too smooth lead to greater friction and wear of the countersurface, while rougher surfaces negatively affect polymer wear (Fig. 2.4) [7].

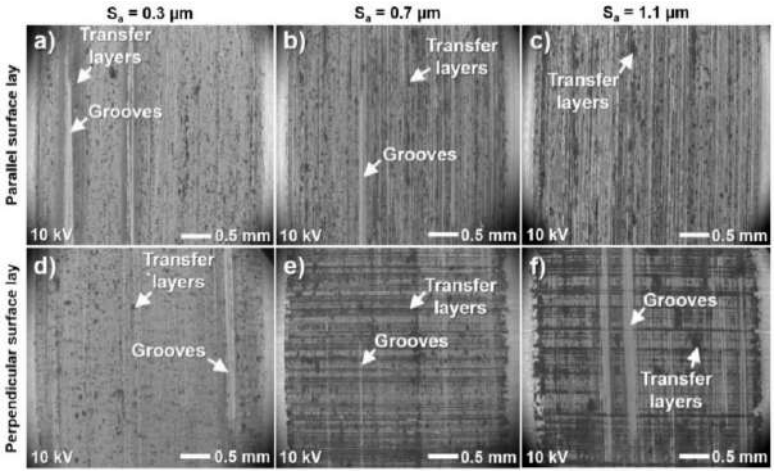

Fig. 2.4. SEM micrographs of transfer layers formed on polished stainless steel closer to the center of the wear track after sliding on fiber-reinforced thermoset

The best surface coverage by protective transfer layers is found on steel surfaces with perpendicular stacking and is accompanied by a lower coefficient of friction compared to parallel stacking. The dominant wear mechanism of the bearing materials changes from delamination wear to abrasive wear between the lowest and intermediate roughness of the steel surfaces with parallel stacking. It is concluded that the relief of the opposing surface has a significant effect on the tribological behavior of these bearing materials and that the effect differs between self-lubricating polymer composites. In [8–9], an experimentally validated numerical approach to the evaluation of linear guideway wear is presented, taking into account the associated vertical and horizontal movements and taking into account the lubrication starvation. The results show that the lubrication starvation has a pronounced effect on the thickness of the lubricating film, friction and the applied load at contact up to 30 %. The localized pressure values can vary. The course of the starvation effect depends on the frequency. It was also found that the starvation effect can be controlled by the magnitude of the preload on the linear guide. Based on the theory of point contact elastohydrodynamic lubrication, a model of free vibration of a contact pair is presented for qualitative analysis of the influence of vibration on film characteristics [10].

Models of film stiffness and damping coefficient under elastohydrodynamic lubrication are constructed to study the influence of operating conditions on dynamic parameters. Complete numerical solutions are obtained using multi-grid techniques. It is found that there is damping from the decay of pressure fluctuations and film thickness in a lubricated ball linear guide. In addition, high load or low speed operating conditions can lead to an increase in film stiffness at the steel ball-guide contact, but there is a tendency for the film damping coefficient to vary inversely. The study [11] studies the contact stiffness of linear rolling guides due to the effects of friction and wear during operation. The initial and final contact stiffness models were established. As a confirmation of the predicted variable stiffness, an experimental modal analysis was performed on a specialized linear guide system. The results show that the contact stiffness of linear guides decreases with the increase of the friction path, and the entire stiffness decline can be divided into two different stages depending on how the thermal effect and wear effect affect the contact deformations of the balls at different rolling distances.

The aim of [12] is to establish a simplified model of a closed hydrostatic guideway for rapid analysis of static and dynamic characteristics. In addition, the effects of compressibility and dynamic frequency are taken into account in the new dynamic model. The new model is based on the second type of Lagrange equation. In this model, a closed hydrostatic guideway is supported by 10 gaskets, and each oil gasket is equivalent to a nonlinear spring-damper system. The equivalent spring coefficient and the damper coefficient of the oil gasket are considered by three different equivalent methods. Verification experiments of the step load response and dynamic stiffness are carried out on the hydrostatic guideway.

Most studies on linear rolling bearings usually assume that the contact load between the ball and the raceway is uniform, which leads to deviations from the actual conditions. The study [13] aims to establish a load distribution model based on the Hertzian contact theory with combined ball obstacles that are transformed from the preload, the center distance error of the ball raceway. The reliability of the proposed model is verified by numerical methods for load distribution and deformation analysis. The result shows that the proposed approach is in better agreement with the experimental results compared with the preload effect alone. This work can be an important starting point for studying the friction and wear of equipment guide elements.

Hydrostatic guides have been used as an important element of precision engineering in numerous applications requiring high-precision motion and positioning with significant load capacity. Hydrostatic guides provide good operational performance, especially in terms of high rigidity and damping characteristics, but also its high load capacity combined with excellent motion accuracy. However, a comprehensive review of hydrostatic guides has not been reported so far. The paper [14] aimed to present an informative literature review of research and engineering developments on hydrostatic guides, describing their basic operating principles and applications in precision machines, defining and characterizing hydrostatic guide concepts, briefly reviewing motion error modeling and compensation types, discussing the impact characteristics, and further discussing emerging issues of sliding guides and their engineering applications.

In [15], in order to expand the production of machine tools that use precision-machined slideways, cubic boron nitride was implemented as an alternative machining process to conventional surface grinding. While higher material removal rates can be achieved with a milling strategy, the use of a defined cutting edge results in surfaces with irregularities. These sharp peaks wear quickly during sliding contact, leading to unacceptable changes in the bearing surface of the guide. This paper investigates the use of a spindle-mounted abrasive disk tool to fabricate a functional surface. The optimal process parameters were investigated using 2D profile measurements and then compared using an analysis of ground, milled and polished surfaces. Polishing was found to reduce both the height and volume of irregularities on the milled surface, resulting in contact characteristics that were more similar to those of conventional surfaces currently used for slideways.

For economic, environmental and even technical reasons, there has been a trend for several years towards the introduction of self-lubricating materials for cylindrical slideways. This makes it possible to eliminate external lubricants, simplify the design and reduce maintenance costs. Among self-lubricating materials, the so-called engineering plastics are of increasing importance. Unfortunately, data on their friction and wear characteristics are very different, and there is often a lack of a common understanding of the physical mechanism of their action. In the article [16], some types of oil-filled engineering plastics are experimentally investigated using small-scale reciprocating tribotesting. The dependences for the coefficient of friction for such types of materials are shown in Fig. 2.5 [16].

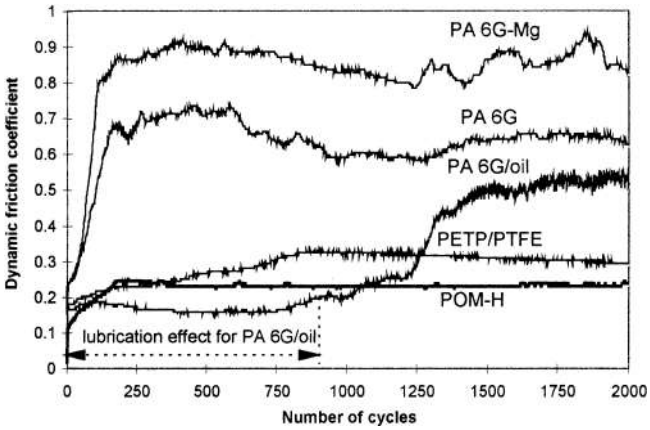

Fig. 5. Dynamic friction characteristic of polymers against smooth steel surface

Tribological behavior is explained in relation to the chemical and mechanical properties of materials. The main failure processes are described for light wear conditions as well as for overload conditions.

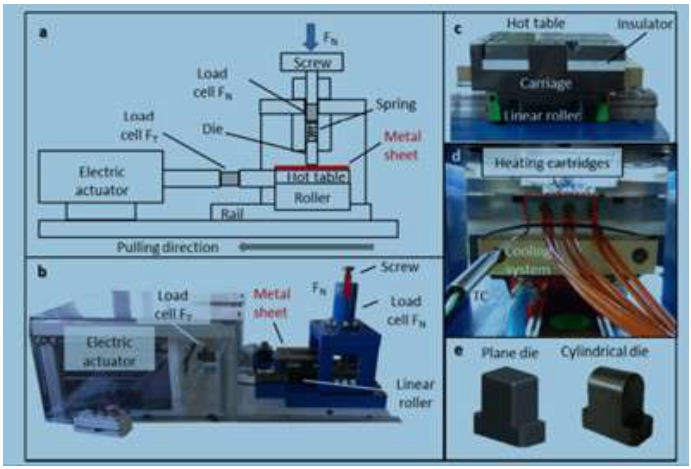

Fig. 2.6. Schematic representation of flat strip drawing test (*a*) and the real version (*b*); details of the linear roller guideway (*c*); details of the hot table heating system, thermocouple to control temperature and the cooling system (*d*); *e*) plane and cylindrical die shape usable in the machine

In the article [17] a new experimental apparatus is presented, suitable for wear tests of reciprocating guides at elevated temperatures (Fig. 2.6) [17].

It consists of a linear slide rail connected to an electric drive and equipped with a heating plate for heating the metal sheets. The solid frame incorporates a screw device used to apply the normal load. Thermocouples placed on both the plate and the sheet sample are used to monitor the temperature during the test. The machine is also equipped with two strain gauges to record the normal and tangential loads. High-strength steel was chosen as the reference material for testing the machine. The results showed the operational capability of the new equipment and good stability of the mechanical and thermal state during the tests.

In recent years, sliding guides have been re-examined as linear motion guides for machine tools due to the demand for machines with good dynamic characteristics, which is vital in machining difficult-to-machine materials. While the traditional approach to manufacturing the sliding surface is grinding. In [18–20], an alternative manufacturing approach based on cubic boron nitride using Al and Mg additives in the cast iron material for better machinability of sliding guides was investigated. The machining results showed a significant improvement in machinability, especially in terms of tool wear under certain cutting conditions using cleaned hardened cast iron and cubonite tools. During experimental analysis, it was found that oxide films of the additives were created on the cutting edge of the tool to protect the tool from wear. By reducing tool wear, a stable surface roughness can also be achieved. The case study also demonstrated the effectiveness of a manufacturing approach based on milling slideways with cleaned cast iron and found high-speed cutting conditions.

The characteristics between the rolling balls and the raceways are key to studying the linear rolling guide. In [21–22], the contact stresses with non-standard sized balls, which include the change of contact angle, are given by the established joint model (Fig. 2.7) [22].

In addition, the influence of the location, number and degree of deviation of non-dimensional balls on the stress distribution is studied. The contact stress distribution between the ball and the raceway is analyzed for different location cases. The effectiveness of the contact stiffness and wear prediction model is verified by simulation and analysis.

In articles [23–24], favorable microdimples from the calculated results were fabricated on a guide using single-pulse process intervals with a specialized accuracy compensation method (Fig. 2.8) [24].

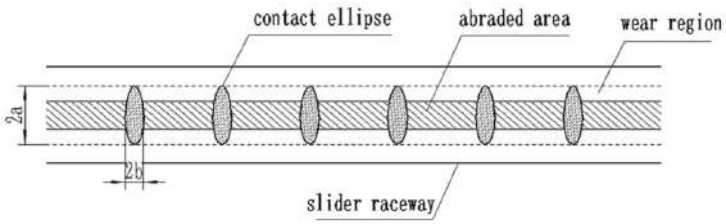

Fig. 2.7. Contact mechanism between the balls and the carriage raceway

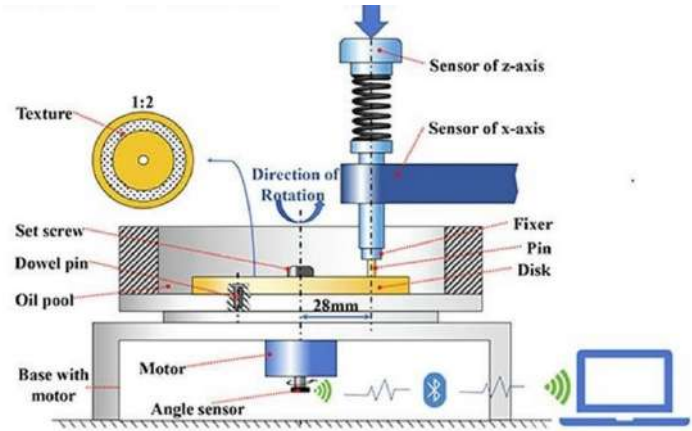

Fig. 2.8. Experimental setup for the formation and study of surface microprofiles

Contrast tests were conducted to verify the anti-slip performance. The results showed that the favorable micro-dimple depth size could be 1–5 μm, and the area ratio was 11 % ~ 16 %. The friction coefficient was reduced by 15 %.

At present, the wear models and the prediction of the accuracy of the guide are established based on the elastoplastic mechanics of continuum media. These methods are limited to describing the process of accuracy reduction using the material characteristics determined based on the conditions of the macroscopic hypothesis. In [25–26], a multi-scale method based on the principle of a quasi-continuous medium is proposed to describe the degradation process of the linear accuracy of the guide using an exponential model. According to the distribution of the wear of the guide surface with the process of micromorphology

evolution, the measurement value of the linear accuracy of the guide is systematically modeled. Using the quasi-continuous medium method instead of the continuum hypothesis, an exponential model of the guide wear is established. The exponential wear model uses a wear index to describe the wear state based on the measurement of linear accuracy, rather than long-term wear products. Information about the microtopography of the guide surface is obtained. Thus, the wear condition of the guide is checked under different loading conditions, and the validity of using the method to establish an exponential guide wear model is also verified.

Solid lubricants have been widely used in many fields. In [27–28], the influence of each component in composite solid lubricants on the tribological characteristics is investigated and the antifriction effect of different types of solid lubricants is compared to solve the problem of lubrication of cylindrical sliding guides (Fig. 2.9) [28]. Surface textures with pits were produced on the surfaces of bearing steel by solid-state laser. Composite solid lubricants filled the micropits with heat- and pressure-supported deposition products consisting of lubricating elements. The tribological characteristics of sliding friction for different types of lubricants with different grain sizes were evaluated using a ring-on-disk tribometer.

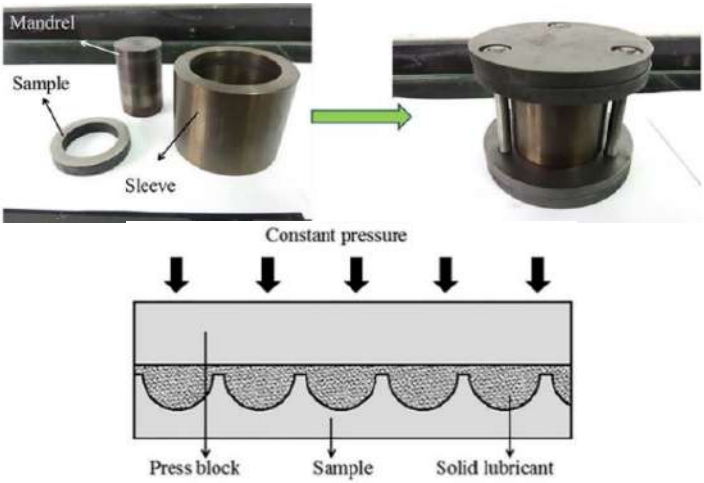

Fig. 2.9. Experimental tests of solid lubricants for contact strength

On this basis, an orthogonal experiment with four factors and three levels was designed to investigate the effects of different components

of solid lubricants on tribological characteristics. Solid lubricants with nanoparticles can improve the antifriction ability: the friction coefficient is higher than that of micron graphite, and the friction coefficient of nano-sized molybdenum disulfide is reduced compared with that of micron-sized molybdenum disulfide. According to the experimental results, the optimal formula of composite solid lubricants was graphite nanotubes: molybdenum disulfide: polyamide: carbon.

The improvement of tribological properties by applying different textured surfaces has been reported by many researchers. In these studies, most of the surfaces used were textured by lasers. However, this texturing method has several problems, including thermal effects, accumulation formation, possible pit shapes, and lower efficiency than mechanical methods. Traditional mechanical texturing methods also have some problems. In the study [29–30], an alternative method was developed using vibrocutting using a diamond indenter that vibrates in the depth direction with an amplitude of tens of microns. The asperities formed around all the pits during texturing can be removed by additionally performing conventional microcutting. Dry sliding tests were performed using steel balls on surfaces textured by both the proposed and conventional cutting methods for comparison. A series of sliding test results were analyzed using the coefficient of friction and observations of worn surfaces. As a result, the textured surface obtained with a relatively high areal density (40 %) where the inclusions were completely removed showed the lowest coefficient of friction and wear. Thus, the proposed texturing method can be recommended for creating surface textures for better tribological properties.

Conclusions

1. Wear and contact fatigue are the main factors of guideway degradation, which largely depend on the friction between the contact surfaces. Optimization of roughness and tribological parameters can improve their durability.

2. Optimization of lubricating structures (using molybdenum disulfide, hexagonal boron nitride, etc.) allows to significantly reduce the coefficient of friction and improve antifriction properties, especially during running-in and normal wear.

3. The dynamic characteristics of the guideways play a key role in the accuracy and stability of the operation. The stiffness of the contact pair decreases with the increase of the friction path, and the temperature and wear affect the contact deformation.

4. Wear prediction methods based on the Archard and Hertz theories allow for optimizing load distribution between balls and raceways, which helps to increase the accuracy of friction and wear prediction.

5. New materials, such as cubic boron nitride, as well as hydrostatic guides, provide high rigidity, damping, and motion accuracy, but require further research for implementation in practical applications.

2.2. Investigation of the stress contact state during surface plastic treatment of a cylindrical sliding guide

The method of discrete strengthening of steel parts of the "shaft" type requires the need to assess the depth of the strengthened wear-resistant layer. A reinforced layer is a layer characterized by the formation of a so-called white layer. This layer is formed in the volumes of the material, the heating temperature of which exceeds the phase transformation temperature. A high-temperature volume can be defined as a volume in which the temperature is above 600 °C.

Experimental studies show that the width and height of the high-temperature volume in working hardening modes are close to the width and height of the contact of the tool with the part. Therefore, determining the contact surface of the tool and the processed part is one of the first steps necessary for the correct selection of technological parameters.

In addition, knowledge of the geometric parameters of the contact surface is required to determine other characteristics of the technological process, in particular, the current density, which ensures the necessary temperature on the surface of the contact zone. The purpose of the task is to create a calculation method for assessing the influence of the load of the run-in roller on the resulting stresses and deformations of the shaft when simulating their mutual rotation in the environment of the finite element method (Ansys Static Structural).

2.2.1. Analysis of methods for surface plastic treatment of cylindrical guide elements

It is advisable to familiarize yourself with various methods of surface treatment since all of them are related to plastic deformation of the upper layers and their hardening. The paper [31] introduces a multiphysic model to explore the hardening mechanism of stainless steel 304's surface layer, revealing that hardening significantly strengthens the surface. The study [32] explores a new surface treatment combining

discrete laser surface hardening (DLSH) and ultrasonic surface rolling (USR) on 25CrNi$_2$MoV steel with residual stresses up to 1240 ± 91 MPa. In [33] experimental tests were carried out during electromechanical strengthening to analyze the influence of the stress-strain state on wear resistance. The authors in [34] explore how deep rolling influences the formation of a white etching layer (WEL) on AISI 4140 steel with varied microstructures from different heat treatments. The paper [35] compares various surface modification processes through analysis of their effects on strengthening. Modern technologies are used to strengthen the surfaces of the shafts. In [36] considers the strengthening process using laser surfacing, which is the basis for applying a Ti/B_4C/dr40 composite coating to strengthen the surface of shaft parts. In paper [37] the shaft parts surface was treated by ultrasonic surface machining (USM) technology after surface induction hardening and tempering. In the article [38], the laser surfacing technology is used to strengthen the surface of the machine shaft and the analysis of the microstructure, hardness, friction and wear resistance after laser surfacing is carried out. In order to improve the surface tribological properties of TC4 titanium alloy, laser processing technology was used in [39] to obtain a cellular texture on the surface of TC_4. Discrete surface textures of grooves with different orientation and distance between them were obtained on Ti–6Al–4V alloy using a laser in the study [40]. In [41] authors explore the enhancement of surface properties of 2205 duplex stainless steel through high current pulsed electron beam (HCPEB) treatments, observing microhardness and corrosion resistance. The paper [42] introduces a modified Newton-Raphson method that is also used in the current research. The formation of white layers [43–47] is crucial for their impact on mechanical properties and the industry's need for predictive models. Considering the usage of Ansys Coupled Field which allows simulating mechanical and thermal loads at the same time, it is advisable to refer to the works [48–50].

2.2.2. Development of a finite element model of the contact interaction between the roller and the cylindrical guide

The complexity of the experiment lies in the curvilinearity of the forms in contact: the cylinder, represented by the shaft, and the torus, which corresponds to the pressure roller. The geometric parameters of the model elements are as follows: a roller with a diameter of 56 mm and a radius of the working surface of 2.5 mm; shaft with a diameter of

25 mm. The experiment presented in the current task is aimed at evaluating the influence of material nonlinearity on the results of stresses and strains. The current model simplified in terms of its components was adopted (truncated torus of the roller (segment) and a short segment of the shaft (Fig. 2.10).

The task required high computational resources, the total calculation time was 1 hour. 42 min. The roller presses in a straight line (along the Y axis) on the surface of the shaft, having only one degree of freedom. The MKE grid consists of 70,661 elements connected by 115,564 nodes, and the shape of the final elements is mainly Tetrahedrons (Fig. 2.11).

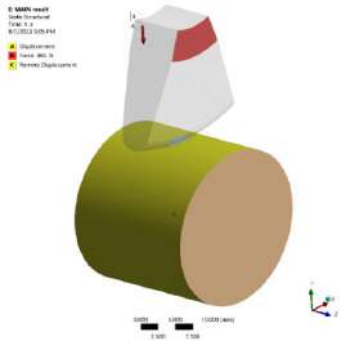

Fig. 2.10. Model of a truncated segment of a roller-shaft, load 400 N

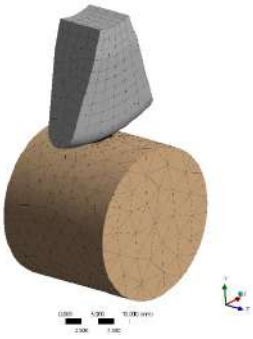

Fig. 2.11. Mesh of FEM elements

At the point of contact, the body of the stain itself (area 4.2×1.8 mm and depth 0.3 mm) is modeled separately (Fig. 2.11). The size of the final elements here does not exceed 0.05 mm.

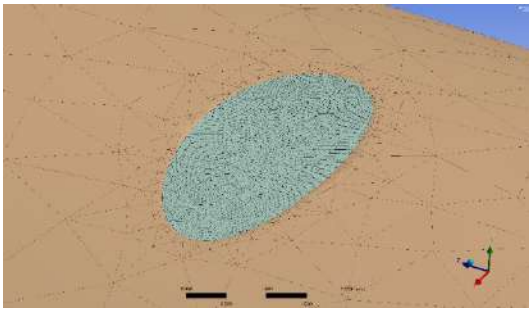

Fig. 2.12. Spot contact

Contact Sizing and Contact Match functionality of Ansys with the Tolerance indicator of 0.05 mm and 0.04 mm, respectively, was used to connect the nodes of the shaft model and the spot body.

2.2.3. Analysis of the distribution of contact and thermal stresses in the contact zone

Nonlinear properties of the Structural Steel material: beyond the yield point, the stress-strain graph abruptly changes its character: instead of being proportionally linear, it acquires a fracture (Bilinear Isotropic Hardering). In fact, this means that beyond the yield point, with the next slight increase in loads (and as a result, stresses), deformations (mm/mm) increase significantly – irreversible inertial plastic processes occur (the body "floats").

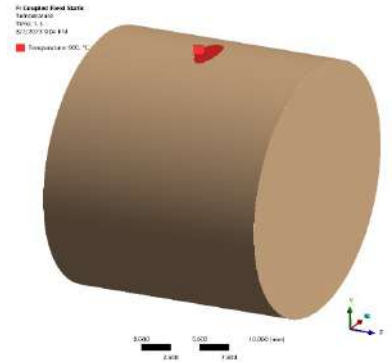

Fig. 2.13. Thermal load – 900 °C

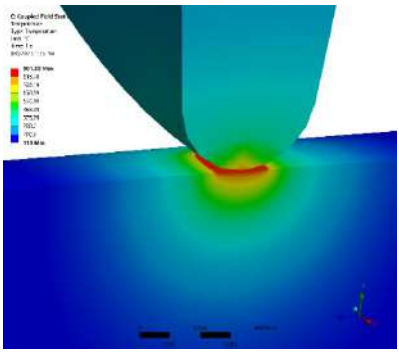

Fig. 2.14. Temperature distribution in the contact zone

In addition, the above-mentioned effect of plasticity is enhanced by the influence of temperatures – a thermal load (900 °C). Convection of the medium is 25 W/m^2 °C at a temperature of 22 °C.

Boundary conditions also include force F_p = 400 N, directed opposite to the Y axis and applied to the sides of the roller. The reason is the heat load, the graph of the temperature distribution along the cross-section of the model is shown in Fig. 2.14.

The time of the experiment is 4.0 s, and the load application schedule is stepwise (Fig. 2.15): during the period of 0.0–1.0 s, the load increases F_p from 0 N to 400 N; the interval of 1.0–2.0 s has a

stabilization character F_p keeps the value of 400 N; during the next second (2.0–3.0 s), the load F_p is reduced to 0 N; the last interval (3.0–4.0 s) passes at rest for the system.

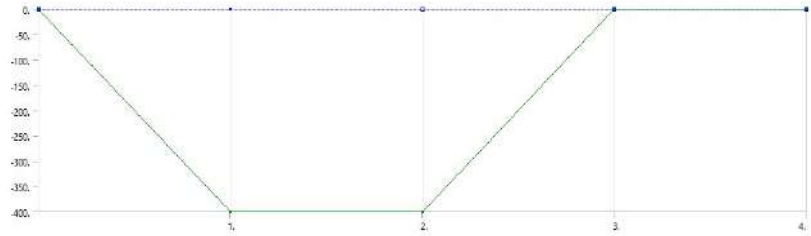

Fig. 2.15. Load application schedule

The purpose of simulating natural load according to such an algorithm is to identify peak stresses during the steady process of loading and residual stresses after releasing the system from the action of forces on it. Traditionally, we make sure that the calculation reached a successful conclusion on the basis of the Force convergence graph, no abnormal jumps between iterations or gaps were recorded, and the time and force curves reached the specified limit – 4.0 c. Thus, we can proceed to the evaluation of model stresses: as expected, the largest value of stresseswas 1082.9 MPa andrecorded at a time of 2.0 s when the force F_p still kept the value of 400 N. This indicator significantly exceeds the yield point of the material and indicates the appearance of plastic deformations. The stress-strain state of the contact spot is shown in Fig. 2.16 – it visually shows a deflection in the central part, which is expected.

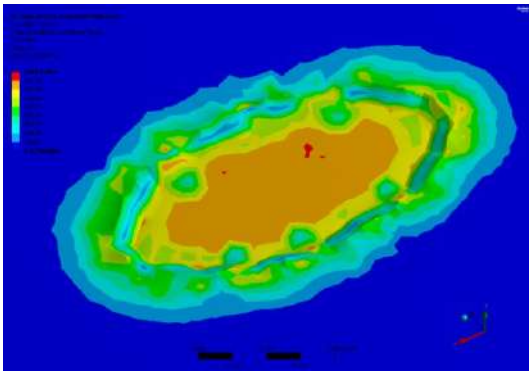

Fig. 2.16. Stress-strain state of the contact patch

The nature of the stress change during loading is the most significant, so let's analyze the key time points of Fig. 2.17.

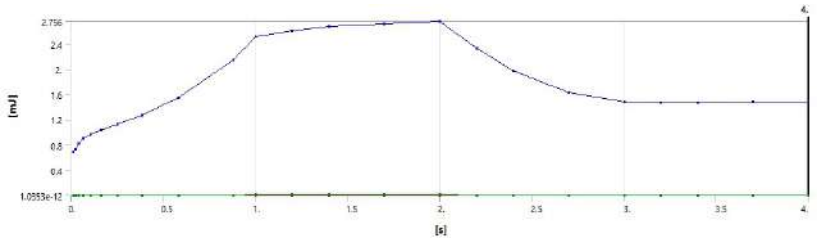

Fig. 2.17. The graph of changes in stress energy in the contact zone depending on time

t = 0.0116 s: at the initial moment of contact between the roller and the shaft (0.0116 s), the stress value was 996.19 MPa and was recorded on the surface of the shaft (max tag). The fact of the location of the max tag is interesting: it is not in the center of the contact patch, as one might expect, but on the periphery. What actually happens: the roller "captured" a certain part of the shaft surface with its contact (the dimensions of the contact surface are 0.8×0.3 mm) and transmits the load to the rest of the shaft body through it. As a matter of fact, maximum stresses are formed at their junctions. Conventionally, this process can be called instant "sticking" of the roller to the shaft in the micro region. Such sticking can also be detected by the contact status graph (Contact Tool > Status) – the spot shows a Sticking-type contact with a sharp contour, which is further smeared, filling with Sliding and Near statuses.

t = 0.0406 s: stress drops to the lowest value throughout the experiment (957.83 MPa) with movement closer to the central part of the contact patch. At the same time, the stress extreme is still on the surface of the shaft. This indicates the end of the momentary process of "sticking" the roller to the shaft established in the previous step – the contact has stabilized: the roller begins to act on the shaft as an independent body, bending it (the deformations of the spot body during loading will be analyzed below).

t = 1.0 s: starting from the previous characteristic moment of time, there is a gradual increase in stresses up to 1058.7 MPa, when the load reached 400 N. The extremum of stresses migrated to a depth of the order of 0.1–0.2 mm, where, under the conditions of temperature load,

the corresponding white layer began to form (Fig. 2.17), which corresponds to the defamation process of the metal surface (the typical depth of the defamation layer is 0.2 mm or more).

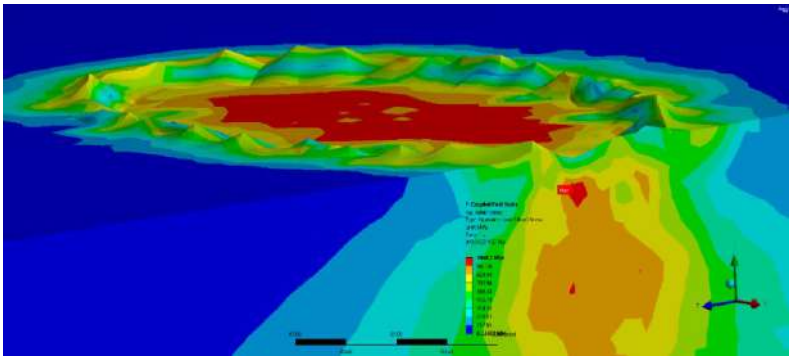

Fig. 2.18. Stress-strained state of the contact spot when forming a white layer

t* = *2.0 s: the force is maintained at 400 N – the system has accumulated maximum energy (2.756 mJ), which can be seen on the Strain Energy graph, and the stresses have increased to 1082.9 MPa. The location of the stress extreme has changed only minimally (within 0.05 mm it has sunk into the shaft body) F_p.

t* = *2.2 s: the force begins to linearly decrease to zero during the period 2.0–3.0 s, therefore turbulent processes appear in the structure of the outer layer – the maximum stress has decreased to 970.05 MPa and moved to the surface of the shaft, but inside the body there is still a zone of high stresses F_p.

t* = *4.0 s: the force remains zero during the last second of the experiment, so the shaft is free and not subjected to loads. The plastic deformation has stabilized, and the residual stresses are 1036 Mpa F_p.

Confirmation of the presence of plastic deformation can also be found on the graph of the vertical movement of the roller (along the *Y* axis) – as can be seen, the contact surface of the roller (Fig. 2.19) did not return to the initial position that corresponded to the beginning of the experiment (0.0 s). The value of the movement of the roller at the end of the experiment was 0.00311 mm, that is, the model did not restore its original location, which means that the shaft received irreversible deformations $t = 4$ s.

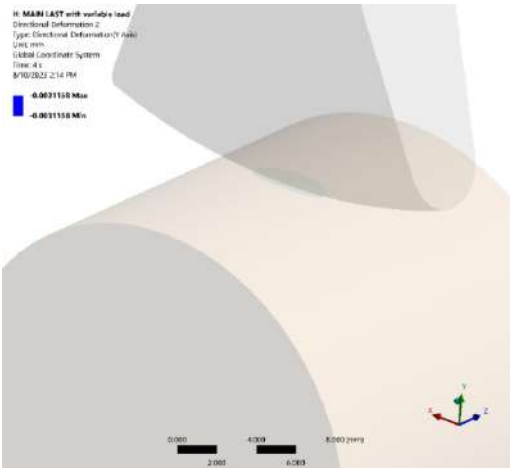

Fig. 2.19. Stress-strained state of the contact spot when after removing the load

The specified dynamics of the movement of maximum stresses from the surface to the body of the model can also be observed on the displacement maps: at the initial moment of contact (t = 0.0116 s) the maximum value was 0.0059 mm, at the time of 1.0 s – 0.0126 mm, and at the end of the experiment – 0.0104 mm. The distribution of heat fluxes over the contact area is expected and adequate in nature – the extremum falls on the central part with a value of 166.06 W/mm^2. Deformations at the peak moment of the experiment (2.0 s) were 0.01384 mm/mm t = 4 s.

Non-linearity of the material significantly affects the magnitude of the stresses in the model, and therefore the resulting plastic deformations. The key factor in the case of the graph of bilinear isotropic hardening (Bilinear Isotropic Hardening) of the Structural Steel material used in Ansys the angle of inclination of the straight line, starting from the point of the yield point, protrudes. The closeness of simulated FEM calculations to full-scale tests of material surface slander depends on the veracity of the strengthening schedule entered into the model (Multilinear, Kinematic, Nonlinear, Chaboche and other types). In fact, each experimental laboratory forms original graphsstresses and strainsbased on their own physical research of samples of material that is their intellectual property. Our task is to create a universal technique to which any graph created in Ansys could be applied.

Conclusions

1. The Ansys Static Structural calculation module turned out to be a sufficient tool in terms of its calculation capabilities. The results of the problem are absolutely adequate within the scope of Hooke's law and carry valuable information about the geometric parameters of the body of the contact spot, which is the basis of the boundary conditions of the problem.

2. The heat load of the surface of the contact spot, together with the consideration of the non-linearity of the material, significantly affects the amount of stress in the upper layers of the shaft, including the formation of the so-called white layer at a depth of about 0.2 mm. The extremum of stress migrates during the loading-unloading process of the shaft from the surface to the body of the shaft and vice versa. The regularity is as follows: as the load on the surface of the shaft increases, the extremum of stress moves inward, starting the formation of the indicated white layer.

3. The applied boundary conditions made it possible to obtain an array of information on residual stresses, deformations and displacements of the model, strain energy graphs, a temperature distribution map, as well as data on the type and nature of contact of bodies during the experiment. Undoubtedly, such a multifactorial model in the form of various input parameters (load, temperature, experiment time, convection, etc.) is a promising object of future research on the analysis of surface strengthening of the outer layers of shafts, and the calculations described in the work can serve as a basis for the formation of original FEM simulation methods natural strengthening of the material, which is especially relevant for experimental laboratories in materials science.

2.3. Optimization of technological parameters at discrete strengthening of steel cylindrical surfaces

Widely used technologies of continuous strengthening of technological surfaces have practically exhausted their capabilities, which calls for the creation of fundamentally new approaches. The application of the principles of discrete-oriented strengthening of tribosystems has broad prospects for improving existing approaches due to the choice of strengthening technology and the principles of the geometric arrangement of strengthening islands. Bearing tribosystems are one of the most common types of friction nodes, which are an

integral and responsible component of modern machines: bearings, axles, shafts, bushings of technological and transport machines. When analyzing the performance of bearing tribosystems, an algorithm for assessing the impact of technological and design factors on their wear resistance and durability is necessary.

Much attention is paid to the problem of creating discretely reinforced surfaces in modern scientific literature. In [51], a study of the properties and characteristics of the surfaces of a discrete structure with mechanically formed depressions was carried out. In work [52] a mathematical model of discrete frictional contact of bodies with periodic surface textures is proposed. The contact problem is reduced to a system of singular integral equations for the functions of the heights of the contact gaps and the relative displacement of the surfaces in the sliding zones. Characteristics of contact deformation and wear of materials with a smooth and discrete track were investigated using nanoindexing and nanoscratching [53]. Wear tests have shown that wear is less for discrete discs than for smooth discs.

Research [54] determined the effect of discrete point laser hardening on abrasion and contact fatigue resistance during rolling. Samples hardened with adjacent and separated laser spots showed higher abrasion resistance than surfaces treated with overlapping laser spots.

In order to improve the surface tribological properties of titanium alloy, laser processing technology was used in [55] to obtain a cellular texture on the surface of the material. Surface textures of grooves with different orientation and distance between them were obtained on the Ti–6Al–4V alloy using a laser in the study [56].

In contrast to traditional research and development of new materials and coatings, three types of surface microstructure, including V-shaped, U-shaped and ring-shaped groove microstructures, were performed in [7] to increase the erosion resistance of sludge. In [8], a groove of a certain size was made, then it was filled with pure phenolic resin and molybdenum sulfide additives to obtain a surface with time-varying contact characteristics. Operational characteristics of friction pairs of a cylinder liner - piston ring of a diesel engine with different surface textures were studied in [9].

Therefore, the problem of creating discrete structures on the surfaces of materials and researching the technological parameters of their formation is an urgent task.

2.3.1. The essence of the process of discrete strengthening of cylindrical parts

The essence of the discrete-oriented strengthening method is the application of combined electromechanical processing and electrocontact cementation of cylindrical surfaces using a carbide roller as a tool. The schematic diagram of DOZ is shown in Fig. 2.20.

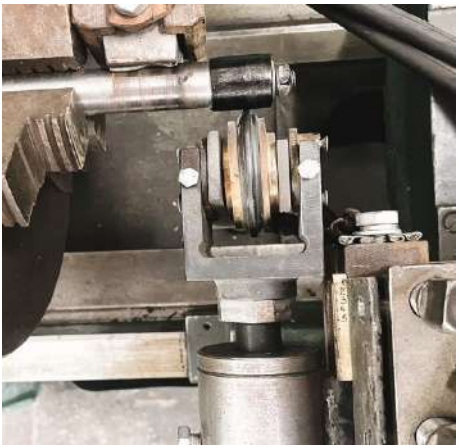

Fig. 2.20. Schematic diagram of the discrete-oriented method of strengthening cylindrical surfaces

The working tool-roller 4 is pressed against the processed workpiece with a given spring force in the range of 100–500 N. One current pole from the power transformer is supplied to the workpiece through the contact roller. The second pole is brought to the processed workpiece. At the same time, an electric discharge occurs between the roller and the tool, which leads to local heating of the contact point. Due to heating, structural transformations similar to the hardening process occur in the surface layers of the metal with the formation of a so-called white layer. Additionally, during processing, the outer surface of the shaft is covered with a layer of graphite by rubbing it with a graphite rod. Graphite, falling into the place of contact between the tool and the workpiece, is also heated and can diffuse into the surface under the action of contact pressure from the roller. That is, there is a local high-temperature diffusion of carbon into the surface of the workpiece, that is, the process of cementation.

The roller and cylinder are set by the shaping movements inherent in the usual processing on a lathe. By setting the movement-feed step, it is possible to form specified processing tracks on the surface of the workpiece.When a large amount of Joule heat is released, the surface of the microvolume is rapidly heated (1000 C/s) with its plastic deformation. Then intense cooling takes place due to heat dissipation inside the material. As a result, a finely dispersed and hard martensitic "white layer" structure with high strength and wear resistance is formed in the surface layer.

The installation allows strengthening of various cylindrical parts, including the bearing necks of the camshaft of the internal combustion engine. To apply the graphite layer on the surface of the workpiece, cylindrical graphite rods with a diameter of 10 mm were used. Samples made of 20X steel were mounted on a cylindrical mandrel, which rested on the conical center of the installation. In the process of rolling with a roller on the surface of the samples, strengthened strips were formed with a step in accordance with the given feed of the movement of the roller (1.5–2 mm).

Optimization of technological parameters of the discrete-oriented method of strengthening bearing tribosystems

The software package for statistical analysis STATISTICA was used to plan the experiment to determine the optimal values of the technological factors of the electrical contact strengthening process. The STATISTICA DOE package module is intended for experiment planning.

The 3-level Box-Behnken plan was used for planning. In statistics, Box–Behnken plots are experimental plots for response surface methodology developed by George E.P. Boxing. Each factor or independent variable is assigned one of three equidistant values, usually coded as –1, 0, +1. (At least three levels are required to achieve the next goal.) The plan should be sufficient to fit a quadratic model, that is, a model containing elements in a square, product of two factors, linear. The ratio of the number of experimental points to the number of coefficients in the quadratic model must be justified (in fact, their plans are kept in the range from 1.5 to 2.6). The variance of the estimate should depend only on the distance from the center of the plan.

2.3.2. Planning of a factorial experiment for establishing optimal processing parameters of the guide

The STATISTICA DOE module contains a complete implementation of standard (block) 3^{**}(kp) plans. The module also includes standard

Box-Behnken plans. As with other plans, it is possible to display and save these plans in standard or random order, request replicas or individual experiments, view the plan and block generators, and more. The program performs a complete analysis of 3^{**}(kp) plans. It is possible to include any effects in the analysis. Main effects are broken down into linear and quadratic effects, and interactions are broken down into linear-linear, linear-quadratic, quadratic-linear, and quadratic-quadratic effects. You can view correlation matrices of factors and effects. The program calculates standard estimates of variance analysis parameters (standard errors, confidence intervals, statistical significance, etc.), coefficients for recoded (–1, 0, +1) factors and coefficients for untransformed factors. The analysis of variance table will contain tests for the linear and quadratic components of each effect and combined tests for effects with many degrees of freedom. If the design contains replicates, the net error estimate can be used for analysis of variance and significance testing; in this case, a general loss of consent test will also be conducted. To interpret the results, the program calculates a table of means (and confidence intervals), as well as marginal means (and confidence intervals) for the interactions. Graphical options include plots of means and marginal means (with confidence intervals), Pareto effects plots, normal and semi-normal probability effect plots, response surface plots, and contour plots.

On the Pareto diagram of the effects, the estimates of the effects of the analysis of variance are arranged by the absolute magnitude of the values: from the largest to the smallest. The magnitude of each effect is represented by a bar, and the bars are crossed by a line indicating how large the effect must be (ie, how long the bar must be) to be statistically significant. It has been established that the main technological parameters affecting the parameters of hardening at DOZ are: the amount of operating current of the power source, the force of pressing the working roller against the surface of the shaft, and the duration of contact between the tool and the processed part. The duration of contact depends on the speed of rotation of the cylindrical part and the size of the contact area, which was estimated when setting the contact parameters. In order to evaluate the influence of the specified factors and determine their optimal values according to the criterion of ensuring maximum hardness, it is advisable to use the methodology of planning the experiment, with the accepted ranges:

Factor	Current strength, A	Effort, N	Contact time, p
min	200	200	0.1
max	800	500	0.3
average	500	350	0.5

In this case, taking into account the planning of the experiment to determine the optimal values of the technological factors of the electrical contact strengthening process, the software package for statistical analysis STATISTICA was used. Taking into account the number of factors and their independent influence on the response function, the 3-level Box-Behnken plan was used for planning:

No. of the experiment	Current strength, A	Effort, N	Contact time, p
1	–1	0	–1
2	–1	–1	0
3	+1	–1	0
4	+1	0	+1
5	0	+1	–1
6	0	0	0
7	0	0	0
8	–1	0	+1
9	+1	0	–1
10	+1	+1	0
11	+1	–1	+1
12	–1	+1	0
13	+1	+1	+1
14	+1	–1	–1
15	+1	0	0

Using the program menu, an experiment plan was formed, which consists of 15 experiments, presented in Table 2.1.

Microhardness was taken as the response function. Next, the Statistica program allows you to perform a variance analysis to determine the effect of processing parameters on the response function. To assess the significance of the factors, a Pareto map was constructed, shown in Fig. 2.21.

On the diagram, the letter L indicates the linear effect of the factor, and the letter K indicates the effect of the factor value in the quadratic equivalent.

Table 2.1

Factorial experiment plan for the DOZ method

No. of the experiment	Current strength, A	Effort, N	Contact time, p	Microhardness, MPa
1	200	350	0.1	4500
2	200	200	0.3	4400
3	800	200	0.3	4900
4	800	350	0.5	5300
5	500	500	0.1	6050
6	500	350	0.3	5800
7	500	350	0.3	6150
8	200	350	0.5	4750
9	800	350	0.1	5000
10	800	500	0.3	5750
11	500	200	0.5	6300
12	200	500	0.3	5250
13	500	500	0.5	6400
14	500	200	0.1	5750
15	500	350	0.3	5900

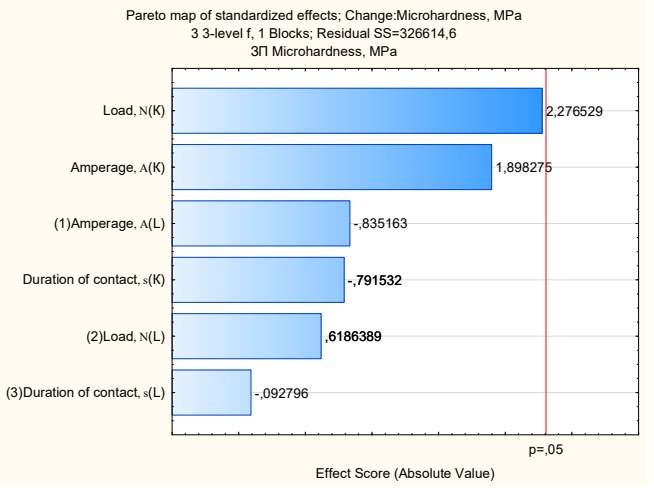

Fig. 2.21. Pareto map of the importance of operating factors

From the analysis of the diagram, it can be seen that the quadratic value of the current and the linear value of the pressing force

have the greatest influence on the microhardness, the contact time has a smaller influence, and the squares of the force and the contact time in the response functions can generally be neglected, since they are beyond the red limit of significance. The results of variance analysis are presented in Table 2.2.

Table 2.2

Results of dispersion analysis

Factor	Analysis of variance; Prm.: Microhardness, MPa; R-squared=.94983; Rate.9122 (3 fact. Box-Behnken plan (Data Table 1) in Plan_7n.stw) 3 3-level f, 1 Blocks; Final.SS=37812.5 ZP Microhardness, MPa				
	SS	ss	MS	F	p
(1) Current strength, (L)	525313	1	525313	13.8926	0.005810
Current strength, A(K)	4119375	1	4119375	108.9421	0.000006
(2) Effort, H(L)	551250	1	551250	14.5785	0.005103
Effort, N(K)	121298	1	121298	3.2079	0.111060
(3) Contact time, s(L)	262812	1	262812	6.9504	0.029882
Contact time, s(K)	144	1	144	0.0038	0.952269

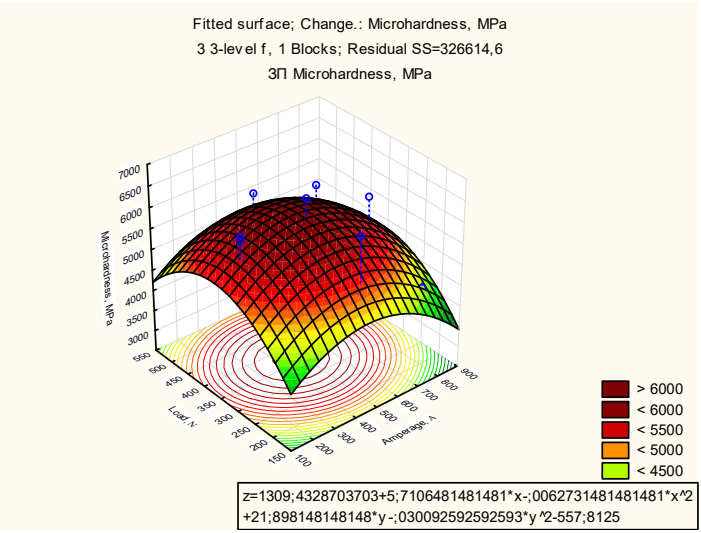

a

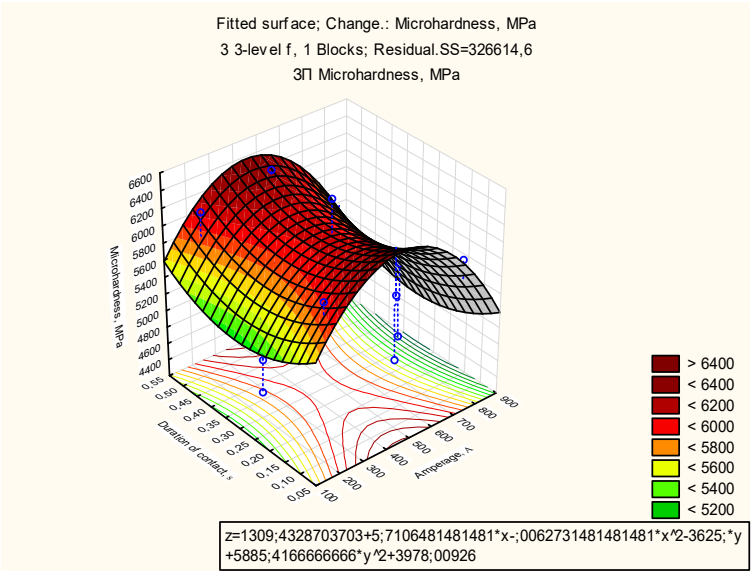

b

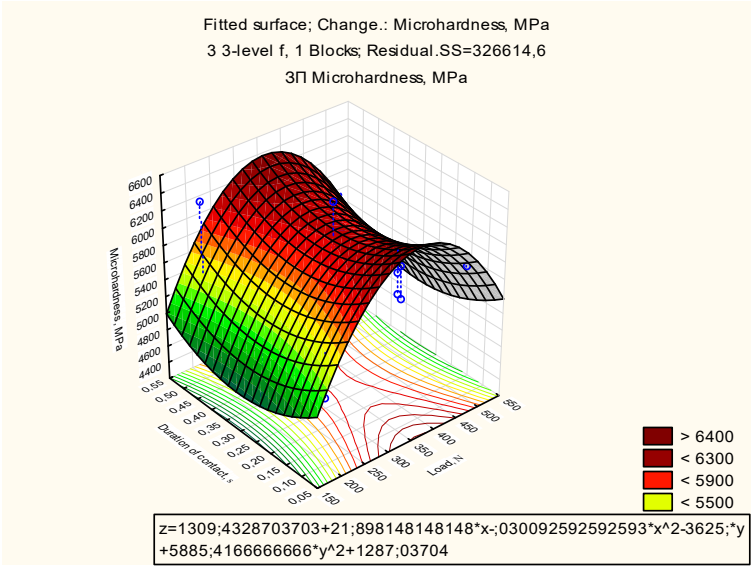

c

Fig. 2.22. Graphs of response functions and approximating correlation functions

In the table, the value of Fisher's test is indicated by the letter F, and the Student's probability test by the letter p. The results shows the adequacy parameters of the built experiment plan, that is, in general, the obtained experiment plan can be considered adequate. Next, graphs of response functions for microhardness from a combination of determining factors were constructed with the help of a software package (Fig. 2.22).

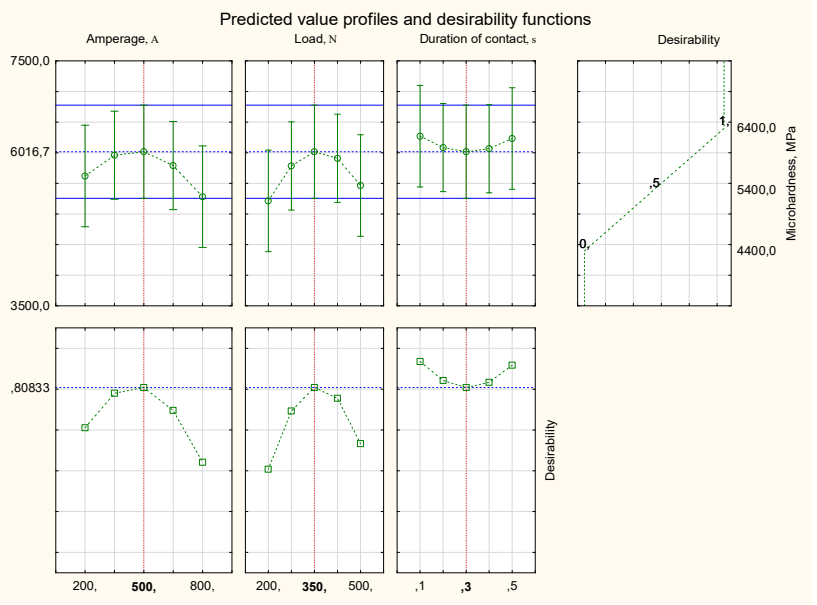

Fig. 2.23. The value of desirability indicators for the maximum value of the response function (microhardness)

So, it follows from the results that to achieve the maximum values of microhardness (5950 MPa), the following optimal parameters of DOZ processing are necessary: current strength – 500 A, force – 350 N, contact time – 0.3 s. Analysis of the obtained graphs shows that the current strength has a clearly defined extreme influence on the microhardness, while the influence of other factors is almost linear.

The results of the regression analysis, that is, the determination of the coefficients of the regression equations, are shown in Table 2.3.

To determine the optimal values of the determining factors of the processing process, a spline approximation of the plan results was carried out using the discrete method according to the criterion of maximum microhardness. In Fig. 4 are given by the results of such approximation.

Table 2.3

Results of regression analysis

Factor	Regression; R-squared=.94983; Rate.9122 (3 fact. Box-Behnken plan (Data Table 1) in Plan_7n.stw) 3 3-level f, 1 Blocks; Final.SS=37812.5 ZP Microhardness, MPa					
	Regression. Coef.	St. Osh.	t(8)	p	-95.% Dov. Pred	+95.% Dov. Pred
Average/ St. Member	2677,257	646,147	4.1434	0.003238	1187.24	4167.275
(1) Current strength, A(L)	12,590	1,148	10.9716	0.000004	9.94	15,236
Current strength, A(K)	-0.012	0.001	-10.4375	0.000006	-0.01	-0.009
(2) Effort, H(L)	-3,889	3,182	-1.2223	0.256372	-11.23	3,448
Effort, N(K)	0.008	0.004	1.7911	0.111060	-0.00	0.018
(3) Contact time, s(L)	1000,000	1556,394	0.6425	0.538515	-2589.05	4589.052
Contact time, s(K)	-156,250	2529,931	-0.0618	0.952269	-5990.28	5677,782

In order to determine the optimal technological parameters of the discrete-oriented method of strengthening with the help of the Statistica program, a factorial experiment according to the Box-Behnken plan was implemented, and the results of dispersion and regression analysis of the influence of processing parameters on microhardness were obtained. It was established that the following optimal parameters of DOZ processing are necessary to achieve the maximum values of microhardness (5950 MPa): current strength – 500 A, force – 350 N, contact time – 0.3 s.

2.4. The influence of texture discreteness on the stress-strain state of the tribosurface after its preliminary profiling

2.4.1. Analysis of the problem of surface layer strength under the influence of normal and tangential stresses in automotive industry components

The problem of surface layer strength under the influence of normal and tangential stresses state belongs to such widespread problems that both scientists and manufacturers of the automotive industry are actually engaged in the study of tribocontact process nature. Among the classic examples of problems in tribotechnics is the well-known rotary engine (RE) of the Mazda company with their most popular model RX-7, which began its history in 1978 and survived until 2012 in the form of a successor RX-8. Thanks to the development of tribology, the fundamental science of studying the problems of friction, wear and reliability, after almost 20 years, Mazda returns to the RE-market with its hybrid MX-30 e-Skyactiv R-EV. In the framework of the following studies, we will analyze the maximum and average stresses at the micro-level with the size of the FEA-model less than 0.5–1.0 mm element length. In addition, we will check the deformations' dependence on the uniformity of the profiled surface of the rolled steel (influence of texture discreteness) beyond the material yield point. To achieve the latter in the Ansys environment, the penetration of the run-in roller into the rolled steel body to a depth of 0.3 mm is simulated, followed by broaching under the press at constant pressure. Among the aims of our research are: confirmation of the hypothesis of average surface stress decrease by the growth of the surface discreteness index, formulation of the hybrid approach for combing the mathematical modeling and FEA. The core idea is to predict the stress rates of the profiled surface based on the geometrical parameters of its notches and the von Mises stress of the smooth surface.

The study [61] examines how geometric notches in maraging tool steel affect its stress-strain behavior during additive manufacturing, finding that higher stress concentration, specific notch shapes, and positions can lead to decreased ductility and increased defect sensitivity, potentially resulting in catastrophic failures. The same author in paper [62] explores the complex interplay between notches, microscale defects, and cyclic loading on the performance of tool steel produced through

additive manufacturing, highlighting the influence of stress concentration, surface quality, and defect-related factors on ductility and fatigue behavior. The notch fatigue factor is described in [63]. The research [64] reveals a significant increase in yield stress with increasing strain rate, underscoring the importance of considering dynamic hardening properties in simulations to achieve more accurate results, as demonstrated in a shot peening simulation where the dynamic properties differed notably from quasi-static ones. Throughout this paper [65], authors aim to explore the impact of work hardening, known as Pre-Straining, and bake hardening on two commonly utilized DP steels to maximize the performance of the materials. The article [66] delves into how the key technological parameters of pendulum surface plastic deformation (SPD) affect the mechanical properties of the surface layer in cylindrical carbon steel components. The authors in paper [67] investigated how the size of impact abrasive particles influences the wear and surface hardening characteristics of high-manganese steel. Impact wear tests were conducted using a MLD-10 tester with abrasive particles measuring 0.75 mm in size. This research [68] presents a numerical analysis of the roll leveling process for third-generation Fortiform 1050 steel, utilizing MSC MARC software and two distinct material laws, followed by the development and assessment of a combined isotropic-kinematic hardening model's impact on the numerical results in comparison to a pure isotropic model. Taking into account we will model the contact of the roller with the rolled steel, it is advisable to get acquainted with [69–72] in relation to research of the influence of kinematic hardening in finite element simulation. In the study [73], laser processing technology was applied to create micro-textures on the surface of 42CrMo steel, aiming to enhance its wear resistance in high-load conditions. The research involved conducting finite element analysis to examine the friction process of the textured components, comparing and measuring various texture forms to optimize their shapes and parameters, and subsequently, fabricating three types of texture shapes (micro-dimples, micro-grooves, and reticular grooves). Besides the surface texturing influence on the hardening and stress level is the topic of [74, 75]. The friction parameters and tribological behavior of surface texturing are described in [76]. However, none of the reviewed sources consider a hybrid approach for determining stresses based on mathematical modeling of notches and von Mises stresses of a smooth surface, which we consider the scientific novelty of our research.

2.4.2. Determine the discreteness impact on the indicators of the stress-strain state of rolled steel surface as a result of profiling

The aim of our Ansys research is to determine the discreteness impact on the indicators of the stress-strain state of rolled steel surface as a result of profiling and subsequent tribocontact under the press. To perform this we will carry out two cases for previously slandering surface with a: smooth roller surface (Task #1) and notched roller surface to achieve the texture discreteness impact (Task #2). For the purity of the experiment with a total duration of 10 s, we will apply the next constant boundary conditions (Fig. 2.24) in both tasks modeled in Ansys.

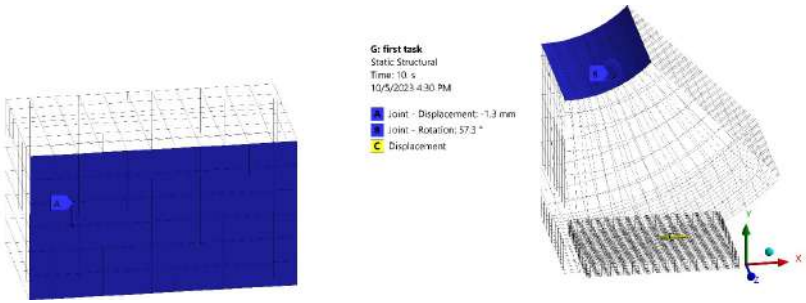

Fig. 2.24. Ansys model of rolled steel with the roller and press (FEA mesh)

Structural Steel NL is applied to the rolled steel and has nonlinear characteristics of the stress-strain curve in Ansys (Bilinear Isotropic Hardering). The yield strength is 250 MPa. A rolled steel has a horizontal surface of 40×50 mm with 4 mm thickness;

Titanium Alloy is used for the press and run-in roller segment and has linear material behavior with 930 MPa (Tensile Yield Strength). The press body for the simulation of tribocontact has a surface of 50×58 mm and a height of 50 mm to be rigid enough;

The kinematics consists of the successive steps: rolled steel horizontal displacement (see tag C in Fig. 2.24 and graph in Fig. 2.25, *a*) and the press vertical travel (see tag A in Fig. 2.23 and graph in Fig. 2.24, *b*) during which the rolled steel is broaching under the pressure – these last 3 seconds are of key interest regarding the processes inside;

Penetration of the roller's body into the rolled steel surface during the period of 6–7 s (Fig. 2.25, *b*) is ensured by their initial

vertical displacement (0.3 mm) that affects the gripping of the rolled steel with its corresponding plastic splashing. When the rolled steel moves under the press, the latter compresses it to flatten the profile formed by the roller's notches.

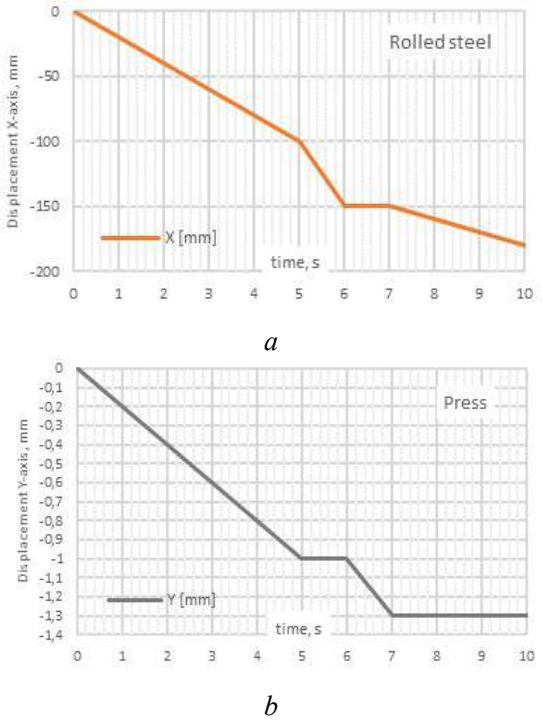

Fig. 2.25. Displacement graphs during the experiment: *a*) rolled steel; *b*) press

The rotation of the roller to an angle θ = 57.3° (see tag B in Fig. 2.24) during the first 5 s of contact with the rolled steel is determined as follows:

$$\theta = \frac{t_{rc} \cdot 180^{\circ}}{\pi r_r}, \tag{2.1}$$

where t_{rc} – rolled steel travel (100 mm); r_r – roller radius (100 mm).

The friction coefficient value was set at 0.2 in the Ansys Static Structural

To estimate model stresses, we will use the concept of Equivalent stresses or "von Mises stresses" σ_{Mis} in Ansys Static Structural). The classical notation of the von Mises stress theory is known and is based on the principal stresses σ_1, σ_2, σ_3. The strength estimate at the studied point of the deformed solid body is given based on the principal stress values determined for each FE.

To calculate the Average stresses, it is necessary to integrate the Equivalent von Mises stresses in each FE by the volume of the model, and then divide them by its total volume (2.2). The following formula is used to calculate the Average stresses:

$$\sigma_{Ave} = \frac{\iiint \sigma_{Mis} dV}{V}, \tag{2.2}$$

where σ_{Ave} – Average stresses, MPa; σ_{Mis} – von Mises stress, MPa; V – volume, m^3.

Given that we will evaluate not only stresses but also deformations, it will be appropriate to understand the concept of surface texture discreteness, provoked by a roller with notches (Task #2): its contact surface consists of diagonal notches with a width of 1.5 mm and a height of 0.2 mm (Fig. 2.26). When setting the step of the notches, equal to their width (1.5 mm), the discreteness coefficient value will be: $K_d = 0.5$. The height of 0.2 mm was not chosen by chance, because it is precisely at a depth of 0.2–0.3 mm from the surface that the so-called "White Layer" (WL) of steel is formed with the concentration of maximum stresses and plastic deformations.

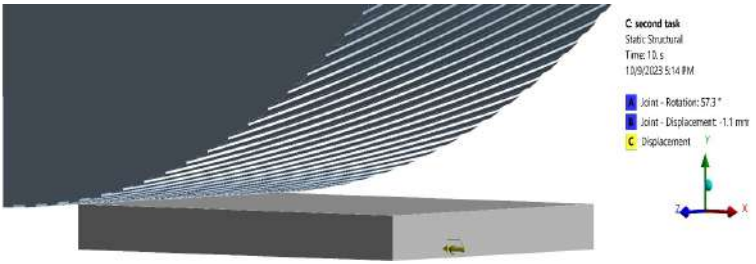

Fig. 2.26. A roller's surface with notches for profiling the rolled steel for discreteness achieving

Calculating surface discreteness usually involves measuring parameters such as roughness height, average roughness, and other surface texture characteristics. One common method to describe the roughness of a surface is to use the R_a parameter, which is the average roughness. R_a is calculated by measuring the vertical deviations of the surface from its ideal form over a specified sampling length.

$$R_a = (1/L) \int_0^L |Z(x)| dx, \tag{2.3}$$

where $Z(x)$ – is the vertical deviation of the surface at position x along the measurement length, mm; L – specified length of the surface, mm.

Incorporating the effect of surface discreteness into the von Mises stress calculation involves considering the impact of surface irregularities, such as notches or discontinuities, on the local stress field. Here are possible different approaches to reflect the effect of discreteness in the von Mises stress calculation.

Stress Concentration Factors (SCFs) are factors used to quantify the increase in stress at a localized region, such as a notch or crack, in a structure compared to the nominal or unnotched stress, like a smooth surface of the rolled steel (Task #1). Taking into account that the notched roller leaves the elliptical-formed holes on the rolled steel, it makes sense to use the next formula (2.4) for the stress concentration factor K_t^e and consider the common case of stress concentration factor K_t:

$$K_t^e = \sqrt{(1 + a^2 / r^2)(1 + b^2 / r^2)}$$

or

$$K_t = \frac{\sigma_{\max}}{\sigma_{\text{nominal}}}, \tag{2.4}$$

where a, b – are the major and minor semi-axes of the ellipse, mm; r – is the distance from the center of the ellipse to the point of interest, mm; $\sigma_{\max}$ – is the maximum stress at the notch tip, MPa; σ_{nominal} – is the nominal (unnotched) stress (formally von Mises stress of the smooth surface), MPa.

This last formula quantifies how much the stress is amplified at the hole's edge compared to the nominal stress. Theoretically, the a

parameter in (2.4) which is a major semi-axe of elliptical notch correspondence to the R_a of (2.3), that enables mathematical programming of the stress distribution along the profiled rolled steel surface by the next algorithm: 1st step – simulate stress on a smooth surface; 2nd step – calculate R_a based on (2.3); 3rd step – apply found value for K_t^e using (2.4).

According to the given algorithm, we can determine the stress in the notches based on the geometry of the surface irregularities and the magnitude of the von Mises stresses, which can be previously calculated for a smooth surface. This is significantly easier and less resources consuming, than sequential FEA iterations, and could be considered an effective and innovative approach.

$$\sigma_{\max} = \sqrt{(1 + a^2 / r^2)(1 + b^2 / r^2)} \cdot \sigma_{Mis}. \tag{2.5}$$

An alternative approach to extending the mathematical modeling in the 2nd step (2.3) is the application of RMSD methodology (Root Mean Square Deviation) – a statistical measure used to determine the differences between values in one data set and another set of values, also derived from data. Let's apply it to our notches case:

$$RSMD = \sqrt{\frac{\sum_{i=1}^{N} (a_i - \overline{a})^2}{n}}, \tag{2.6}$$

where a_i – is the observed value of sample item (vertical semi-axe of the ellipse), mm; $\overline{a}$ – the mean (average) of all values in the data set, mm; n – the size of samples (number of notches).

The novelty of our research is that the proposed method of mathematical modeling can be effective for saving resources when recalculating a solid model in Ansys every time with a preliminary reconstruction of notches on its surface in 3D CAD software. Being said, the FEA mesh (Fig. 2.24) consists of 11,264 elements and 56,713 nodes (Task #1) and 20,479 elements and 64,613 nodes (Task #2). In both cases, the detailing of contact surfaces (especially profiled ones) does not exceed 0.5–1.0 mm for the FE size of the Hexahedron shape. Total Ansys calculation time was 2 h 37 min for the Task #1 using two physical Intel Xeon 24-core, RAM 48 Gb, NVIDIA GeForce 4 Gb video.

The research presented in this section is characterized by scientific novelty due to the hybrid approach of determining the stresses

of a profiled surface based on the geometric parameters of its notches and the von Mises stresses of a smooth surface. Such modeling is much more efficient because of computing and time resources (the notches solid and FEA modeling are not required).

2.4.3. Analysis of the study results on the influence of texture discreteness on the mechanical properties of the surface layer

Notches are stress concentrators on the one hand and literally their transmitters – on the other. Let's compare the von Mises stress results of the rolled steel for both problems (Task #1 and #2 – Table 2.4 and Fig. 2.27). At all key moments of time, the value of the Maximum stresses was higher for Task #2 (Fig. 2.27, *a*), but when comparing the values of the Average stresses, the situation turned out to be the opposite (Fig. 2.27, *b*) – the Average stresses in the profiled rolled steel model with notches (Task #2 with discreteness) were lower than Average stresses in smooth rolled steel (Task #1). An explanation for this can be found in the logic of calculating the value of σ_{Ave} (2.2) – the discreteness of the surface with relief stress drops on average gives lower values than a completely plastically deformed smooth rolled surface as a result of rolling with a smooth roller.

When the roller gripped the rolled surface during the 0.0–1.0 s, the yield strength had already been exceeded (Structural Steel – 250 MPa) – the Maximum stresses were 352 MPa and 430 MPa (Fig. 2.27, *a*), respectively (Task #1 vs Task #2). The extremum of stresses falls on depressions formed by roller notches (Task #2), which provokes displacement at the level of 0.328 mm (Fig. 2.28) unlike 0.227 mm in the case of Task #1.

We can observe tight stress oscillations (Fig. 2.29) during the period of 0–3.05 s when the contact of the roller with the rolled steel continues (Task #2) – this is exactly where the impact of texture discreteness is manifested due to the profiling with notches. The indicated fluctuations can also be observed on the graph of Ansys Contact Tool > Status (Fig. 2.29): the “Max” value corresponds to the Sticking state and “Ave” to Sliding.

Of greater interest for comparison are the residual stresses that can be recorded during the period of 3.7–5.0 s (rolled steel is free of contact – see the break on the graph Fig. 2.30): the maximum stresses were 410 MPa and 459 MPa, and the average stresses were 281 MPa and 259 MPa (Task #1 and # 2, respectively).

Table 2.4

Comparison of von Mises stresses at key points in time

t, s	Task #1	Task #2
1	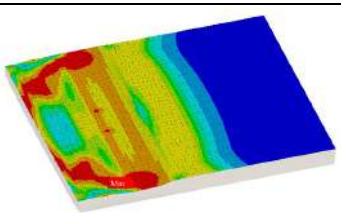	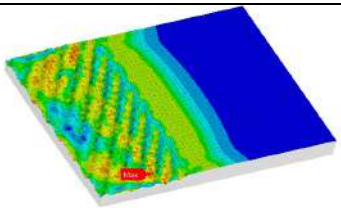
2	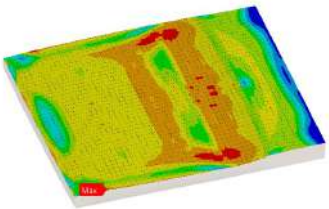	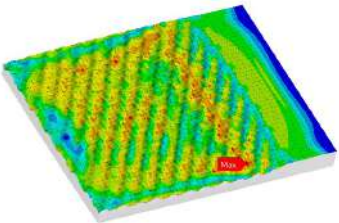
5.4	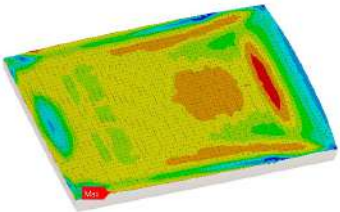	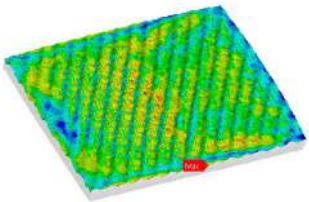
8	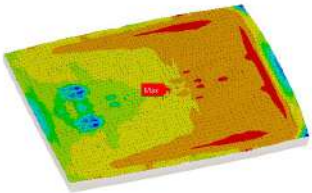	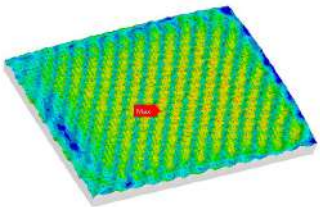
10	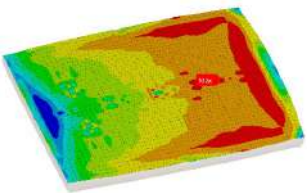	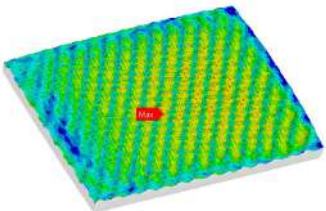

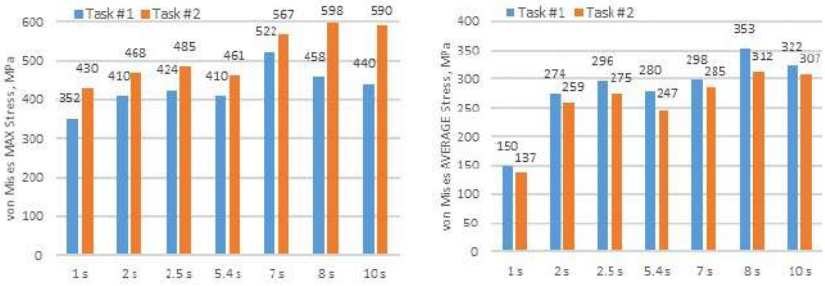

a *b*

Fig. 2.27. Graphs of von Mises stresses at key moments of time *t*, s: *a*) max stress; *b*) average stress

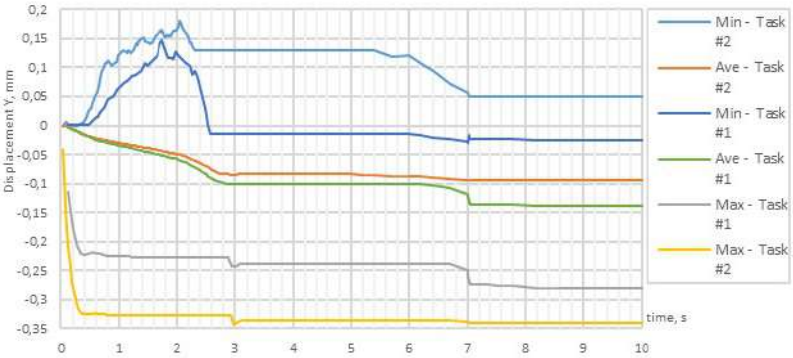

Fig. 2.28. Graphs of displacement at key moments of time *t*, s

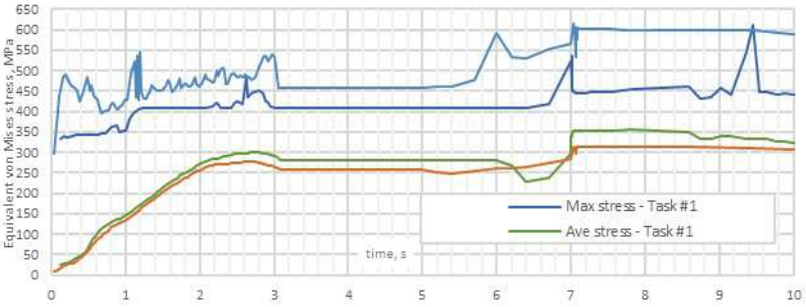

Fig. 2.29. Graphs of von Mises stresses at key moments of time *t*, s

This confirms that in both cases the rolled steel did not recover its shape (see Fig. 2.29), which we can also see on the displacement graph, and remained plastically deformed: max value is 0.335 mm and 0.237 mm for Tasks #1 and Task #2 at time moment of 5.0 s.

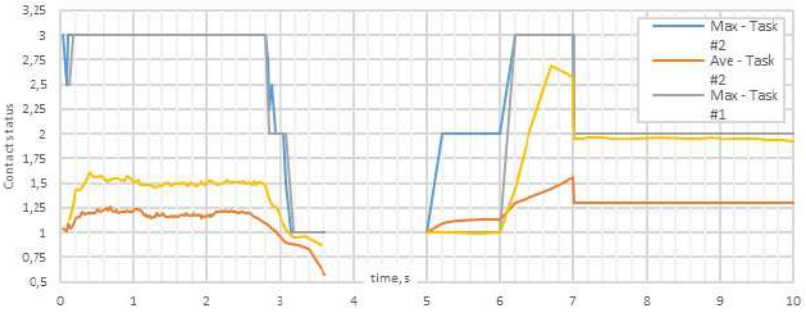

Fig. 2.30. Graphs of Ansys contact status at key moments of time *t*, s

During the period of 6.0–7.0 s (Fig. 2.25, *b*) press performs it vertical displacement of 0.3 mm and compresses the rolled steel surface to flatten its profile formed by the roller's notches. Contact status has Sticking at the moment of t = 7.0 s (Fig. 2.31).

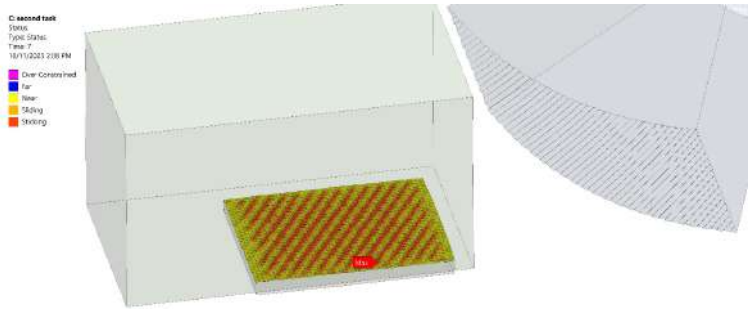

Fig. 2.31. Ansys contact status map at 7.0 s (contact of press with the rolled steel)

The model is maximally compressed during the entire time of the experiment to a value of 7981.4 mm^3, and already at the moment of 7.1 s, when it breaks away from the press, which has just finished its compression (during 6.0–7.0 s), it begins its movement and increases in volume capacity up to 7982.5 mm^3. When rubbed against the surface of

the press as a result of tribocontact, the volume of the rolled steel at the end of the experiment (t = 10 s) increases to 7983.3 mm^3. It should be noted that the stresses at 10.0 s are lower than the stresses at 8.0 s of the experiment in both tasks (Fig. 2.27 and Table 2.1). The reason for this is the adaptation of the rolled steel to the loads from the press, which has already completed its vertical movement by 0.3 mm (Table 2.1) at 7.0 s. Thus, the rolled steel literally "breaks out" from under the roller, performing its horizontal movement. The friction between these elements is reduced as the rolled steel moves (the press remains stationary until the end of the experiment) – the tribocontact changes its character from “Sticking” to “Sliding” Ansys contact status.

These processes of adaptation of the profiled surface to the tribocontact with the press can also be observed by the way the rolled steel surface is leveled – the protrusions have decreased from 0.12 mm (Fig. 2.32, *a*, *b*) at 6.0 s to 0.049 mm (see Fig. 2.32, *c*) at 10.0 s. In addition, they were localized closer to the center of the rolled steel surface, which indicates that the surface at the edges has become almost flat. Thus, it can be said that the process of plastic slander of the surface succeeded, and the phenomenon of discreteness has strengthened it since there was a reduction of Average stresses by 4–5 % compared to a smooth surface (10.0 s).

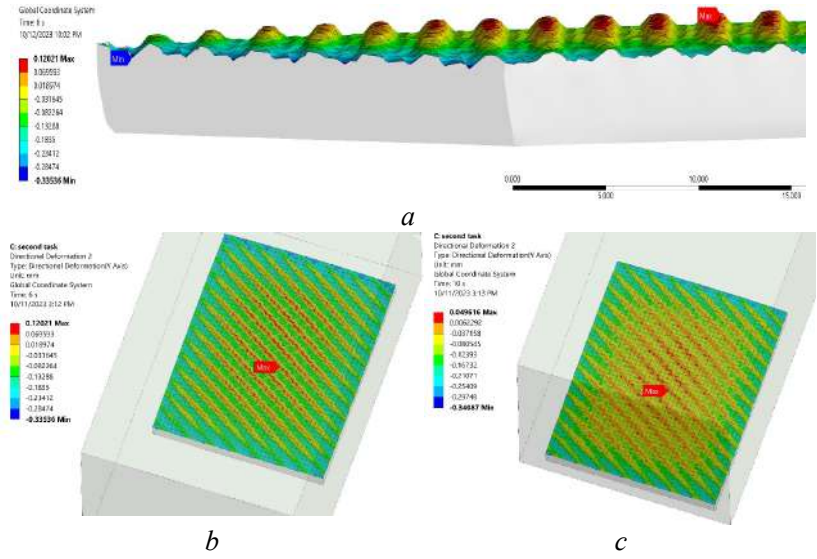

a *b* *c*

Fig. 2.32. Protrusions deformation results at: *a*) 6.0 s; *b*) 10.0 s

In the case of profiling with notches, at the end of the experiment (10.0 s) we have a final increase in Maximum stresses by 34.2 % relative to the smooth surface. If we compare a more weighted indicator (Average Stress), then due to the alternation of different stress zones, which is a manifestation of discreteness, the Average stress values of a profiled surface were always lower than a smooth one. Thus, from the point of view of stresses beyond the yield point, the rolled steel suffered less due to the discreteness. The phenomenon of discreteness plays a significant role when working on contact problems with texture profiling – the transition from a flat surface to a relief one with notches, which are stress concentrators on one side, and literally their transmitters – on the other. Summarizing the conducted research, there are reasons to judge the practical effectiveness of tribocontact FEA methodologies similar to the one presented, where various profiling configurations are taken into account. The mathematical approach presented in the paper is also valuable, where based on the stress values of the smooth surface and the geometric parameters of the profile, mathematical modeling can be carried out, which precedes the more resourceful FEA. This is significantly less resources consuming, than sequential FEA iterations, and could be considered an effective and innovative approach for designing the new best-performance profiled surfaces.

Conclusions

The texture discreteness effect has a great influence on the mechanical properties of the surface layer. Thus, the maximum stresses at the end of the experiment 10.0 s are higher by 34.2 % in the case of Task #2 (profiled surface with notches) than Task #1 (590 MPa vs. 440 MPa). Max values are fixed on the ends of notches, which act as dampers and are the first to perceive the load.

In contrast to Maximum stresses, the situation with Average stresses (a more objective and important parameter) is the opposite: as the discreteness of the surface increases, the Average stresses decrease. For comparison: at 10.0 s, the value for Task #1 was 322 MPa, and Task #2 was 307 MPa. The last value is valuable, it is quite possible to choose the geometric parameters of the roller notches in such a way that the Average stresses on the surface remain within the limits of Hooke's law (elastic deformation).

The final tribocontact of rolled steel at constant press pressure gives positive results – the surface is smoothed: the maximum amplitude

of irregularities decreased from 0.12 mm to 0.049 mm during the last step, and the stresses even dropped by almost 2 % just in the period of 8.0–10 s.

Precisely the hybrid algorithm of the mathematical modeling proposed by us and based on the application of the flat surface stress value and the geometric parameters of the notches serves for achieving the optimal discreteness. This stage precedes the FEA verification calculation.

References for Chapter 2

1. Zhao B, Zhang S, Li J, Wang P. Friction characteristics of sliding guideway material considering original surface functional parameters under hydrodynamic lubrication. Proceedings of the Institution of Mechanical Engineers, Part J: Journal of Engineering Tribology. 2017; 231(7): 813–825. doi:10.1177/1350650116681941

2.Tao, W., Zhong, Y., Feng, H., & Wang, Y. (2013). Model for wear prediction of roller linear guides. Wear, 305(1–2), 260–266.

3. Soleimanian, P., & Ahmadian, H. (2022). Modeling friction effects in lubricated roller guideways using a modified LuGre model. Journal of Vibration and Control, 28(19–20), 2519–2530.

4. Bao, H., Hao, M., Du, Y., & Chen, Y. (2024). Optimal Design of Multilevel Composite Lubrication Structures on Sliding Guide Rail Surfaces. Coatings, 14(10), 1286.

5. Fan, Y., Chen, Y., Hao, M., Wang, S., Du, Y., Xia, Y.; Guan, X. Study on the improvement of crawling phenomenon of sliding guideway by composite lubrication texture. China Mech. Eng. 2024, 1–8.

6.Huan, Z. H. A. O., Yuanka, Z. H. O. U., & Xue, Z. U. O. (2022). Anti-friction Performance of Composite Lubrication Structure Surface under Oil-lubrication. Lubrication Engineering (0254–0150), 47(10).

7. Rodiouchkina, M., Berglund, K., Forsberg, F., Rodushkin, I., & Hardell, J. (2022). Influence of counter surface roughness and lay on the tribological behaviour of self-lubricating bearing materials in dry sliding conditions at high contact pressures. Lubricants, 10(8), 167.

8. Soleimanian, P., Mohammadpour, M., & Ahmadian, H. (2021). Effect of Lubricant Starvation on the Tribo-Dynamic Behavior of Linear Roller Guideway. Shock and Vibration, 2021(1), 7517696.

9. Soleimanian, P., Mohammadpour, M., & Ahmadian, H. (2021). Coupled tribo-dynamic modelling of linear guideways for high precision machining application. Proceedings of the Institution of Mechanical Engineers, Part J: Journal of Engineering Tribology, 235(4), 711–737.

10. Li, L., & Yang, J. (2018). A study of dynamic behaviors of contact pair in lubricated ball linear guide. Industrial Lubrication and Tribology, 70(4), 746–753.

11.Zou, H. T., & Wang, B. L. (2015). Investigation of the contact stiffness variation of linear rolling guides due to the effects of friction and wear during operation. Tribology international, 92, 472–484.

12. Wang, Z., Liu, Y., & Wang, F. (2017). Rapid calculation method for estimating static and dynamic performances of closed hydrostatic guideways. Industrial Lubrication and Tribology, 69(6), 1040–1048.

13. Liu, W., Zhang, S., Lin, J., Jiang, S., & Chen, Z. (2024). Effect of combined geometric errors on static load distribution and deformations for linear rolling guide. Tribology International, 191, 109079.

14. Zha, J., Cheng, K., Xue, F., Wu, D., & Liu, X. (2024). Hydrostatic guideways for precision machines: the state-of-the-art and future perspectives. Tribology International, 110060.

15. Raymond, N., Hill, S., & Soshi, M. (2016). Characterization of surface polishing with spindle mounted abrasive disk-type filament tool for manufacturing of machine tool sliding guideways. The International Journal of Advanced Manufacturing Technology, 86, 2069–2082.

16. Zsidai, L., De Baets, P., Samyn, P., Kalacska, G., Van Peteghem, A. P., & Van Parys, F. (2002). The tribological behaviour of engineering plastics during sliding friction investigated with small-scale specimens. Wear, 253(5–6), 673–688.

17. Ghiotti, A., Bruschi, S., Sgarabotto, F., & Medea, F. (2014). Novel wear testing apparatus to investigate the reciprocating sliding wear in sheet metal forming at elevated temperatures. Key Engineering Materials, 622, 1158–1165.

18. Chang, K. C. J. (2016). Development of New Machining Method for Finish Surface of Sliding Guideways. University of California, Davis.

19. Chang, K., & Soshi, M. (2017). Optimization of Planar Honing Process for Surface Finish of Machine Tool Sliding Guideways. Journal of Manufacturing Science and Engineering, 139(7), 071015.

20. Soshi, M., Ueda, E., & Mori, M. (2014). A productive and cost-effective CBN hard milling-based fabrication method of hardened sliding guideways made of refined cast iron. The International Journal of Advanced Manufacturing Technology, 70, 911–917.

21.Horng, T. L. (2013). The study of contact pressure analyses and prediction of dynamic fatigue life for linear guideways system. Modern Mechanical Engineering, 3(02), 69–76.

22. Wang, X. Y., Zhou, C. G., & Ou, Y. (2019). Experimental analysis of the wear coefficient for the rolling linear guide. Advances in Mechanical Engineering, 11(1), 1687814018821744.

23. He, Y., Fu, Y., Wang, H., & Yang, J. (2022). Enhancing anti-stick-slip performance by laser surface texturing on sliding guideway surface. Journal of Manufacturing Processes, 75, 1089–1099.

24. He, Y., Yang, J., Wang, H., Gu, Z., & Fu, Y. (2022). Micro-dimple and micro-bulge textures: Influence of surface topography types on stick–slip behavior under starved lubrication. Applied Surface Science, 585, 152501.

25. Cheng, Q., Qi, B., Ren, W., & Liu, Z. (2021). A new exponential wear model to analyze precision retention of guideway based on macro-micro multiscale method. Proceedings of the Institution of Mechanical Engineers, Part J: Journal of Engineering Tribology, 235(8), 1499–1513.

26. Horng, T. L. (2013). The study of contact pressure analyses and prediction of dynamic fatigue life for linear guideways system. Modern Mechanical Engineering, 3(02), 69–76.

27. Zhang, H., Lu, D., Pan, W., Rong, X., & Zhang, Y. (2024). Static and dynamic characteristics of large-span six-slider closed hydrostatic guideway considering pitch moment and yaw moment. Industrial Lubrication and Tribology, 76(3), 392–404.

28. Wang, H., Xie, X., Hua, X., Xu, S., Yin, B., & Qiu, B. (2020). Analysis of the lubrication process with composition of solid lubricants of laser-modified sliding surfaces. Advances in Mechanical Engineering, 12(4), 1687814020916078.

29. Shimizu, Jun, et al. "Friction characteristics of mechanically microtextured metal surface in dry sliding." Tribology International 149 (2020): 105634.

30. Forsberg, P., Debord, D., & Jacobson, S. (2014). Quantification of combustion valve sealing interface sliding – A novel experimental technique and simulations. Tribology International, 69, 150–155. https://doi.org/10.1016/j.triboint.2013.09.014

31. Teimouri, R., Grabowski, M., Skoczypiec, S.: Modeling of surface hardening in burnishing process. Materials Research Proceedings, Vol. 28, pp. 1223–1234. DOI: 10.21741/9781644902479-133 (2023).

32. Hu, X., Qu, S., Chen, Z., Zhang, P., Lu, Z., Lai, F., Duan, C., Li, X.: Rolling contact fatigue behaviors of 25CrNi2MoV steel combined treated by discrete laser surface hardening and ultrasonic surface rolling, Optics & Laser Technology, Volume 155, 108370, ISSN 0030-3992, DOI: 10.1016/j.optlastec.2022.108370 (2022).

33. Dykha, A., Makovkin, O., Dykha, M. (2020). Influence of Discrete Electromechanical Hardening on the Wear Resistance of Steels. In: Ivanov, V., et al. Advances in Design, Simulation and Manufacturing II.

DSMIE 2019. Lecture Notes in Mechanical Engineering. Springer, Cham. https://doi.org/10.1007/978-3-030-22365-6_55.

34. Souza, P. S., Cangussu, V. M., Câmara, M. A., Abrão, A. M., Denkena, B., Breidenstein, B., Meyer, K.: Formation of White Etching Layers by Deep Rolling of AISI 4140 Steel. Journal of Materials Engineering and Performance, 29(7), pp. 4351–4359. DOI: 10.1007/s11665-020-04988-3 (2020).

35. Schulze, V., Bleicher, F., Groche, P., Guo, Y.B., Pyun, Y.S.: Surface modification by machine hammer peening and burnishing, CIRP Annals, Volume 65, Issue 2, ISSN 0007–8506, pp. 809–832. DOI: 10.1016/ j.cirp.2016.05.005 (2016).

36. Yu, J., Chen, J., & Ho, H. (2023). Effect of laser cladding Ti/B4C/dr40-based composite coatings for the surface strengthening of shaft part. Optics & Laser Technology, 157, 108721.

37. Wang, Y. X., Yang, Z., Dai, J. W., Zhao, X. M., & Mao, X. Y. (2020). Research on surface strengthening induced by ultrasonic punching to improve mechanical properties and corrosion resistance for shaft parts. Surface Review and Letters, 27(01), 1950086.

38. Liu, L., JianLin, W., ZiMeng, Y., ShenLi, W., XiaoMing, L., & BinFeng, H. (2023). Research on Surface Strengthening Treatment and Performance of Sewing Machine Shaft Parts. Integrated Ferroelectrics, 237(1), 287–296.

39. Qi Liu, Yang Liu, Xing Li, Guangneng Dong. Pulse laser-induced cell-like texture on surface of titanium alloy for tribological properties improvement. Wear, Volume 477, 2021, https://doi.org/10.1016/ j.wear.2021.203784.

40. Jianfei Wang, Weihai Xue, Siyang Gao, Shu Li, Deli Duan. Effect of groove surface texture on the fretting wear of Ti–6Al–4V alloy. Wear, Volum 486–487, 2021, https://doi.org/10.1016/j.wear.2021.204079./ Zhang, K., Ma, J., Zou, J., Liu, Y.: Surface microstructure and property modifications in a duplex stainless steel induced by high current pulsed electron beam treatments. J. Alloy Compd. 2017, 707, pp. 178–183. ISSN 0925–8388, DOI: 10.1016/j.jallcom.2017.01.003 (2017).

41. Quan, N., Yang, C.-Y.: A modified Newton–Raphson method to estimate the temperature-dependent absorption coefficient in laser welding process, International Journal of Heat and Mass Transfer, Volume 102, ISSN 0017–9310, pp. 1222–1229. DOI: 10.1016/j.ijheatmasstransfer./ 2016.07.034 (2016).

42. Buchkremer, S., Klocke, F., Döbbeler, B., Abouridouane, M., Meurer, M.: Thermodynamics-based Interpretation of White Layer Formation in Metal Cutting, Procedia CIRP, Volume 58, ISSN 2212-8271, pp. 370–374. DOI: 10.1016/j.procir.2017.03.328 (2017).

43. Zhang, X. M., Chen, L., Ding, H.: Effects of process parameters on white layer formation and morphology in hard turning of AISI52100 steel. Journal of Manufacturing Science and Engineering, 138(7), 074502. DOI: 10.1115/1.4032769 (2016).

44. Chen, Z., Hörnqvist Colliander, H., M., Sundell, G., Peng, R. L., Zhou, J., Johansson, S., Moverare, J.: Nano-scale characterization of white layer in broached Inconel 718, Materials Science and Engineering: A, Volume 684, ISSN 0921–5093, pp. 373–384. DOI: 10.1016/j.msea.2016./ 12.045 (2017)

45. Wan, L.-B., Li, S.-X., Lu, S.-Y., Su, Y.-S., Shu, X.-D., Huang, H.-B.: Case study: Formation of white etching layers in a failed rolling element bearing race, Wear, Volumes 396–397, ISSN 0043-1648, pp. 126–134. DOI: 10.1016/j.wear.2017.07.014 (2018).

46. Zhou, Y., Peng, J. F., Luo, Z. P., Cao, B. B., Jin, X. S., Zhu, M. H.: Phase and microstructural evolution in white etching layer of a pearlitic steel during rolling–sliding friction, Wear, Volumes 362–363, ISSN 0043–1648, pp. 8–17. DOI: 10.1016/j.wear.2016.05.007 (2016).

47. Zhao, C., Ma, C., Yang, J., Li, M., Zhao, Q., Ma, H., Jia, X.: Numerical Simulation Study of Multi-Field Coupling for Laser Cladding of Shaft Parts. Micromachines. 14. 493. 10.3390/mi14020493 (2023).

48. Dykha, A., Holenko, K., Padgurskas, J., Babak, O.: Thermal and stress-strain state of friction pairs in ventilated disc brakes of lightweight vehicles. Problems of Tribology. 28, pp. 41–50. 10.31891/2079-1372-2023-107-1-41-50 (2023).

49. Holenko, K., Koda, E., Kernytskyy, I., Babak, O., Horbay, O., Popovych, V., Chalecki, M., Leśniewska, A., Berezovetskyi, S., Humeniuk, R.: Evaluation of Accelerator Pedal Strength under Critical Loads Using the Finite Element Method. Appl. Sci. 2023, 13, 6684. https://doi.org/10.3390/ app13116684 (2023).

50. Durville, D. (2005). Numerical simulation of entangled materials mechanical properties. Journal of materials science, 40, 5941–5948.

51. Marchuk V., Kindrachuk M., Kryzhanovskyi A. System analysis of the properties of discrete and oriented structure surfaces. Aviation. 2014. No. 18 (4). R. 161–165. http://dx.doi.org/10.3846/16487788.2014.985474

52. Slobodyan BS, Lyashenko, BA, Malanchuk, NI, Marchuk VE, Martynyak RM Modeling of Contact Interaction of Periodically Textured Bodies with Regard for Frictional Slip. 2016. Volume 215, Issue 1. P. 110–12. https://doi.org/10.1007/s10958-016-2826-x

53. Yoon Y. & Talke FE Microsyst Technol. 2011. 17: 733. https://doi.org/10.1007/s00542-011-1239-5

54. Ann Zammit, Stephen Abela, John Charles Betts, Remigiusz Michalczewski, Marek Kalbarczyk, Maurice Grech. Scuffing and rolling contact

fatigue resistance of discrete laser spot hardened austempered ductile iron. Wear. 2019. Vol. 422–423. Pp. 100–107. https://doi.org/10.1016/ j.wear.2019.01.061

55. Qi Liu, Yang Liu, Xing Li, Guangneng Dong. Pulse laser-induced cell-like texture on the surface of titanium alloy for tribological properties improvement. Wear. 2021. Vol. 477. https://doi.org/10.1016/ j.wear.2021.203784

56. Jianfei Wang, Weihai Xue, Siyang Gao, Shu Li, Deli Duan. Effect of groove surface texture on the fretting wear of Ti–6Al–4V alloy. Wear. 2021. Volumes 486-487. https://doi.org/10.1016/j.wear.2021.204079

57. ZX Chen, HX Hu, YG Zheng, XM Guo. Effect of groove microstructure on slurry erosion in the liquid-solid two-phase flow. Wear. 2021. Volumes 466-467. https://doi.org/10.1016/j.wear.2020.203561

58. AY Wang, JL Mo, HH Qian, YK Wu, ZY Xiang, W. Chen, ZR Zhou. The effect of a time-varying contact surface on interfacial tribological behavior via a surface groove and filler. Wear. 2021. Volumes 478–479. https://doi.org/10.1016/j.wear.2021.203905

59. Liang Rao, Chenxing Sheng, Zhiwei Guo, Chengqing Yuan. Effects of thread groove width in cylinder liner surface on performances of diesel engine. Wear. 2019. Volumes 426-427. Part B. Pr. 1296–1303. https://doi.org/10.1016/j.wear.2018.12.0703.

60. Lu, Ping & Wood, Robert. (2020). Tribological performance of surface texturing in mechanical applications – a review. Surface Topography: Metrology and Properties. 8. 10.1088/2051-672X/abb6d0.

61. Afkhami, Shahriar & Lipiäinen, Kalle & Javaheri, Vahid & Amraei, Mohsen & Salminen, Antti & Björk, Timo. (2023). Effects of notch-load-defect interactions on the local stress-strain fields and strain hardening of additively manufactured 18Ni300 steel. 876. 145165. 10.1016/ j.msea.2023.145165.

62. Afkhami, Shahriar & Dabiri, Edris & Lipiäinen, Kalle & Piili, Heidi & Björk, Timo. (2021). Effects of notch-load interactions on the mechanical performance of 3D printed tool steel 18Ni300. Additive Manufacturing. 47. 102260. 10.1016/j.addma.2021.102260.

63. Nicoletto, Gianni & Konečná, Radomila & Kunz, Ludvík & Frkáň, Martin. (2018). Influence of as-built surface on fatigue strength and notch sensitivity of Ti6Al4V alloy produced by DMLS. MATEC Web of Conferences. 165. 02002. 10.1051/matecconf/201816502002.

64. Lee, Sungbo & Yu, Kwanghyun & Huh, Hoon & Kolman, Radek & Arnoult, Xavier. (2022). Dynamic Hardening of AISI 304 Steel at a Wide Range of Strain Rates and Its Application to Shot Peening Simulation. Metals. 12. 403. 10.3390/met12030403.

65. Vegi, Nischay & Ragothaman, Balakrishnan. (2023). Effect of Varying Levels of Work Hardening and Bake Hardening on the Mechanical Properties of Dual Phase Steels. 10.4271/2023-28-1331.

66. Zaides, S. & Quan, Ho. (2023). Degree and depth of hardening under pendulum surface plastic deformation of carbon steel. Izvestiya. Ferrous Metallurgy. 66. 272-282. 10.17073/0368-0797-2023-3-272-282.

67. Wang, Yongjin & Song, Chuansongxin & Song, Renbo & Ma, Zetian & Taylor, Tom. (2023). Size Effect of Impact Abrasive Particles on Wear and Surface Hardening Behavior of High-Manganese Steel. Acta Metallurgica Sinica (English Letters). 10.1007/s40195-023-01540-9.

68. Galdos, Lander & Sáenz de Argandoña, Eneko & Mendiguren, Joseba & Silvestre, Elena. (2017). Numerical simulation of the roll levelling of third generation fortiform 1050 steel using a nonlinear combined hardening material model. Journal of Physics: Conference Series. 896. 012122. 10.1088/1742-6596/896/1/012122.

69. Baru, Naveen Krishna & Laugwitz, Marvin & Jochum, Martin & Lohmar, Johannes. (2022). On Considering the Influence of Kinematic Hardening in Finite Element Simulation of Hot Levelling of Structural Steel Heavy Plates. Key Engineering Materials. 926. 1993–2003. 10.4028/p-931ugj.

70. Wang, Yu & Mehari, Zelalem & Wu, Junyuan & Han, Jingtao. (2022). Optimization design of process parameters for cold and hot composite roll forming of the AHSS square tube using response surface methodology. The International Journal of Advanced Manufacturing Technology. 123. 1–16. 10.1007/s00170-022-10119-0.

71. Perzynski, K. & Pyzynski, Kamil & Swierczynski, Sebastian & Pidvysots'kyy, Valeriy & Klis, Janusz & Madej, Łukasz. (2022). Influence of the roll leveler setup parameters on the quality of high-strength steel leveling operation. The International Journal of Advanced Manufacturing Technology. 120. 10.1007/s00170-022-08877-y.

72. Guan, Y. & Yan, Y. & Wang, H.. (2018). FEM simulation of flexible roll forming based on different material models. High Technology Letters. 24. 434-439. 10.3772/j.issn.1006-6748.2018.04.013.

73. Zhang, Hua & Pei, Xinfeng & Jiang, Xindong. (2023). Anti-Wear Property of Laser Textured 42CrMo Steel Surface. Lubricants. 11. 353. 10.3390/lubricants11080353.

74. Gachot, Carsten & Rosenkranz, Andreas & Hsu, Stephen & Costa, Henara. (2016). A critical assessment of surface texturing for friction and wear improvement. Wear. 372. 10.1016/j.wear.2016.11.020.

75. Arulkumar, M. & Rangan, Prashanna & Ananth, Prem & Srividhyasakthi, V. & Aaditya, R.. (2023). Experimental verification on the influence of surface texturing on biomaterials and study of its tribological characteristics. 10.1016/j.matpr.2023.01.172.

Chapter 3

Modern approaches to modeling dynamic processes, contact parameters, wear and reliability of structural elements of transport systems

3.1. Modeling of mechanisms of nonlinear collector tribodynamics of magnetization in ferroresonance regimes

Research into nonlinear ferroresonance processes is stimulated primarily by the tasks related to the electric power industry in which abnormal ferroresonance overvoltage and overcurrent cause emergency shutdowns and damage to expensive equipment. Despite the wide range of numerical-analytical and graph-analytical methods for preventing this kind of regimes, the number of accidents in this field is constantly increasing, which is why further study of the physical mechanisms underlying ferroresonance excitations remains relevant. The complexity of power grids explains the formalization of their calculations based on Kirchhoff's quasi-static laws for electric and magnetic circuits. However, these laws do not sufficiently take into account wave processes in nonlinear ferromagnetic elements, and the calculations are based on quasi-static magnetization curves and the corresponding Weber-ampere characteristics. In the context of Maxwell's equations, this approach corresponds to the choice of electric and magnetic field strengths as a basis. An alternative record of material relations for closing the system of Maxwell's equations due to the induction (and not due to the intensity) of the magnetic field is practically not used. Meanwhile, the very large indices of magnetic permeability of ferromagnets bring to the fore the induction of the magnetic field in the material, the nonlinear dynamics of which, in fact, predetermines the overvoltage and overcurrent induced. Therefore, research into the development of such an alternative is a relevant task.

The use of magnetic conductors in the power industry significantly reduces the dynamic range of ferroresonances – mainly to the industrial frequency (50 Hz) and its subharmonics (25 Hz, 16.7 Hz, etc.). At the

same time, the widespread use of magnetic dielectrics in radio engineering transfers the phenomenon of ferroresonance to the range of sound and ultrasonic frequencies, in which the role of wave processes increases significantly. This range eventually borders on the ultra-high-frequency radio range of ferromagnetic and ferrimagnetic resonances, which are studied by radio spectroscopy methods. A known result of such studies is the cooperative nature of the processional motion of solid-state spin magnetic moments in a strong permanent magnetic field. On the other hand, the cooperation of magnetic moments in a relatively weak alternating field of oscillating radio technical systems has not been sufficiently investigated. This actualizes the comparative analysis of magnetization dynamics of conducting and dielectric ferromagnets in an external as well as in an internal electromagnetic field. Features of dielectric ferro- and ferrimagnetic systems are an additional mesoscopic mechanism of polarization of the material caused by the accumulation of electric charges on structural inhomogeneities, as well as magnetostriction. These factors provide pronounced electromagnetic and acoustic emission upon excitation of ferroresonances, which must be used for diagnostics and experimental research of such resonances.

It is advisable to describe ferroresonance processes in electromechanical analogies with contact tribodynamics, in which contact hysteresis is an analog of magnetic hysteresis. At the same time, quasi-static neglect of wave processes leads to unexpected emergency excesses of dynamic contact reactions over quasi-static ones, crack formation and deep sub-contact damage of the material under resonant modes. The commonality of the mathematical description of electrical and mechanical oscillatory and wave processes actualizes this kind of comparative analysis.

Ferroresonances are formed under thermodynamically unbalanced conditions of balance (or imbalance) of energy pumping and energy dissipation. In this regard, when describing them, the terms "nonlinear dissipative system" and "non-equilibrium dissipative system" are usually used, emphasizing the scattering processes. At the same time, the alternative attraction of non-equilibrium systems to the accumulation (rather than dissipation) of the energy of the electromagnetic field and the energy of the magnetic moments in the field is not taken into account. Direct transfer of known tendencies of quasi-equilibrium systems to stable equilibrium states corresponding to the energy minimum is not always adequate under non-equilibrium conditions. In this regard, the problem of researching ferroresonance regimes, which are manifold in

their content, is relevant, under which the system of spin magnetic moments of a ferromagnet goes to an unstable state of equilibrium, corresponding to the energy maximum in the surrounding field.

3.1.1. Analysis of studies of resonance processes in tribological dynamic systems

Works [1, 2] report the results of experimental studies of ferroresonance processes in industrial electrical networks and their components with nonlinear inductive elements. The authors proposed methods of multifactorial analysis and prediction of emergency-dangerous ferroresonance modes of equipment operation. However, questions remain regarding the completeness of the description of magnetization dynamics under ferroresonance conditions because in these works, as in this field in general, the consideration is based on the intensity of the external magnetic field. An alternative approach based on the analysis of the influence of the induction of the internal magnetic field in ferromagnets on the dynamics of magnetization is not used here. This requires additional research.

In [3], the main attention is paid to subharmonic low-frequency resonances. These modes are characteristic of electromagnetic oscillating circuits with conducting magnets. At the same time, the regimes of superharmonic ferroresonances and basic resonances of the audio frequency range have not been studied in detail. Such studies should be conducted using magnetic dielectrics.

For the analysis of ferroresonance processes in the power industry, new methods have been tested using wavelet transformations of signals [4] and registration of accompanying magnetostrictive acoustic emission [5]. However, in the cited works, little attention is paid to the cascade transport of disturbance energy, which can have unexpected consequences in a wide range of frequencies. Relevant studies can be conducted on the basis of Fourier analysis of magnetostrictive acoustic emission under ferroresonance modes.

Numerical-analytical and graph-analytical methods of calculation and prediction of emergency-dangerous ferroresonance modes in electrical networks with nonlinear inductances are considered, in particular, in [6, 7]. Calculations are based on the polynomial dependence of the magnetizing current on the flux linkage, or hysteresis curves of magnetization, which are characteristic of the standard operating modes of voltage transformers, power transformers, and other devices of real

industrial power networks. Such connection with in-kind data increases the practical value of the results of the cited works. Critically, one should note the a priori determination of the time forms of currents and voltages, usually expressed by harmonic and limited polyharmonic dependences. Meanwhile, under the real conditions of power grid operation, non-normative switching processes with a significantly non-harmonic form of disturbances initiate nonlinear ferroresonances, which have features of both forced and parametric oscillations. In this context, one should note the ability of open nonlinear systems for dynamic self-regulation of their parameters that is not a priori predictable – with the "goal" of the fastest energy pumping and winning in the competition of modes. This side of the problem of ferroresonance is not covered at all in the cited works, which focus mainly on the processes of electromagnetic energy dissipation.

To predict alternative (relative to the known) energy pumping channels of ferroresonances, it is worth investigating the dynamics of magnetization in the ferromagnet material under conditions of external electromagnetic influence. In power grids, the classical axial magnetization in magnetic conductors is implicitly postulated. However, this is not the only geometry of the internal magnetic field in the conditions of the already mentioned dynamic self-regulation of the system of spin magnetic moments in the surrounding field. This side of the problem, using the example of nanostructured systems, is highlighted in works on ultra-high-frequency ferromagnetic and ferrimagnetic resonance [8, 9], in which the precession of moments under conditions of a strong permanent magnetic field is analyzed. In the context of the results below, such a precession is only comparative in view of the significant difference in the spatial and temporal scales of the studied systems. One should note the possibility (in addition to precession) of reversal of the cooperative magnetic moment in an external field, as well as the division of the system of spin magnetic moments of a ferromagnet into subsystems whose moments are mutually oriented in a certain way. Such processes in electrotechnical and radiotechnical nonlinear oscillating systems have been studied only within the framework of quasi-static magnetization curves, the parameters of which cannot be directly transferred to the self-organized dynamics of magnetic moments in an alternating electromagnetic field. In electric power systems using conductive ferromagnets, the magnetic induction rotor in the core material is largely determined by the conduction current density, which provides damping

of magnetization turns at high frequencies. Therefore, the little-studied processes of reversal of magnetic moments in the surrounding field should be carried out using magnetic dielectrics, where the angular dependence of the induction is determined by the rotor magnetization and displacement currents in Maxwell's equations.

The specified dynamic self-regulation and self-organization of the system of spin magnetic moments of a ferromagnet in a relatively weak external field brings ferroresonance processes closer to self-oscillatory and self-wave processes. This prompts their consideration in electromechanical analogies with contact tribodynamics, in which the nonlinearity of the mechanical contact of deformable solid bodies causes complex coherent dynamics even in the simplest systems in terms of elemental composition [10]. Such analogies have deep historical roots, formalized in the Lagrange-Maxwell equations, applicable directly to linear systems. Their indirect application to nonlinear ferromagnetic and tribodynamic systems can be carried out with the introduction of conditionally equivalent parameters. However, the internal ideology of Lagrangian mechanics regarding the exclusion of reactions (bonds) makes such an approach auxiliary and illustrative since the main problem lies precisely in nonlinear contact reactions and ferromagnetic elements. Appropriate use of quasi-static hysteresis curves does not make it possible to solve it fully [10, 11]. Therefore, the main way is the experimental study of this kind of systems and the construction of mathematical models based on the results of measurements.

In the end, it is necessary to especially note the thermodynamic disequilibrium of the studied systems and the possibility of their collector directing to unstable equilibrium states, rather than dissipative relaxation to stable equilibrium. This side of the problem is not reflected at all in previous studies of ferroresonance and requires special attention. Thus, for a comprehensive solution to the problem of ferroresonance and supplementing data on conducting ferromagnets in power systems, experimental studies of ferroresonance modes should be conducted. To this end, it is necessary to use magnetic dielectrics as part of the basic radio engineering RLC circuit. It is also necessary to reveal the peculiarities of such regimes with respect to self-oscillating and self-wave processes, dynamic self-regulation of the system of spin magnetic domains, and the collector increase of their energy, which may have emergency consequences.

3.1.2. The aim and objectives of the study, the study materials and methods

The purpose of our study is to establish the physical mechanisms of nonlinear tribodynamics of magnetization under ferroresonance modes of a parallel RLC circuit. This will make it possible to expand the possibilities of predicting emergency-dangerous ferroresonance modes in the power industry, as well as increase the reliability of using the phenomenon of ferromagnetic resonance in the field of thin magnetic films in radio electronics.

To achieve the goal, the following tasks were set:

– to carry out experimental measurements of resonant amplitude-frequency characteristics of an RLC circuit with a nonlinear ferromagnetic inductive element under the conditions of energy pumping by a source of alternating electric current;

– to register time forms of ferroresonance signals and forms of accompanying electromagnetic and acoustic magnetostrictive emission;

– to build a mathematical model describing the nonlinear dynamics of magnetization in the ferroresonance modes of a parallel RLC circuit;

– to reveal electromechanical analogies of the studied processes with collector resonance modes in nonlinear systems of contact tribodynamics.

The object of our research is a parallel RLC circuit with a nonlinear ferromagnetic (ferrimagnetic) core of an inductor, connected to a source of alternating electric current. The main research hypothesis assumes that the behavior of the system of spin magnetic moments of a ferromagnet in an external alternating electromagnetic field has signs of self-organization and dynamic self-regulation. Such behavior cannot be fully described using the existing quasi-static magnetization curves and requires an experimental study with appropriate analysis of the results.

In the paper, assumptions are adopted regarding the collector nonequilibrium nature of ferroresonance modes (contrary to the currently dominant quasi-static dissipative models), as well as regarding electromechanical analogies of the studied processes with nonlinear resonance modes of contact tribosystems.

In the process of analyzing the results, simplified linearized models of nonlinear resonant modes are used involving the corresponding conditionally equivalent dynamic parameters. In the scheme of the

experimental circuit (Fig. 3.1), a capacitor of constant capacity (1 μF or 2 μF) and a non-ideal (internal resistance of 17 Ohm) non-linear inductance coil were used.

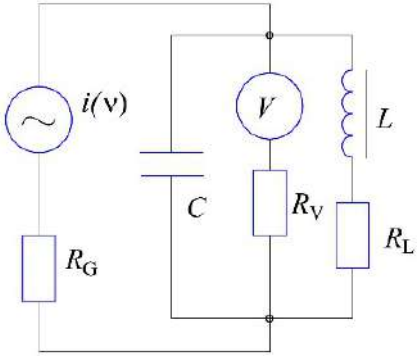

Fig. 3.1. Electrical diagram of an experimental RLC circuit

The elements were connected according to the parallel circuit to an external alternating current generator of the audio frequency range, the type of FG-200 ASICO (India). The advantage of this generator is the high stability of the output signal and the ability to adjust the internal resistance. The latter (5 kΩ) exceeded all characteristic resistances in the external circuit by at least an order of magnitude, which ensured operation under the current generator mode.

The alternating voltage on the capacitor and inductance was measured by the digital voltmeter B7-16A, and the waveform was recorded by the oscilloscope OWON XDS2102A (China). The internal resistances of the voltmeter and oscilloscope (~1 MΩ) significantly exceeded all resistances in the system, which excluded their influence on the measurement results. The electrical capacity of the connecting cables, oscilloscope, and voltmeter was several orders of magnitude smaller than the capacity of the capacitor, which also excluded the corresponding uncontrolled nonlinearity factors.

Two inductors with different magneto-dielectric cores were used to study the influence of the magnetization saturation factor on the nature of oscillations. The toroid coil had a core made of sendust (85 % Fe, 9.5 % Si, 5.5 % Al) composite material with a relatively high saturation inductance (about 1.0 T).

The solenoid coil was used with a MnZn-ferrite core, which was characterized by a relatively low saturation magnetization (about 0.3 T). The inductances of the coils and the capacities of the capacitors were selected in such a way as to ensure close values of the resonance frequencies at the limit of small excitations. To study the influence of the dissipation factor on the nature of oscillations, a cartridge of additional resistances was connected in series with the coil (Fig. 3.1).

To analyze electromagnetic wave losses under resonance modes, electromagnetic wave detectors (remote inductors) connected to an oscilloscope were brought to the inductor coils at a distance of several centimeters. In parallel with this, acoustic emission analysis of magnetostriction signals during remagnetization of a ferromagnet was also carried out. The Audacity software package was used for recording and spectral analysis of acoustic signals.

3.1.3. Results of investigating the nonlinear dynamics of magnetization under the ferroresonance modes of a parallel RLC circuit

Fig. 3.2 shows two families of resonance curves, obtained in the process of increasing the output power of the current generator, for each of the coils – with relatively large and relatively small non-linearity of the core material.

Unstable resonance modes, the transition through which had a jump-like character, are marked here with a dotted line. The high-frequency limit of the resonance curves was determined by the need to assign the main resonant mode, and the upper limit of the voltages was determined by the generator power limit.

Fig. 3.3 shows oscillograms of voltage signals on parallel sections of the circuit under the pre-resonance mode (~100 Hz), under the superharmonic resonance mode (~300 Hz), and under the basic resonance mode (~800–1000 Hz).

For comparison, Fig. 3.4 shows oscillograms of emission of electromagnetic waves under the same modes.

Fig. 3.5 shows a typical spectrum of magnetostrictive acoustic emission from a coil with a ferrite core under the basic resonance mode.

Acoustic magnetostrictive emission from a coil with a composite magneto-dielectric core was audible only under the marginal amplitude resonance modes but was too weak for reliable technical registration and further analysis.

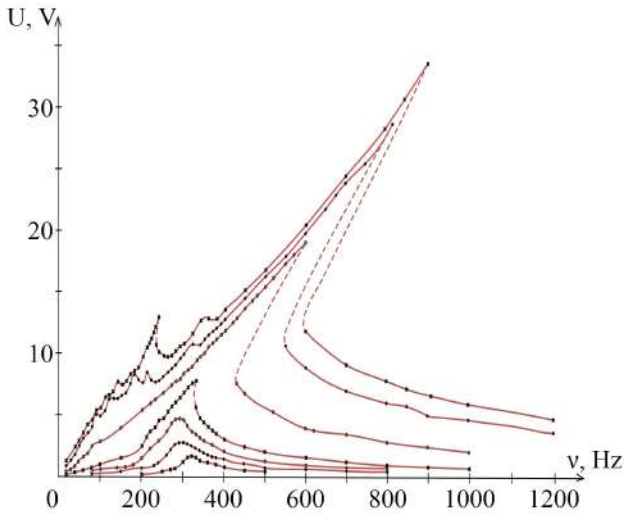

a

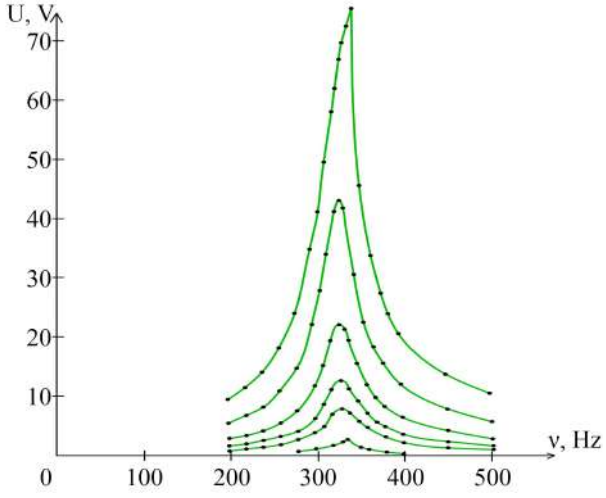

b

Fig. 3.2. Amplitude-frequency characteristics of ferroresonance oscillations in the circuits of the inductor: *a*) with a ferrite core; *b*) with a composite core

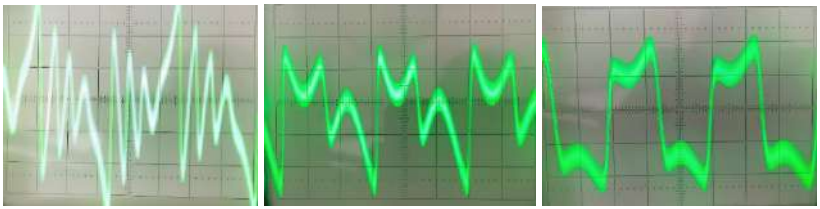

a *b* *c*

Fig. 3.3. Oscillograms of voltage signals on parallel sections of the circuit:
***a*) under the pre-resonance mode;**
***b*) under the mode of superharmonic resonance;**
***c*) under the basic resonance mode**

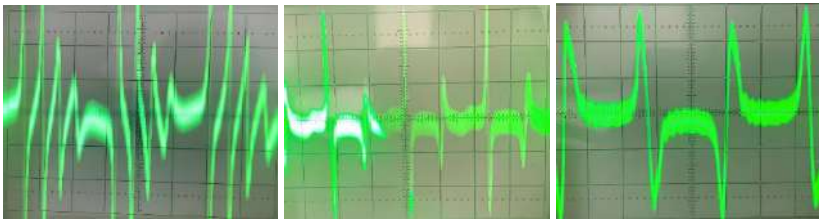

a *b* *c*

Fig. 3.4. Oscillograms of electromagnetic emission signals from the inductor coil: *a*) under the pre-resonance mode;
***b*) under the mode of superharmonic resonance;**
***c*) under the basic resonance mode**

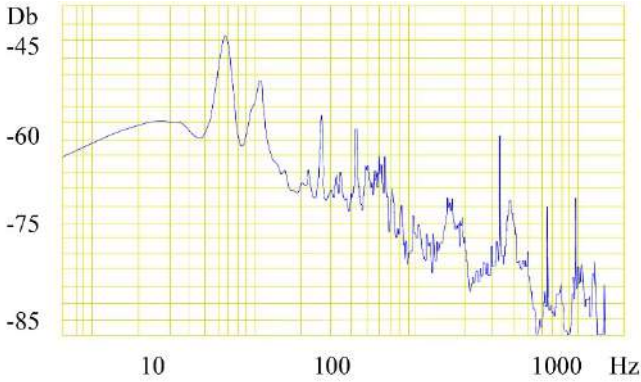

Fig. 3.5. Typical spectrum of magnetostrictive acoustic emission from a coil with a ferrite core under the basic resonance mode

3.1.4. Mathematical model of nonlinear dynamics of magnetization under ferroresonance modes of a parallel RLC circuit

When constructing a mathematical model, the following features of the above experimental results should be taken into account. As can be seen from Fig. 3.2, the nature of the resonance curves significantly depends on the degree of nonlinearity, which is determined by the saturation limit of the ferromagnet. A characteristic feature of nonlinear modes is the direct slope of the frequency-dependent amplitude in the pre-resonance sections. For a weakly nonlinear composite ferromagnet, this kind of dependence is observed only at extremely high (for the used generator) excitation levels. Resonance characteristics have a mixed form of their skeletal curves, which qualitatively correlates with the quasi-static magnetization curve of a ferromagnet (Fig. 3.6) – with a transition from the initial nonlinear-soft to the next nonlinear-hard characteristic.

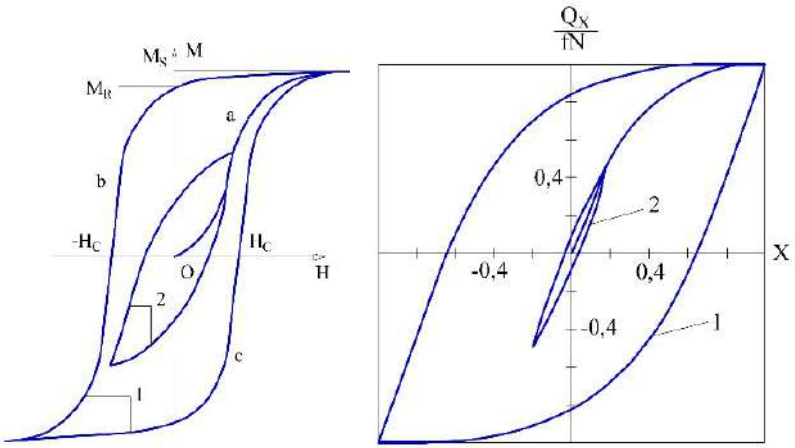

a *b*

Fig. 3.6. Curves of quasi-static hysteresis: *a*) magnetic; *b*) contact

The time forms of voltage signals on circuit elements and electromagnetic emission signals have a quasi-harmonic form only for a weakly nonlinear ferromagnet. In the case of a ferrite core, the forms have a significantly different appearance (Fig. 3, 4).

We shall use the model method of electromechanical technologies in oscillating systems with variable parameters. When a capacitor with capacity C and a coil with inductance L are connected in parallel to an external alternating current circuit, we have the following analogies:

$$C \leftrightarrow m, \tag{3.1}$$

$$L^{-1} \leftrightarrow k, \tag{3.2}$$

$$\frac{di}{dt} \leftrightarrow Q(t), \tag{3.3}$$

where m, k, $Q(t)$ are the mass, stiffness coefficient, and forcing force in the equivalent mechanical system, respectively. Under the condition of small dissipative losses, the resonant frequency is written here in a known way:

$$\omega_r^2 = \left(2\pi\nu_r\right)^2 \approx \frac{k}{m} = \frac{1}{LC}. \tag{3.4}$$

In such a model, the analog of the mechanical displacement X is the voltage U on the capacitor and the inductor. Under resonant modes, the current I through the coil significantly exceeds the current in the external power supply circuit as well (with a high Q-factor of the oscillating circuit). Under the conditions of resonant compensation of reactive resistances, we use the following ratio:

$$U_r = I_r R_L, \tag{3.5}$$

where U_r is the resonant voltage measured by a voltmeter, R_L is the total active resistance of the section with the inductor. Considering the inductance L as the proportionality factor between the magnetic flux coupling Ψ and the current strength I, we write Faraday's law in a system with a nonlinear inductance depending on the current strength and, accordingly, on time t:

$$\varepsilon_S = -\frac{d\left(LI\right)}{dt} = -\left(L + I\frac{dL}{dI}\right)\frac{dI}{dt} = -\tilde{L}\frac{dI}{dt}, \tag{3.6}$$

where ε_S – e.r.s. of self-induction, $\tilde{L}$ – nonlinear inductance:

$$\tilde{L} = L + I\frac{dL}{dI}. \tag{3.7}$$

As can be seen, at negative and sufficiently large values of the derivative in (3.7), the nonlinear inductance $\tilde{L}$ becomes negative, which leads to a negative value of the square of the resonance frequency:

$$\omega_r^2 \approx \frac{1}{\tilde{L}C} \le 0. \tag{3.8}$$

In electromechanical analogies, regimes of this kind correspond to the dynamics of an inverted pendulum near an unstable upper equilibrium position. The forms of oscillations in this case are essentially non-harmonic – they are stitched together from areas of exponential growth and decrease of voltage, which is clearly shown in Fig. 3.3, as well as on the corresponding oscillograms of electromagnetic emission from the coil (Fig. 3.4). The spectrum of magnetostrictive acoustic emission (Fig.3. 5) contains two clusters – low-frequency and high-frequency, corresponding to the slow movement of the conditional pendulum near the upper point of unstable equilibrium and the abrupt passage of the lower equilibrium point with the loss of part of the stored energy.

Equation (3.7) can be integrated under the condition of transition to the self-oscillating mode with reversal of the magnetic moment of the spin domains in the given magnetic field:

$$\tilde{L} = L + I\frac{dL}{dI} = -L, \tag{3.9}$$

$$L = \frac{K}{I^2}, \tag{3.10}$$

where K is a dimensional constant. Expression (3.9) in its physical meaning reflects dynamic antiferromagnetism – self-organized orientation of the system of spin magnetic moments in the direction opposite to the external magnetic field. This orientation corresponds to the non-equilibrium maximum (rather than the usual equilibrium minimum) of the magnetic moments in the external field. Under such conditions, as can be seen from (3.10), the inductance of the coil decreases inversely quadratically with respect to the current, which

becomes possible with the transition to the magnetic saturation mode with the subsequent reversal of the magnetic moment.

Substitution (3.9), (3.10) in (3.8), taking into account (3.5), gives:

$$\omega_r^2 \approx -\frac{I_r^2}{KC} = -\frac{U_r^2}{R_L^2 KC}, \tag{3.11}$$

which reflects the direct proportionality of the resonance frequency and voltage under such modes, corresponding to the experimental data (Fig. 3.2).

According to experimental data (Fig. 3.2) and expression (3.8), the inductance is directly proportional to the magnetic permeability of the core. In this way, the formal dependence of nonlinear magnetic permeability $\tilde{\mu}$ (in relative terms) on resonant frequency, voltage, and current can be established:

$$\left|\frac{\tilde{\mu}}{\tilde{\mu}_0}\right| = \left|\left(\frac{\omega_r^0}{\omega_r}\right)^2\right|, \tag{3.12}$$

where $\tilde{\mu}$ is the magnetic permeability at the limit of weak excitations, ϖ_r^0 is the cyclic resonance frequency at this limit.

Fig. 3.7 shows this kind of dependence in terms of the current corresponding to the active resistance R_L.

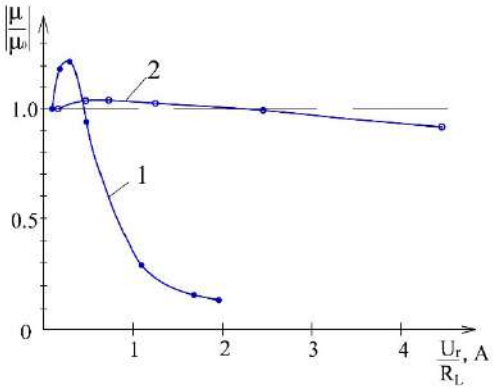

Fig. 3.7. Calculated dependences of the reduced magnetic permeability on the current in the coils: *1* – ferrite core; *2* – composite magnetoelectric core

Qualitatively, the dependence $\tilde{\mu}(I)$ corresponds to a quasi-static loop of ferromagnetic hysteresis (Fig. 3.6). The descending part of this dependence agrees with (3.10) (in the case of a ferrite core) at the initial stage, but at higher excitation levels it is quantitatively approximated by an expression different from (3.10):

$$L = \frac{D}{I^{1.2}}, \tag{3.13}$$

$$\tilde{L} = -0.2L, \tag{3.14}$$

where D is the dimensional factor. This indicates the need to take into account dissipation processes in the dynamics of magnetization reversal.

These processes can be analyzed based on the known ratios regarding the Q-factor of the oscillating circuit:

$$Q = \frac{\nu_r}{\Delta\nu_{0.7}} \frac{\sqrt{\frac{L}{C}}}{R_L} = \frac{1}{\varpi_r \cdot C \cdot R_L}, \tag{3.15}$$

where ν_r, $\Delta\nu_{0.7}$, ω_r are the resonance frequency and standard frequency width of the maximum, as well as its cyclic resonance frequency.

It is advisable to supplement the above calculations with a description of the dynamics of magnetization in ferromagnets based on Maxwell's equations (SGS system):

$$rot\vec{E} = -\frac{1}{c}\frac{\partial\vec{B}}{\partial t}, \tag{3.16}$$

$$\vec{\nabla}\vec{B} = 0, \tag{3.17}$$

$$rot\vec{B} = \frac{4\pi}{c}\left(\vec{j} + c \cdot rot\vec{M}\right) + \frac{1}{c}\frac{\partial\vec{D}}{\partial t}, \tag{3.18}$$

$$\vec{\nabla}\vec{D} = 4\pi\rho, \tag{3.19}$$

where $\vec{E}$, $\vec{D}$, $\vec{B}$ is the intensity and induction of the electric field, as well as the induction of the magnetic field, respectively, $\vec{M}$ is

the magnetization of the core material, $\vec{j}$, ρ is the conduction current density and the volume density of extraneous electric charges in this material, *c* is the speed of light in a vacuum, *t* is time.

The material relations for closing the system (3.16) to (3.19) take the form:

$$\vec{D} = \vec{E} + 4\pi\vec{P}\left(\vec{E}\right), \tag{3.20}$$

$$\vec{H} = \vec{B} - 4\pi\vec{M}\left(\vec{B}\right), \tag{3.21}$$

where $\vec{P}$ is the electrical polarization of the medium, $\vec{H}$ is the intensity of the magnetic field in it. For the magnetic dielectrics studied here, the conduction current $\vec{j}$ in (3.18) can be neglected, and therefore the magnetic induction rotor is determined by the magnetic current density:

$$\vec{j_M} = c \cdot rot\vec{M}\left(\vec{B}\right), \tag{3.22}$$

which directly reflects the rotations of the saturated magnetization of the ferromagnet not in the external field $\vec{H}$, but in the internal field $\vec{B}$. This form of description allows us to explain (at least on a qualitative level) the observed dynamics of magnetization under the non-equilibrium mode.

3.1.5. Results of registration of collector modes of motion in analog systems of nonlinear contact tribodynamics

Manifold modes of motion in analog tribocontact systems have already been demonstrated on the example of a simple auto-oscillating contact mechanical system in the form of a ring, or a disk, launched from the edge of the base plane under the mode of rotation and rotation with rolling. Fig. 8 shows acoustograms of this kind of processes, and Fig. 3.9 – a typical spectrum of accompanying acoustic emission.

As can be seen, the movement of the rotor has a buffeting quasi-periodic character (in the absence of external cyclic excitation in this case), and the acoustic emission spectra, as in Fig. 3.5, contain two clusters. These results reflect the already mentioned mode of oscillation

of a conventional inverted pendulum aimed at the maximum (and not at the minimum) of its energy in an external field – in this case, a gravitational field.

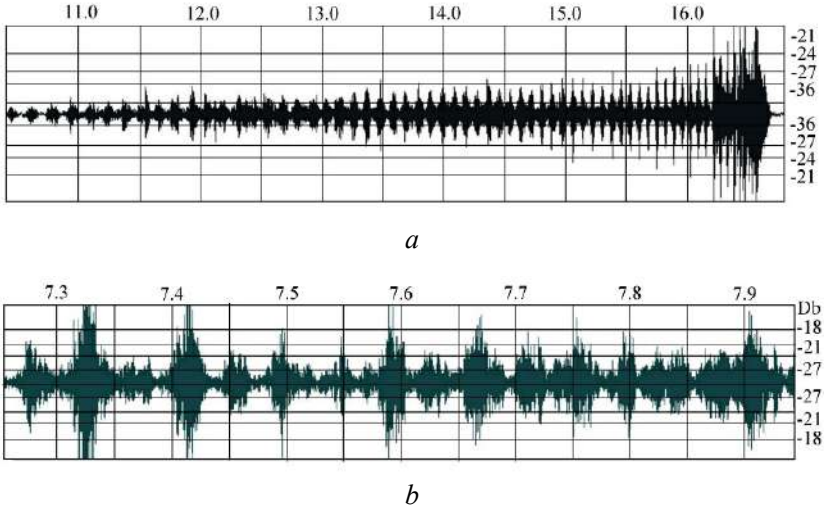

Fig.3. 8. Acoustograms of motion along the plane of the base under the rotation-roll mode: *a*) metal ring; *b*) mirror disk

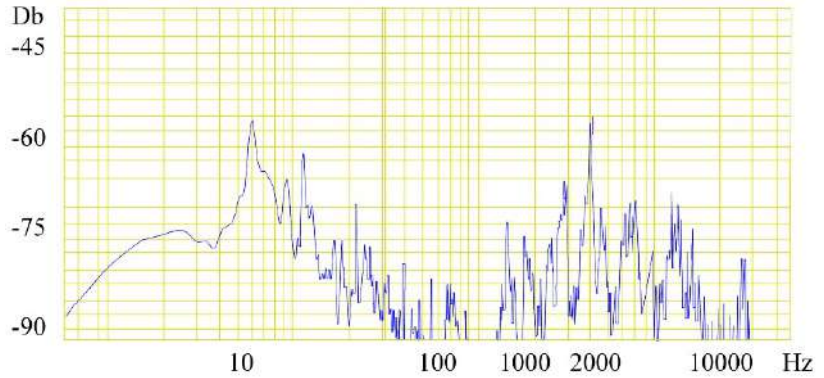

Fig. 3.9. The spectrum of the acoustic emission accompanying the movement of the mirror disk along the plane of the base

3.1.6. Discussion of results of investigating the nonlinear dynamics of magnetization under the ferroresonance modes of a parallel RLC circuit

A comparison of resonant amplitude-frequency characteristics (Fig. 3.2) and the results of model calculations (Fig. 3.7) confirms the leading role of magnetization saturation of the ferromagnet in the mechanisms of the transition to the nonlinear resonance regime. After all, a significant non-linearity of the rigid type in the characteristics (for ferrite cores) is observed directly at the calculated maximum for the relative magnetic permeability of the core. The transition through this maximum is accompanied by dynamic self-regulation of magnetization in the internal magnetic field. A feature of such a transition, which was not noted in other works on this topic, is a cyclic reversal of the collective magnetic moment in the surrounding field in the direction of an unstable state of equilibrium corresponding to a maximum (rather than a stable minimum) of energy. This is evidenced by the forms of electromagnetic emission from the core of the inductor, shown in Fig. 3.4.

They have a significantly non-harmonic appearance and contain relaxation time segments in the direction of an unstable state of equilibrium. Inevitable and stimulated by variable external influence, the loss of such equilibrium generates pulsating induced currents in the oscillating circuit, the shape of which is significantly non-harmonic. At the same time, there remains the possibility of generating also traditional quasi-equilibrium modes imitating the temporal harmonic form of the excitation. Under the pre-resonance modes, the latter are suppressed by the high reactance of the circuit, however, superharmonic and fundamental resonance modes are characterized by self-synchronization of frequencies and nonlinear mixing of both modes. Such mixing in combination with the nonlinear transport of disturbance energy should be taken into account when designing and operating radio and electrical systems with nonlinear inductances.

The nature of dynamic self-regulation of magnetization under resonant modes depends significantly on the domain structure of the ferromagnet and the induction of its saturation, which directly follows from the comparison of ferrite and composite magnetic dielectrics – Fig. 3.2, 3.7. The damping properties of the latter, meanwhile, are insufficient to suppress resonant peaks. At the same time, an increase in

the active resistance R_L already by several Ohms under resonant modes led to the breakdown of resonant maxima and jumps to low-amplitude resonant sections of the amplitude-frequency characteristics (for ferrites).

Therefore, increasing the active resistance remains a simple and effective method of combating unwanted resonance modes: linear or non-linear. In this context, it is worth analyzing the Q-factor of this oscillating circuit under different modes. It is usually estimated by the relative width of resonance maxima according to (3.15). However, this expression does not take into account a certain degree of coherence of the system of magnetic spin domains, which noticeably narrows the resonance lines towards saturation (Fig. 3.2).

A similar narrowing of resonance lines is also observed in coherent systems of contact tribodynamics. At the same time, the nonlinearity of the system serves as an additional factor of restraining resonant amplitudes, but it leads to the cascade transport of energy by the spectrum of disturbances [10, 11]. This factor is of particular importance in terms of projecting the results obtained above (for magnetic dielectrics) to electrotechnical ferroresonance processes in magnetic conductors. In particular, low-frequency subharmonic resonances [3] can be excited by such transport from the side of uncontrolled high-frequency switching processes. Continuing the line of electromechanical analogies, a comparison of ferromagnetic and contact hysteresis curves should be made (Fig. 3.6). Here, worth noting is a significant difference (the opposite result of the effect of nonlinear saturation in ferromagnetic systems and dry friction systems) taking into account that the equivalent mechanical stiffness, as already noted, is inversely and not directly proportional to the inductance.

This predetermines the rigid character of nonlinearity in electromagnetic systems (with strong excitation (Fig. 3.2) and the soft character during tangential loading of mechanical contact [11, 12]. However, taking into account the normal components of contact reactions radically changes the situation, determining the mixed and rigid character of nonlinearities, similar to the results shown above [10].

The limitations of this work are the use of only magnetic dielectrics under ferroresonance modes, without researching the corresponding processes in magnetic conductors. In this connection, one should note the special role of the possible precession of magnetization in the internal magnetic field in the formation of low-frequency subharmonic ferroresonances, noted, for example, in [3]. This requires

additional research because the currently available results from ferroresonance do not take into account the precession factor. On the other hand, the precession factor is considered to be the main factor in the ultra-high-frequency excitation of ferromagnetic and ferrimagnetic resonances in magnetic nanotechnologies using a permanent external magnetic field [8, 9].

In this field, in addition (before precession), one should take into account the possibility of self-wave reversal of the collective magnetic moment in the internal field of the environment, and not only in the external magnetic field. This will make it possible to separate the interfering collective effects and increase the reliability of the technological application of ferromagnetic resonance.

The disadvantage of our study is the use of purely laboratory equipment for the analysis of ferroresonance processes. In the future, this shortcoming can be eliminated via scientific cooperation with domestic and foreign specialists in the operation of industrial power networks, in which the problem of preventing emergency-dangerous ferroresonance modes is being solved. Advancing our research may involve the construction of a more specific and adapted to practice mathematical model for describing the precession and reversal of magnetization of a ferromagnet in the surrounding field, based on Maxwell's equations. Difficulties of a mathematical and methodical nature on this path are the need to reformat the material relations necessary to close the system of Maxwell's equations. These ratios must be derived from the induction of the internal magnetic field, and the dominant methods of describing ferroresonance processes directly or indirectly derive from the intensity of the external magnetic field.

Conclusions

1. It was established that the physical mechanism of dynamic self-regulation of the system of spin magnetic moments of magnetic dielectrics in the ferroresonance regimes of a parallel oscillating circuit is a cyclic reversal of the magnetic moment in the induced electromagnetic field. This mechanism is mathematically described in terms of the magnetic current density and the corresponding magnetization rotor in Maxwell's equations. At a qualitative level, it can be described through the introduction of a nonlinear inductance depending on the current strength. The main factor of this kind of self-regulation is the direction of the system of spin magnetic moments to an unstable state of equilibrium

corresponding to the maximum (rather than the classical minimum) of energy in the external field.

Cyclic loss of such equilibrium generates pulsating induced currents, which are not taken into account by traditional methods for calculating ferroresonance modes.

2. Our experimental studies revealed frequency self-synchronization and nonlinear mixing of two types of modes under ferroresonance conditions. Namely: the quasi-static mode, which imitates the time form of the external excitation of oscillations, and the dynamic mode, which corresponds to the unstable state of equilibrium of the magnetic moments. These processes lead to the cascade transport of energy by the spectrum of disturbances and determine the adaptability of disturbances to the external conditions of energy pumping. They should be taken into account when projecting the obtained results to electrotechnical ferroresonance processes in magnetic conductors, in which the cascade energy transfer of uncontrolled high-frequency switching biases initiates low-frequency subharmonic ferroresonances. Increasing the ohmic losses in the oscillating circuit remains a simple but effective method for suppressing unwanted ferroresonance modes. At the same time, one should take into account the effects of mode competition, which give preference to low-frequency modes with small losses for the dissipation of eddy current energy.

3. The mechanism of reversal of the collective magnetic moment in the internal field is mathematically described through the magnetic current density and the corresponding magnetization rotor in Maxwell's equations. At a qualitative level, it can be described through the introduction of a nonlinear inductance depending on the current strength. However, the last form of description, like the traditional methods in this field, is based on the given intensity of the external magnetic field and does not sufficiently take into account the existing factor of self-regulation of magnetization in the internal field of the environment.

4. It is advisable to conduct the analysis of ferroresonance processes in electromechanical analogies with nonlinear contact tribodynamics in the context of thermodynamic disequilibrium of such systems. This analysis reveals, in particular, coherent narrowing of resonance lines and non-equilibrium forms of self-oscillations that have a common time form in electromagnetic and mechanical contact systems.

3.2. Modeling of contact interaction and wear of the trolleybus contact insert-wire tribopair

3.2.1. Analysis of wear resistance problems of conductive elements of transport vehicles

Wear of contact elements of electric transport, in particular contact inserts of trolleybus pantographs, remains one of the main reasons for the decrease in reliability and increase in operating costs of urban transport. During the movement of the trolleybus, the insert is constantly in contact with the wire network, which leads to intensive abrasive and adhesive wear. Change in the insert profile, loss of contact surface geometry and increase in sliding resistance reduce the quality of current collection, cause electrical sparks and deterioration of the operation of electrical equipment.

Traditionally, wear resistance assessment has been performed experimentally in laboratory or field conditions, but such methods are laborious, expensive and do not always allow to take into account the complex variability of operating modes characteristic of real conditions. Therefore, it is relevant to introduce numerical analysis tools, in particular the finite element method (FEM), which allow to model not only the mechanical interaction, but also the processes that directly affect wear, such as contact pressure, friction, local stresses, the shape of the contact spot and the geometry of the elements.

Of particular interest is the possibility of quantitative assessment of linear wear based on the distribution of frictional stresses obtained in Ansys, with the subsequent application of energy approaches to the calculation. This approach allows not only to take into account local friction characteristics, but also to predict the service life of the insert depending on the length of the run and the modes of movement of the trolleybus. This opens up prospects for integrating numerical modeling into regulatory procedures for assessing the wear resistance of current-collecting components and unifying approaches to their constructive optimization.

The problem of wear of tribosystem elements is key in transport engineering, in particular for current-collecting pairs of electric transport. A systematic study of wear mechanisms is given in the work P. Blau [13], where transient friction modes and the influence of loading conditions on the nature of wear of materials are considered. G. Stachowiak and A.

Batchelor [14] in their fundamental monograph classify in detail the types of wear – adhesive, abrasive, fretting, etc. — and consider mathematical models that describe the dependence of wear on contact pressure, sliding velocity and material properties.

Particular attention in the study of wear is paid to energy criteria. Meng and Ludema [15] summarized the main approaches to building wear models and emphasized their limitations under conditions of variable loading and unsteady contact. Their analysis of the forms and content of predictive equations highlights the need to use models that take into account local contact parameters. At the same time, modern software environments, as shown in [16], allow the use of these equations based on numerical modeling data – in particular, friction stresses and contact pressure.

Han et al. [17] presented a numerical analysis of a wear-sensitive contact problem using a fully discrete scheme to model an elastic body under friction and wear conditions. Their results demonstrate the effectiveness of the approach in predicting the evolution of the contact surface. Ravitej and Kumar [18] conducted a comparative study on the prediction of wear rate of hybrid composites by combining experimental analysis, finite element modeling, and machine learning, which allowed to improve the accuracy of predictions.

Ansys Inc. [19] provided an example of modeling the wear of a contact surface using the Archard wear model, demonstrating the process of sliding a hemispherical ring on a flat ring and evaluating the strains and normal stresses before and after wear. Lopez [20] provided an overview of contact modeling methods in Ansys Mechanical, including different contact types such as bonded, non-separated, frictionless, and rough, and discussed the contact algorithms used in Ansys to accurately model surface interactions.

Thus, modern literature confirms the effectiveness of combining classical energy models with numerical FEA data for wear analysis in tribopairs, which is a relevant and promising approach for modeling the insert and contact wire of a trolleybus.

3.2.2. Modeling of the stress state and contact loads in the tribocouple "contact insert-electrical wire"

Based on the working drawings, the following solid models were created: contact insert (Fig. 3.10) and cross-section of the MF-100 contact wire (Fig. 3.11).

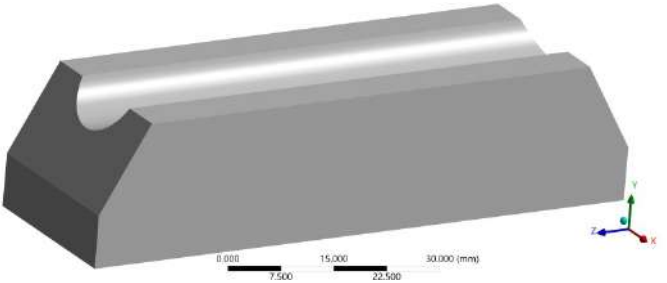

Fig. 3.10. Solid model of a trolleybus contact insert

The models were created in SolidWorks with working dimensions. The body length is 300 mm (solid model extrusion).

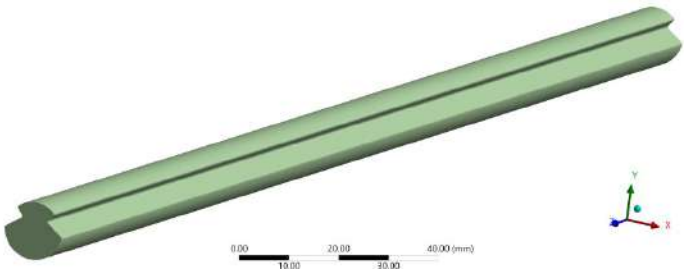

Fig. 3.11. Solid model of the contact wire

Based on the solid-state models of the insert and the contact wire, a finite element FEA mesh was built in the Ansys environment. The FEA mesh parameters are as follows: Body Sizing = 2.0 mm – the maximum size of the finite elements of the model bodies; Face Sizing = 1.0 mm – the size of the finite elements on the contact surfaces of the bodies; Inflaction = 9 for the wire and 12 for the insert. The parameters also determine the number of layers of finite elements with the size Face Sizing deep into the wire body and insert.

Body materials. From the available Granta EduPack library, the only possible materials that are close to the target ones were selected: Carbon (CY) for the insert; Cooper C10100 for the wire. The mesh view is presented in Fig. 3.12.

To simulate the contact conditions for this pair, a frictional contact mode Frictional with a friction coefficient of 0.13 was specified (Fig. 3.13).

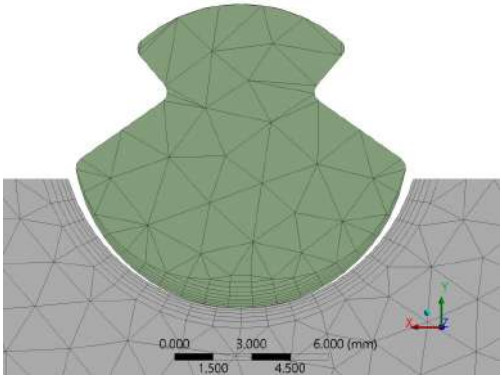

Fig. 3.12. FEA mesh of the contact model of the trolleybus and contact wire insert

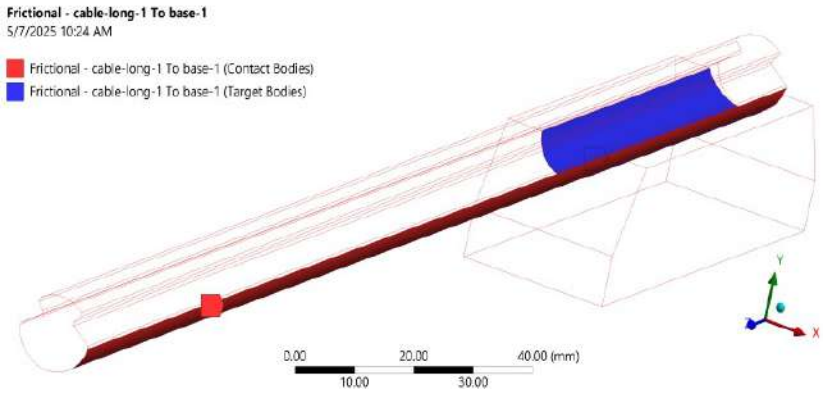

Fig. 3.13. Frictional contact in the insert-wire pair

To simulate contact pressure from the insert side, a uniformly distributed force of 0.5 MPa was applied to the wire perpendicular to the lower surface of the insert (Fig. 3.14).

A steady state loading regime of 0.5 MPa was analyzed. The insert was displaced 200 mm along Z in both L- and S-modes.

The equivalent Mises stresses for the insert and wire are shown in Fig. 3.15–3.16, respectively. For the insertmaximum stresses σ are observedmax = 16.236 MPa at the moment of time t =2.e-002 s; for wire σ_{max} = 14.33 MPa at time t = 0.12 s.

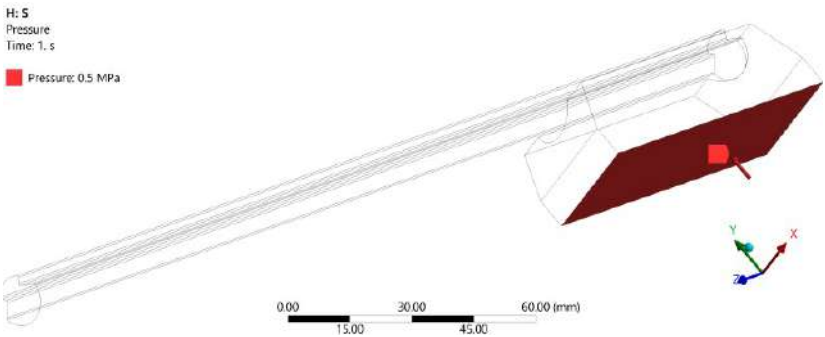

Fig. 3.14. Modeling the load on the contact pair

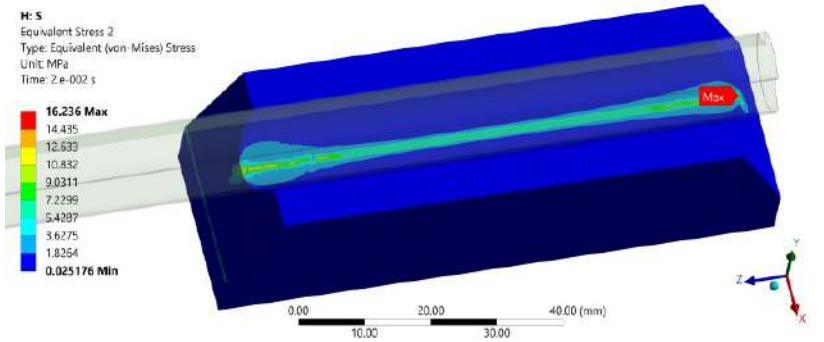

Fig. 3.15. Equivalent Mises stresses for the insert

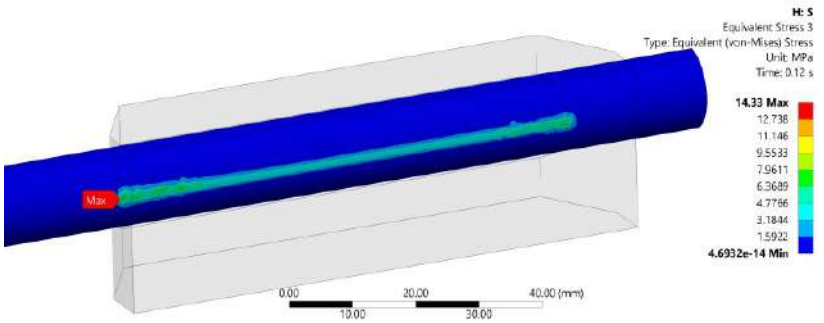

Fig. 3.16. Equivalent Mises stresses for a wire

Next, the characteristics of the dimensions of the contact zone (Contact Tool) were determined. A slip spot was recorded in the contact area, further from it the nature of the contact changes to a transitional one, and at the edges – to a gap (Fig. 3.17).

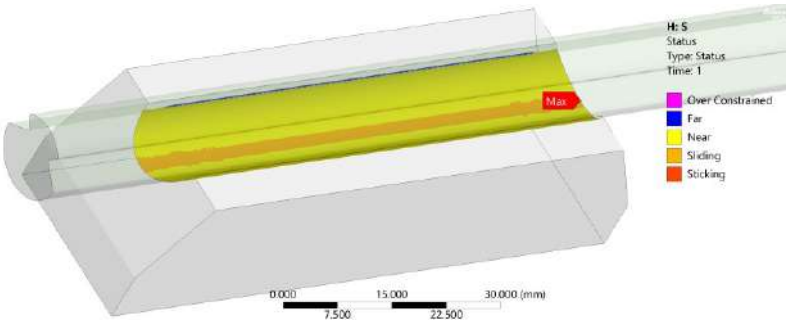

Fig. 3.17. Qualitative characteristic of the contact mode of the insert and wire

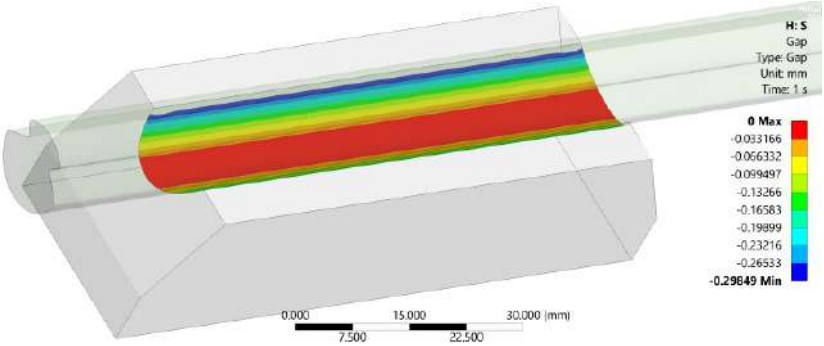

Fig. 3.18. The value of the contact gap between the insert and the wire

The contact gap varies from 0 to 0.29849 mm (Fig. 3.18). The maximum penetration is 0.0035762 mm at $t = 0.42$ s.

The maximum pressure in the contact area is 23.951 MPa at $t = 0.42$ s. The maximum average pressure value is 1.063 MPa at $t = 0.12$ s. The fluctuations of the average pressure are shown in the graph (Fig. 3.19).

Frictional stresses were used to calculate the wear characteristics in the insert-contact wire pair. Accordingly, the values of frictional

stresses were further determined using the Ansys application package (Fig. 3.20).

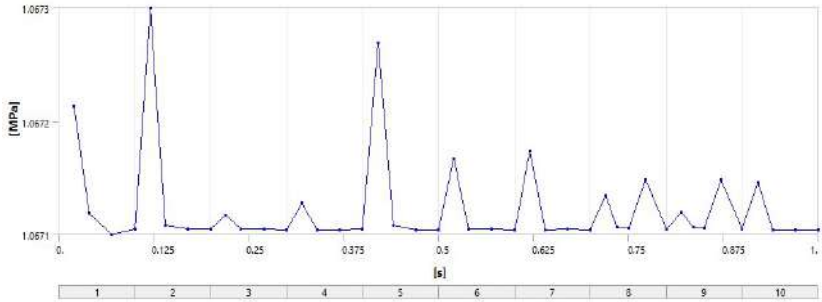

Fig. 3.19. Fluctuations in average pressure

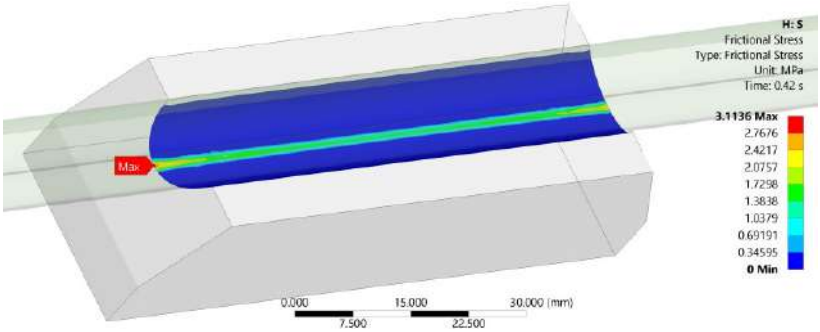

Fig. 3.20. Map of friction stresses on the surface of the contact insert

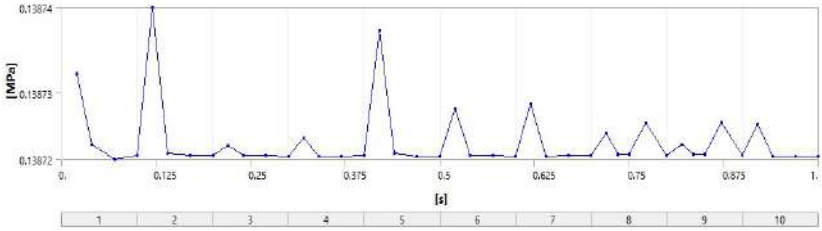

Fig. 3.21. Fluctuations of average friction stresses on the surface of the contact insert

The maximum frictional stresses were σ_{max} = 3.1136 MPa at time t = 0.42 s. The maximum value of the average frictional stress is σ_{max} = 0.13874 MPa at t = 0.12 s. The fluctuations of the average frictional stress are shown in Fig. 3.21.

3.2.3. Calculation of contact insert wear using the energy model

According to the energy approach, wear is the result of the expenditure of part of the mechanical friction energy on plastic deformation and detachment of particles from the contact surface.

The general equation:

$$V = \alpha \cdot E_{frict} = \alpha \cdot \int p \cdot \Delta u dA, \tag{3.23}$$

where α is the global efficiency coefficient of energy conversion into wear, mm³/J; E_{frict} is the friction energy (total or local), N m or J; p is the contact pressure or normal force per area, Pa; Δu is the relative shear displacement, m; dA is the contact area element, m².

Simplified local formula for linear wear:

$$d(x, y) = \frac{\eta \cdot \tau \cdot (x, y) \cdot s(x, y)}{H}, \tag{3.24}$$

where $d(x, y)$ is the local wear depth, mm; η is the local efficiency coefficient of energy conversion into wear (≈ 0.01–0.1); τ is the tangential stress, Pa; s is the sliding distance, m; H is the material hardness, Pa.

Physical content: ($\tau \cdot s$) is the friction work per unit area, J/m²); $\eta \cdot \tau \cdot s$ is the energy effectively spent on wear and tear (losses); H is the normalization of this energy due to the resistance of the material (the higher the hardness, the less wear).

Format for manual calculation:

$$d = \frac{\eta \cdot \tau_{avq} \cdot s_{total}}{H}, \tag{3.25}$$

where τ_{avq} is the average frictional stress value from Ansys, Pa; s_{total} is the total sliding distance, m . According to FEA tests = 0.13873 MPa

for the entire surface, and the max value is 3.1136 MPa. However, we will be interested only in the central part, where the permanent contact is fixed – the red area with a gap value of 0 mm (Fig. 3.18). The approximate value in the red area is 0.4 MPa. For the hardness of the insert material HRB = 50–75, the value varies between $H = 3.45 \cdot 50 = 172,5$ MPa and $H = 3.45 \cdot 75 = 258,75$ MPa. We take the average value $2.15 \cdot 10^8$ Pas. We consolidate the boundary conditions: $\tau_{avq} = 0.4$ MPa; $s_{total} = 0.2$ m; $H = 2.15 \cdot 10^8$ Pa; Mileage = 100 km.

Wear per 1 sliding cycle (0.2 m):

$$d = \frac{\eta \cdot \tau_{avq} \cdot s_{total}}{H} = \eta \cdot \frac{0.4 \cdot 10^6 \cdot 0,2}{2.15 \cdot 10^8} = \eta \cdot 0.37209 \text{ mm}. \quad (3.26)$$

Number of cycles per 100 km: 100,000/0.2=500,000 cycles.
Total wear:

$$d_{100km} = 0,37209 \cdot 500.000 \cdot \eta = 186.045 \cdot \eta \text{ mm}. \quad (3.27)$$

The result under the condition is: $\eta = 10^{-6}$ $d_{100km} = 0.186$ mm, which correlates with experimental data on wear "Performance characteristics of VKT-M inserts when working in conjunction with MF-100 copper wire": linear wear of inserts, mm/100 km of run is +(0.1…0.2) mm under dry sliding contact conditions. Given the value of $\eta = 10^{-5}$ $d_{100km} = 1.86$ mm.

Obviously, there is a question of interpolation of FEA test results and selection of a real value of the coefficient . Also, the question of the correspondence of the physical and mechanical properties of Granta EduPack materials in Ansys to real materials in operation. The subject of future research is interpolation of the insert loading modes: with constant and linearly increasing pressure. It can be assumed that when starting from stops, the pressure value changes (increases or decreases); under the conditions of linear movement of the trolleybus and a flat road surface, the pressure value can maintain a relatively constant value; in turns, the contact spot of the insert with the wire migrates to the inner sidewalls of the insert recess, so the wear area shifts, providing a greater overall resource. Interpolation of short FEA tests to long-term operating conditions requires the creation of a mathematical prediction model, which is an integral of various driving

modes during the trolleybus working shift. Undoubtedly, studying the totality of these factors can help actualize the meaning of wear and tear and bring it closer to real conditions η.

Conclusions

1. Numerical modeling of the contact interaction of the insert–wire tribopair was carried out, which allowed determining the stress-strain state and friction characteristics.

2. According to the results of FEA analysis, the values of stresses, pressures, and penetration in the contact zone were obtained, indicating the presence of a stable slip spot and a gap zone.

3. The application of the energy criterion allowed us to calculate the wear depth of the contact insert per cycle and per full mileage, which is consistent with experimental data.

4. It has been established that modeling in the Ansys environment provides a reliable assessment of wear conditions provided that the physical and mechanical parameters are correctly selected.

5. The need to develop a mathematical model for interpolation of short-term FEA tests for long-term operation, taking into account changes in load during trolleybus movement, is shown.

3.3. Probabilistic approach to assessing tribotechnical reliability indicators of friction units

3.3.1. Analysis of approaches to assessing the reliability of tribosystems

Ensuring the reliability of technical systems is one of the main tasks of modern mechanical engineering, in particular in conditions of intensive operation and high loads. Friction units are one of the most vulnerable parts of mechanisms, and their premature failure can cause significant economic losses or even accidents. The traditional approach to reliability assessment often ignores the stochastic features of the operation of tribotechnical elements, which leads to an underestimation of the accuracy of predictions.

Given that the wear process is complex, non-uniform and largely random, there is a need to switch to probabilistic analysis methods. This approach allows us to take into account not only the average values of loads and wear, but also their variations, dispersions

and other statistical characteristics. In particular, the use of probability density distribution functions allows us to estimate the probability of failure, construct reliability functions and optimize design parameters.

This article highlights the basic concepts and mathematical tools underlying the probabilistic approach to tribotechnical reliability. This research has practical implications for designers of mechanisms operating under conditions of significant and variable loads.

The aim of the work is to develop a probabilistic model for assessing the reliability of friction units taking into account the random nature of wear and load. To achieve the set goal of the research, the following tasks were solved: to build mathematical models of wear and load distribution; to determine distribution and density functions for key parameters; to propose a methodology for assessing reliability under constant and block loading; to calculate reliability based on statistical characteristics.

Tribological reliability issues in engineering have been widely discussed in the scientific literature. In [21], the main focus is on identifying failure modes and mechanisms. This is especially true for the emerging technology of microelectromechanical systems (MEMS). The focus here is on the mechanism of wear failure and how the methodology was used to create a predictive model.

The MEMS device that was emphasized in these studies was a Sandia-developed micromotor with orthogonal electrostatic linear actuators connected to a gear on a hub. The dominant failure mechanism was wear in the sliding/contact zones. A sliding beam-on-post test structure was also used to measure friction coefficients and wear morphology for different surface coatings and environments. The results show that a predictive model of failure time as a function of drive frequency based on wear fits the functional form of the reliability data quite well and demonstrates the benefits of a fundamental understanding of wear. In [22], it is stated that tribological experimental studies have improved significantly in recent years, leading to a significant number of results and, as a result, an increasing number of papers are appearing. The scatter found in the data is often explained by many variables involved in the experiments, namely: the environment (especially humidity), layers of contaminants, differences in test conditions, uncertainty in the evaluation of the results and rarely – the response of the experimental equipment. This work aims to discuss several sources of inaccuracies that lead to the scatter of experimental tribology results. A reliability

method is proposed to characterize friction and wear data. Experimental results obtained by unidirectional sliding and microabrasion will be used to support the discussion.

In [23], it is stated that system reliability is an extremely important issue, especially in multi-core systems, which tend to have high power density and, consequently, temperature. Existing reliability-based methods are either slow and non-adaptive, or do not use task assignment and scheduling to compensate for the uneven wear state of the core. This paper presents a dynamically activated task assignment and scheduling algorithm based on theoretical results, which clearly optimizes the system lifetime. In the study [24], the effects of the coupling between linear guide wear and vibration of a machine table system are studied based on the infinitesimal method. A nonlinear dynamic model is developed to analyze the wear and vibration failure mechanisms under parameter uncertainty. To assess the dynamic reliability of a machine table system under multiple failure modes, a time-dependent and conditional reliability approach based on the Kriging model with active learning and Monte Carlo simulation is proposed.The approach eliminates the need to recalculate the real values of the limit state function, and the calculation efficiency is significantly increased.

The document [25] describes methods for formulating and assessing the reliability of the system in conditions where failure is the result of wear of system parts reaching a critical threshold. A model is proposed related to the stochastic behavior of wear, in which a continuous, right-hand non-decreasing wear process consists of a “continuous” and a “jump” part. Several properties of the model we have proposed are presented. Also, a number of applied problems on wear and reliability are highlighted in the works [26–29]. At the same time, it should be noted a small proportion of works that analyze numerical dependencies for calculating tribotechnical reliability parameters.

3.3.2. Wear and tear as a random variable

The dependence of wear on the friction path even under constant load is random (Fig. 3.22). At each given friction path, wear at pressureσis a random variable. Like any random variable, wear is characterized by a probability distribution $p(u_w)$ the appearance of this wear: $p(u_w)$ is the density of the wear probability distribution or wear probability uw; $Q(u_w)$ is the probability distribution function of wear

uw, or the probability of wear occurring from zero to the value uw; this function is called the failure function:

$$Q(u_w) = \int_{-\infty}^{\infty} p(u_w)\,du_w, \tag{3.28}$$

$P(u_w)$ is a reliability function or probability of failure-free operation, i.e. the probability that wear u_w will not be achieved:

$$P(u_w) = 1 - Q(u_w). \tag{3.29}$$

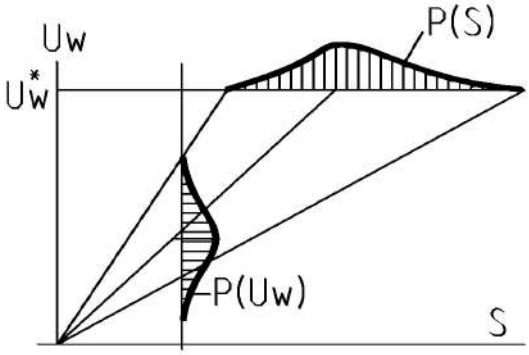

Fig. 3.22. Random distribution of wear and friction path

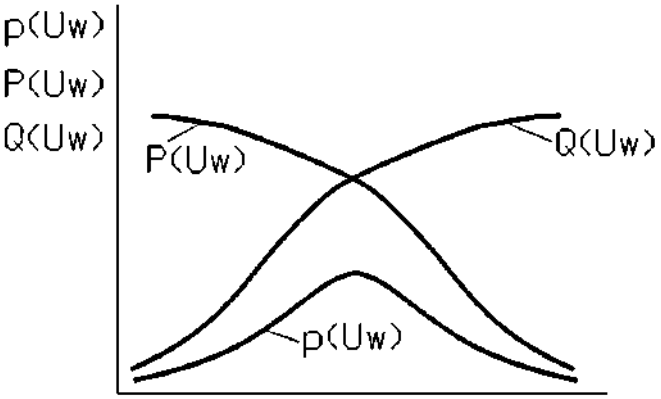

Fig. 3.23. Reliability functions

The probability distribution density is characterized by:
1) the mean or mathematical expectation:

$$\overline{u}_w = m_{u_w} = \frac{1}{N}\sum_{i=1}^{N} u_{wi}; \tag{3.30}$$

2) dispersion

$$D_{u_w} = \frac{1}{N}\sum\left(u_{wi} - u_w\right)^2; \tag{3.31}$$

3) standard deviation

$$S_{u_w} = \sqrt{D_{u_w}}, \tag{3.32}$$

4) coefficient of variation

$$V_{u_w} = \frac{S_{u_w}}{\overline{u}_w}. \tag{3.33}$$

According to the above formulas, the characteristics of the distributions are determined from experimental data u_w and S_i.

Depending on the wear pressure and the friction path, the random nature of the wear is reflected in the value of the wear coefficient k_w:

$$u_w = k_w \sum_{i=1}^{N} \sigma_i^m \Delta s_i$$

Or in integral form:

$$u_w = k_w \sigma^m s. \tag{3.34}$$

In this dependence (3.34), in addition to the random variable k_w, there is, as a rule, the value of the acting pressures σ. Let the system be subjected to a random pressure σ. Random variable σ, as well as k_w, is described by the density distribution $P(\sigma)$ with characteristics: average value $\overline{\sigma}$, pressure dispersion D_σ, the standard deviation S_σ and the coefficient of variation of pressures ν_σ.

It should be emphasized that the random nature of a constantly acting load applies only to the set (set) of friction pairs operating under

all other equal conditions, except for the load, the random nature of which is manifested in the random selection of the load at the beginning of the operation of the unit.

The task of constructing the density of the wear distribution for given wear coefficient distributions k_w and pressure σ in formula (3.34) can practically only be solved approximately. The average wear value $\overline{u}_w$ is calculated by the formula for the average values of the arguments of random $\overline{k}_w$ and $\overline{\sigma}$:

$$\overline{u}_w = \overline{k}_w \overline{\sigma}^m s. \tag{3.35}$$

To calculate the variance D_{uw} we will use the approximate method of linearization of functions, according to which for the independent variables k_w and σ:

$$D_{u_w} = \left(\frac{\partial \overline{u}_w}{\partial \overline{k}_w} \right)^2 D_{k_w} + \left(\frac{\partial \overline{u}_w}{\partial \overline{\sigma}} \right)^2 D_\sigma \tag{3.36}$$

or taking into account (3.34):

$$D_{u_w} = \left(\overline{\sigma}^m s \right)^2 D_{k_w} + \left(\overline{k}_w m \overline{\sigma}^{m-1} s \right)^2 D_\sigma. \tag{3.37}$$

It is obvious that the constant value s can be placed outside the brackets:

$$D_{u_w} = s^2 \left[\left(\overline{\sigma}^m \right)^2 D_{k_w} + \left(\overline{k}_w m \overline{\sigma}^{m-1} \right)^2 D_\sigma \right]. \tag{3.38}$$

3.3.3. Reliability assessment from wear under constant load

The problem is posed as follows: there is a random variable of current wear $u_w(s)$, for example, (3.34) and the random variable of permissible wear u_w^*, it is necessary to find the probability that the current wear does not exceed the permissible one, that is:

$$P = P\left(u_w < u_w^* \right)$$

or

$$P = P\left[\left(u_w - u_w^* \right) > 0 \right]. \tag{3.39}$$

From probability theory it is known that if the density of the distribution of quantities is given $f_1(u_w)$ and $f_2(u^*_w)$, then the distribution density $P(z = u_w - u^*_w)$ is calculated using the integral:

$$P(z) = \int_{-\infty}^{\infty} f_1(u_w) \left[\int_{u_w}^{\infty} f_2(u^*_w) du^*_w \right] du_w . \qquad (3.40)$$

This integral is taken only for certain types of density distributions $f_1(u_w)$ and $f_2(u^*_w)$.

In the case where the distribution of effective and limit stresses obeys the normal law for determining $P(s)$, taking the integral (3.40) is not required in this case.

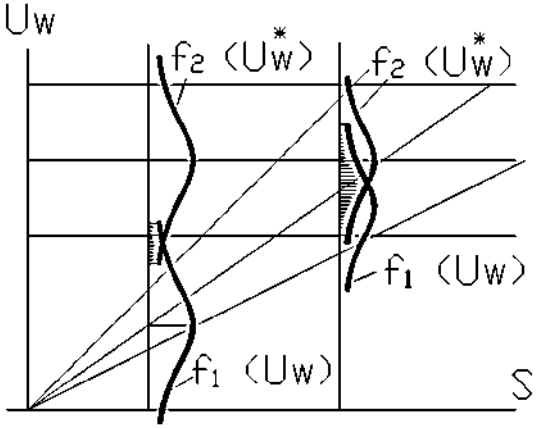

Fig. 3.24. Normal law of wear distribution

The function $P(s)$ also obeys the normal law:

$$P(s) = \frac{1}{s_z \sqrt{2\pi}} e^{-\frac{(z-\bar{z})^2}{2D_z}} , \qquad (3.41)$$

where $z = u_w - u^*_w$, $D_z = D_{u_w} + D_{u^*_w}$, $s_z = \sqrt{D_z}$, $\bar{z} = \bar{u}_w - \bar{u}^*_w$.

The value of the random variable z corresponding to a certain probability $P(s)$ is determined from the expression:

$$z_p = \overline{z} + u_p s_z. \tag{3.42}$$

where u_p is the quantile corresponding to the probability *P*.

Value $z = u_w - u_w^* = 0$ delimits the regions of negative and positive values of z so that the probability of destruction is determined by the condition: $z_p = \overline{z} + u_p s_z = 0$, from which the expression for the desired quantile follows:

$$u_p = -\frac{\overline{z}}{s_z} = \frac{\overline{u}_w - \overline{u}_w^*}{\sqrt{D_{u_w} + D_{u_w^*}}}. \tag{3.43}$$

Entering the depreciation reserve factor:

$$u_p = -\frac{n_w - 1}{\sqrt{n_w^2 v_{u_w^*}^2 + v_{u_w}^2}}; \quad n_w = \frac{u_w^*}{u_w}, \tag{3.44}$$

expression (3.43) is reduced to the form:

$$u_p = -\frac{n_w - 1}{\sqrt{n_w^2 v_{u_w^*}^2 + v_{u_w}^2}}, \tag{3.45}$$

where $v_{u_w^*}$ and v_{u_w} are the coefficients of variation:

$$v_{u_w^*} = s_{u_w^*} / \overline{u}_w^*, \quad v_{u_w} = s_{u_w} / u_w.$$

According to formula (3.45), the probability quantile *P* is determined, and then any of the quantities $p(s)$, $P(s)$ and $Q(s)$.

3.3.4. Calculation of wear reliability under random block loading

Randomness in block loading can manifest itself in:
1) in the random choice of pressure in the stage;
2) in the random choice of interval in the stage;

3) in the random alternation of stages;

4) in the given probability of stages.

Let us consider for example the case where the choice of pressure in a stage is random. Let us assume that in each ith stage:

$$\sigma_i = \overline{\sigma}_i \left(1 + u_p v_\sigma\right) = \overline{\sigma}_i \varepsilon \,. \tag{3.46}$$

The size ε, which reflects the random nature of the load, we will assume the same for all stages.

Substituting expression (3.46) into the equation for wear (3.34), we obtain the statistical expression for wear:

$$u_w = k_w \varepsilon^m \sum \sigma_i^m \Delta s_{i\ddagger} \tag{3.47}$$

Similarly, substituting expression (3.46) for the number of blocks before reaching the limit of wear, we obtain:

$$\lambda = \frac{u_w^*}{k_w \varepsilon^m \sum_1^N \overline{\sigma}_i^m \Delta s_{i\ddagger}} \,. \tag{3.48}$$

Average number of blocks before reaching wear limit:

$$\overline{\lambda} = \frac{\overline{u}_w^*}{\overline{k}_w \sum_1^N \overline{\sigma}_i^m \Delta s_{i\ddagger}} \,. \tag{3.48, a}$$

Average resource of the friction unit:

$$\overline{s} = \lambda \; s_{\ddagger} \,. \tag{3.49}$$

It is necessary to find the probability density function of exceeding the wear limit above the current one. Solving this problem in the case of a normal distribution for u_w^* and u_w, is given by expression (3.45), which can be used to construct the reliability function *P*(*s*). In this case, it is necessary to know the wear dispersion Duw, which we find taking into account (3.47):

$$D_{u_w} = \left(\frac{\partial u_w}{\partial k_w}\right)^2 D_{k_w} + \left(\frac{\partial u_w}{\partial \varepsilon}\right)^2 D_\varepsilon, \qquad (3.50)$$

$$D_{u_w} = \left(\sum \overline{\sigma}_i^m \Delta s_{i\ddagger}\right)^2 D_{k_w} + \left(\overline{k}_w \sum \overline{\sigma}_i^m \Delta s_{i\ddagger}\right)^2 D_\varepsilon. \qquad (3.50, a)$$

Resource distribution taking into account the average value (3.49):

$$s = \overline{s}\left(1 + u_p v_\lambda\right), \qquad (3.51)$$

where $v_\lambda = s_\lambda / \overline{s}$.

Taking into account (3.48):

$$\begin{aligned} s_\lambda^2 &= D_\lambda, \quad D_\lambda = D_{u_w} + D_{u_w^*} \\ v_\lambda &= \sqrt{v_{u_w}^2 + v_{u_w^*}^2}, \quad v_{u_w} = \sqrt{D_{u_w}} / \overline{u}_w. \end{aligned} \qquad (3.52)$$

The most common is the random load, given in the form of the probability P_i of the load action at each stage. In the case of a continuous load application, this is the pressure distribution density problem $P(\sigma)$. With a discrete load assignment, this is $P_i(\sigma_i)$, so $\sum P_i = 1$.

Conclusions

The probabilistic approach allows for more accurate modeling of the behavior of friction units in real-world conditions. The constructed models take into account the variability of loads and wear, which is crucial for predicting reliability. In particular, when applying the models to block loading, significant differences in reliability functions were found compared to constant loading. The proposed methods can be used to design more reliable machines and mechanisms.

References for Chapter 3

1. Bakhor, Z., Yatseiko, A., Ferensovych, R. (2020). Assessment of ferroresonance processes in schemes of 6-35 kV electrical grids on the basis of reliability analysis. Energy Engineering and Control Systems, 6 (2), 137–145. https://doi.org/10.23939/jeecs2020.02.137

2. Akinci, T. C., Akgun, O., Yilmaz, M., Martinez-Morales, A. A. (2023). High Order Spectral Analysis of Ferroresonance Phenomena in Electric Power Systems. IEEE Access, 11, 61289–61297. https://doi.org/10.1109/access.2023.3286817

3. Olguín-Becerril, M. A., Angeles-Camacho, C., Fuerte-Esquivel, C. R. (2014). Ferroresonance in subharmonic 3rd mode in an inductive voltage transformer, a real case analysis. International Journal of Electrical Power & Energy Systems, 61, 318–325. https://doi.org/10.1016/j.ijepes.2014.03.057

4. Sharbain, H. A., Osman, A., El-Hag, A. (2017). Detection and identification of ferroresonance. 2017 7th International Conference on Modeling, Simulation, and Applied Optimization (ICMSAO). https://doi.org/10.1109/icmsao.2017.7934904

5. Martinez, R., Arroyo, A., Pigazo, A., Manana, M., Bayona, E., Azcondo, F. J. et al. (2022). Acoustic Noise-Based Detection of Ferroresonance Events in Isolated Neutral Power Systems with Inductive Voltage Transformers. Sensors, 23(1), 195. https://doi.org/10.3390/s23010195

6. Klimas, M., Majka, Ł. (2019). Enhancing the possibilities in visualisation of the ferroresonance phenomenon. Poznan University of Technology Academic Journals. Electrical Engineering, 98, 115–124. https://doi.org/10.21008/j.1897-0737.2019.98.0010

7. Solak, K., Rebizant, W., Kereit, M. (2020). Detection of Ferroresonance Oscillations in Medium Voltage Networks. Energies, 13 (16), 4129. https://doi.org/10.3390/en13164129

8. Schmool, D. S., Markó, D., Lin, K.-W., Hierro-Rodríguez, A., Quirós, C., Díaz, J. et al. (2021). Ferromagnetic Resonance Studies in Magnetic Nanosystems. Magnetochemistry, 7 (9), 126. https://doi.org/10.3390/magnetochemistry7090126

9. Abdel-hamed, A. M., M. EL-Shafhy, M., A. Badran, E. (2022). Elimination of ferroresonance in the distribution zone by high ohmic reactor-shunt limiter. Indonesian Journal of Electrical Engineering and Computer Science, 28 (3), 1286. https://doi.org/10.11591/ijeecs.v28.i3./ pp1286-1296

10. Zaspa, Y., Dykha, A., Marchenko, D., Matiukh, S., Kukurudzyak, Y. (2020). Exchange interaction and models of contact generation of disturbances in tribosystems. Eastern-European Journal of Enterprise Technologies, 4 (5 (106)), 25–34. https://doi.org/10.15587/1729-4061.2020.209927

11. Dykha, A. V., Zaspa, Yu. P., Slashchuk, V. O. (2018). Triboacoustic Control of Fretting. Journal of Friction and Wear, 39 (2), 169–172. https://doi.org/10.3103/s1068366618020046

12. Dykha, A., Makovkin, O. (2019). Physical basis of contact mechanics of surfaces. Journal of Physics: Conference Series, 1172, 012003. https://doi.org/10.1088/1742-6596/1172/1/012003

13. Blau, PJ (1989). Friction and Wear Transitions of Materials: Break-In, Run-In, Wear-In. Noyes Publications. ISBN: 9780815511960.

14. Stachowiak, GW, & Batchelor, AW (2013). Engineering Tribology (4th ed.). Butterworth-Heinemann. ISBN: 9780123970473.

15. Meng, HC, & Ludema, KC (1995). Wear models and predictive equations: their form and content. Wear, 181–183, 443–457. https://doi.org/10.1016/0043-1648(95)90158-2

16. Bhushan, B. (2013). Introduction to Tribology (2nd ed.). Wiley. ISBN: 9781119943925.

17. Han, D., Han, W., Jureczka, M., & Ochal, A. (2019). Numerical Analysis of a Contact Problem with Wear. arXiv preprint arXiv:1905.05541./ https://arxiv.org/abs/1905.05541arXiv

18. Ravitej, YP, & Kumar, R. (2025). Wear Rate Prediction of Hybrid Composites: A Comparative Study Using Experimental Analysis, Finite Element Simulation, and Machine Learning. SSRN Electronic Journal.https://doi.org/10.2139/ssrn.5177817SSRN

19. Ansys Inc. (2024). Contact Surface Wear Simulation. PyMechanical Examples.https://examples.mechanical.docs.pyansys.com/examples/technology_showcase/example_07_td_043.htmlpymechanical

20. López, S. (2024). Contact Modeling in Ansys Mechanical for Beginners. Ozen Engineering Blog.https://blog.ozeninc.com/resources/understanding-contacts-in-ansys-mechanicalOzen Inc Blog+1LinkedIn+1

21. Tanner, DM, & Dugger, MT (2003). Wear mechanisms in a reliability methodology. Reliability, testing, and characterization of MEMS/MOEMS II, 4980, 22-40.

22. Ramalho, A. (2010). A reliability model for friction and wear experimental data. Wear, 269(3-4), 213–223.

23. Chantem, T., Xiang, Y., Hu, XS, & Dick, RP (2013, March). Enhancing multicore reliability through wear compensation in online assignment and scheduling. In 2013 Design, Automation & Test in Europe Conference & Exhibition (DATE) (pp. 1373-1378). IEEE.

24. Wang, W., Shen, G., Zhang, Y., Zhu, Z., Li, C., & Lu, H. (2021). Dynamic reliability analysis of mechanical systems with wear and vibration failure modes. Mechanism and Machine Theory, 163, 104385.

25. Ebrahimi, N. (2006). System reliability based on system wear. Stochastic models, 22(1), 21-36.

26. Pfeifer, T., & Wiegers, L. (2000). Reliable tool wear monitoring by optimized image and illumination control in machine vision. Measurement, 28(3), 209–218.

27. Yang, MC, Chang, YH, Tsao, CW, & Huang, PC (2013, May). New ERA: New efficient reliability-aware wear leveling for endurance

enhancement of flash storage devices. In Proceedings of the 50th Annual Design Automation Conference (pp. 1–6).

28. Rao, RN, & Das, S. (2010). Wear coefficient and reliability of sliding wear test procedure for high strength aluminum alloy and composite. Materials & Design, 31(7), 3227-3233.

29. Chen, X., He, X., Tang, L., Li, Y., Zhou, M., Jin, W., & Gao, Z. (2020). A heat transfer tube wear reliability analysis method based on the first-order reliability method. Journal of Computational Design and Engineering, 7(6), 803–815.

Диха Олександр Володимирович,
д-р техн. наук, проф., зав. кафедри трибології, автомобілів та матеріалознавства,
Хмельницький національний університет, вул. Інститутська, 11, Україна, 29016
E-mail: tribosenator@gmail.com, тел.: +380975546925
ORCID: http:// orcid.org/ 0000-0003-3020-9625
Oleksandr Dykha
Doctor of Technical Sciences, Professor, Head of Department
of Tribology, Automobiles and Materials Science,
Khmelnitskyi National University, Institutska str., 11, Khmelnitsky, Ukraine, 29016
E-mail: tribosenator@gmail.com, tel.: +380975546925
ORCID: http://orcid.org/0000-0003-3020-9625

Голенко Костянтин Едуардович,
канд. техн. наук, доц. кафедри трибології, автомобілів та матеріалознавства,
Хмельницький національний університет, вул. Інститутська, 11, Україна, 29016
E-mail: holenkoke@khmnu.edu.ua, тел.: +380676709765
ORCID: https://orcid.org/0000-0002-6140-4573
Kostyantyn Holenko
PhD, Associate Professor, Department of Tribology, Automobiles and Materials Science,
Khmelnitskyi National University, Institutska str., 11, Khmelnitsky, Ukraine, 29016
E-mail: holenkoke@khmnu.edu.ua, tel.: +380676709765
ORCID: https://orcid.org/0000-0002-6140-4573

Диха Максим Олександрович,
канд. техн. наук, докторант кафедри трибології, автомобілів та матеріалознавства,
Хмельницький національний університет, вул. Інститутська, 11, Україна, 29016
E-mail: maxdixal@gmail.com, тел.: +380682133057
ORCID: https://orcid.org/0000-0002-6075-1549
Maksym Dykha
PhD, doctoral student, Department of Tribology, Automobiles and Materials Science,
Khmelnitskyi National University, Institutska str., 11, Khmelnitsky, Ukraine, 29016
E-mail: maxdixal@gmail.com, tel.: +380682133057
ORCID: https://orcid.org/0000-0002-6075-1549

Дитинюк Володимир Олександрович,
д-р філософії, ст. викл. кафедри трибології, автомобілів та матеріалознавства,
Хмельницький національний університет, вул. Інститутська, 11, Україна, 29016
E-mail: vdytynyuk28@gmail.com, тел.: +380677570229
ORCID: https://orcid.org/0000-0001-6377-524X
Volodymyr Dytyniuk
PhD, Senior Lecturer, Department of Tribology, Automobiles and Materials Science,
Khmelnitskyi National University, Institutska str., 11, Khmelnitsky, Ukraine, 29016
E-mail: vdytynyuk28@gmail.com, tel.: +380677570229
ORCID: https://orcid.org/0000-0001-6377-524X

Наукове видання

Диха Олександр Володимирович,
Голенко Костянтин Едуардович,
Диха Максим Олександрович,
Дитинюк Володимир Олександрович

Simulation of stress state and tribological behavior in structural elements of transport systems

Моделювання напруженого стану та трибологічної поведінки у конструкційних елементах транспортних систем

Відповідальний за випуск: ***В. С. Яремчук***

Художнє оформлення обкладинки: ***А. М. Басалюк***

Технічне редагування, коректування і верстка: ***О. В. Чопенко***

Підписано до друку 31.07.2025.
Формат 30×42/2. Папір офс. Гарн. Times New Roman.
Друк різографією. Ум. друк. арк. – 11,20. Обл.-вид. арк. – 10,51.
Тираж 50. Зам. № 82/25

Редакційно-видавничий відділ ХНУ.
29016, м. Хмельницький, вул. Інститутська, 7/1.
Свідоцтво про внесення в Державний реєстр, серія ДК № 4489 від 18.02.2013 р.

S614 **Диха О. В., Голенко К. Е., Диха М. О., Дитинюк В. О.**
Simulation of stress state and tribological behavior in structural elements of transport systems = Моделювання напруженого стану та трибологічної поведінки у конструкційних елементах транспортних систем : монографія / О. В. Диха, К. Е. Голенко, М. О. Диха, В. О. Дитинюк. Хмельницький : ХНУ, 2025. 187 с.
ISBN 978-966-330-450-2

Виконано чисельне моделювання напруженого стану та трибологічної поведінки конструкційних елементів транспортних систем. Розглянуто механічні, теплові та контактні процеси за реальних умов їх експлуатації. Наведено приклади застосування методу скінченних елементів для аналізу напружено-деформованого стану, оцінки міцності та зносу. Описано підходи до побудови розрахункових моделей і обробки результатів моделювання.

Для здобувачів бакалаврського та магістерського рівнів автомобільного спрямування, викладачів та аспірантів.

The monograph addresses the numerical modeling of stress state and tribological behavior in structural elements of transport systems. It considers mechanical, thermal, and contact processes occurring under real operating conditions of vehicles. Examples of finite element method applications are provided for analyzing stress–strain states, strength assessment, and wear prediction. The approaches to constructing computational models and processing simulation results are described.

The publication is intended for bachelor's and master's degree students in the field of automotive engineering, as well as for lecturers and postgraduate students.

УДК 621.89:629